University of California
Santa Barbara

Structure and Dispersion of Active Matter in Confinement

A dissertation submitted in partial satisfaction
of the requirements for the degree

Doctor of Philosophy
in
Chemical Engineering

by

Kevin Joseph Modica

Committee in charge:

Professor Sho C. Takatori, Chair
Professor Todd Squires
Professor M. Scott Shell
Professor Zvonimir Dogic

June 2024

The Dissertation of Kevin Joseph Modica is approved.

Professor Todd Squires

Professor M. Scott Shell

Professor Zvonimir Dogic

Professor Sho C. Takatori, Committee Chair

June 2024

Structure and Dispersion of Active Matter in Confinement

Kevin Joseph Modica

Dedicated to all of my mentors. You taught me that a scientist needs to dream, not just measure.

Acknowledgements

A person's graduate school experience is shaped by the people they spend it with. I am extraordinarily fortunate to be surrounded by such wonderful people.

First, I would like to thank my advisor, Professor Sho Takatori. I came to UCSB in large part because of him; his enthusiasm for science is infectious. In addition to his ability to seamlessly blend expertise in rigorous theory *and* challenging experiments, what I admire most about Sho is his commitment to ensuring each of his students become the best and happiest version of themselves. None of this thesis would be possible without his constant guidance and patient mentorship. Sho, thank you for believing in me even when I began to doubt myself, your support means more than I can express.

I have had several excellent mentors during my scientific career. My thesis committee, Professors Todd Squires, Scott Shell, and Zvonimir Dogic has been a valuable resource throughout grad school. They each encouraged me to think about my project from a different perspective. I thank them for all of the time and effort they spent helping my growth as a scientist. Professor Ahmad Omar met with me many times over Zoom as I was beginning my research. It was through our discussions that the original kernel of this dissertation was formed. Dr. Joseph Barakat taught me how to formulate a problem in a rigorous way that was amenable to computation (your patience is formidable). My undergrad mentors, Professor Arthi Jayaraman and Dr. Tyler Martin, took a wide-eyed freshman under their wings and are role models that I still treasure to this day.

My first labmates, Starry Xu and Daniel Arnold, made going to grad school more than just *going* to grad school. Thank you for all of the laughs, debates, games, and discussions we have had over the years. You are both exceptional scientists, phenomenal communicators, and deep thinkers. It was a real pleasure to work by your side. We took a risk joining a brand new lab. I'm happy to say I wouldn't trade a second of it away.

The rest of the lab, Sachit Nagella, Kyu Hwan Choi, Titus Quah, and Aakanksha Gubbala, have been extraordinary colleagues and good friends to work alongside. I know I'm leaving the Takatori group in good hands. Thank you Sachit for teaching me hydrodynamics and, more importantly, thank you for putting up with me when I took us an hour out of our way to see a movie in a larger screen.

I have made so many friends over my time at Santa Barbara, but only have space to acknowledge a few in particular. Zach, Justin, and Emily, thank you for being my housemates. I'm glad our friendship has grown stronger even though I kept hogging the laundry machine. Isabel, Ryan, Olivia, Greg, Taylor, Kelsey, Jon, and more, thank you for teaching me the value of trashy reality TV. A sincere thank you to my friends at home and abroad: Shuler, Vikki, Caitlin, Shapiro, Owen, Mara, Tyler, Abby, and all the rest, for keeping me sane when I was juggling a thousand things. I am especially grateful to my partner Andrea for her love and support. You remind me to enjoy the journey, not just the destination. That is the greatest wisdom I know.

Being so far from home in New Jersey, the precious love and support from my family is invaluable. I am fortunate to have such a large and loving family rooting for me. To my grandparents Daniel, Mary, Pat, and Joe, thank you for your love and patience, even when my trips home grew less frequent. I'd like to thank my aunt Jean and my uncle Ralf for encouraging my love of science. I still remember all of those books and magazines you gave me. To my parents, Danette and Joe, and our wonderful dog, the late Lucky Modica, I love you all "L.T.B.". I would not be here without your love and encouragement. I could not imagine a better support system. Thank you.

I am also grateful to the National Science Foundation Graduate Research Fellowship (Grant No. 1650114), the U.S. Army Research Office (Cooperative Agreement No. W911NF-19-2-0026) and the Air Force Office of Scientific Research (Award No. FA9550-21-1-0287) who supported and funded parts of this thesis.

Curriculum Vitæ

Kevin Joseph Modica

Education

2024	Doctor of Philosophy in Chemical Engineering (expected), University of California, Santa Barbara *Advisor*: Professor Sho C. Takatori
2019	Honors B.ChE. with Distinction in Chemical Engineering, University of Delaware

Professional Experience

2019-2024	Graduate Research Fellow, University of California, Santa Barbara
Summer 2023	Reaction Engineering Intern, Dow Chemical, Lake Jackson, TX
2016-2019	Undergraduate Researcher, University of Delaware

Publications (* Equal Contribution)

1. J Cheon*, KH Choi*, **KJ Modica**, RJ Mitchell, SC Takatori, J Jeong. "Motility Modulates the Partitioning of Bacteria in Aqueous Two-Phase Systems". (*submitted*).
2. JM Barakat*, **KJ Modica***, L Lu, S Anujarerat, KH Choi, SC Takatori. "Surface Topography Induces and Orients Nematic Swarms of Active Filaments: Considerations for Lab-On-A-Chip Devices". *ACS Applied Nano Materials* 7 (10) 12142-12152 (2024).
3. **KJ Modica**, SC Takatori. "Soft Confinement of Self-Propelled Rods: Simulation and Theory". *Soft Matter* 20 (10), 2331-2337 (2024).
4. **KJ Modica**, AK Omar, SC Takatori. "Boundary Design Regulates the Diffusion of Active Matter in Heterogeneous Environments". *Soft Matter* 19 (10), 1890-1899 (2023).
5. **KJ Modica**, Y Xi, SC Takatori. "Porous Media Microstructure Determines the Diffusion of Active Matter: Experiments and Simulations". *Frontiers in Physics* 10, 869175 (2022).
6. A Kulshreshtha, **KJ Modica**, A Jayaraman. "Impact of Hydrogen Bonding Interactions on Graft–Matrix Wetting and Structure in Polymer Nanocomposites" *Macromolecules* 52 (7), 2725-2735 (2019).
7. **KJ Modica***, TB Martin*, A Jayaraman. "Effect of Polymer Architecture on the Structure and Interactions of Polymer Grafted Particles: Theory and Simulations". *Macromolecules* 50 (12), 4854-4866 (2017).

Selected Presentations

1. **KJ Modica**, SC Takatori. "Active Rods in "Soft" Confinement: Increasing Dispersion via Nematic Alignment". Oral Presentation at APS March Meeting 2024; Minneapolis, MN.
2. **KJ Modica**, SC Takatori. "Active Rods in "Soft" Confinement: Increasing Dispersion via Nematic Alignment". Oral Presentation at Amgen-Clorox Graduate Student Symposium 2023; UC Santa Barbara, CA.
3. **KJ Modica**, JM Barakat, SC Takatori. "Surface Topography Influences Driven Filament Alignment and Controls Swarm Formation". Oral Presentation at AIChE Annual Meeting 2022; Phoenix, AZ.
4. **KJ Modica**, JM Barakat, SC Takatori. "Surface Topography Influences Driven Filament Alignment and Controls Swarm Formation". Poster Presentation at Colloidal, Macromolecular and Polyelectrolyte Solution Gordon Research Conference and Seminar 2022; Ventura CA.

Awards & Fellowships

January 2024	Doctoral Student Travel Grant.
March 2021	NSF Graduate Research Fellowship.
May 2019	Dave GR Short Senior Design Award.
April 2019	Charles B Evans Prize for Outstanding Original Research.
March 2019	AIChE DVS Design Report Award Nominee.
August 2018	Charles S and Silvia Joanedis Scholarship.

Abstract

Structure and Dispersion of Active Matter in Confinement

by

Kevin Joseph Modica

Many living systems, such as bacteria or eukaryotic cells, utilize self-propulsion to enhance transport, find nutrients, or avoid threats. However, cells often inhabit complex and heterogeneous spaces—e.g. gels and tissues in the body, or soil sediments in the environment—that impede rapid transport. Additionally, many biologically and industrially relevant complex materials are opaque and difficult to characterize, indicating the need for adequate computational and analytical models to guide experimental efforts.

In this dissertation, I utilize theory and simulation to study the structure and motion of microscopic self-propelled (or active) species in confinement, including bacteria, synthetic swimmers, and cytoskeletal filaments. Active matter systems are inherently nonequilibrium and traditional theories of Brownian motion in porous media fail to accurately describe the swimmers' dispersion. Active particles accumulate along boundaries due to their self-propulsion, even in the absence of attractive interactions. This mechanism traps the active particles at regions of high concavity, coupling the diffusivity of the swimmer to the microstructure of the confining walls.

I then extend these theories to study the motion of anisotropic active particles (like cytoskeletal filaments or rod-shaped bacteria) in the presence of soft confinement. I develop a Smoluchowski model that demonstrates the connection between the long-time self-diffusivity and active rod nematic order. Finally, I use these results to examine the partitioning of bacteria in an aqueous two-phase system, and the nematic ordering of F-actin filaments on topographically patterned channels.

Contents

Chapter 1

Introduction

1.1 The Role of Active Transport in Human Health and Industry

Anyone who has driven through Los Angeles traffic can tell you the world is crowded. A significant portion of our lives, and indeed that of most living creatures, is spent finding efficient mechanisms to navigate cramped environments. At the macroscale, we contend with streets, crowds, and forests. Navigating around these obstacles can be both tortuous and torturous. Yet these challenges magnify at the microscale. Soil sediments, clays, and mucus can trap microscopic organisms like bacteria and inhibit cell proliferation. To overcome these obstacles, living creatures have evolved various methods of self-propulsion: humans walk, birds fly, and motile bacteria swim. Understanding how bacteria navigate crowded spaces is crucial in fields like agriculture, industry, and human health. After all, a bacterium's ability to move freely can determine if it benefits us, harms us, or simply gets stuck. Whether a microbe gets trapped or transmitted depends as much on the medium as it does on the creature.

Self-locomotion enables living creatures to avoid threats, find nutrients, and explore their environments. Cells often inhabit complex and heterogeneous media bounded by walls, pores, or other microbes, all of which inhibit navigation through the space. Pathogenic bacteria squeeze through pores in tissues and mucus to spread through the body [1–6] —leading to potentially life-threatening infections. After spreading, planktonic bacteria may adhere to a nearby surface and initialize the formation of a biofilm. These densely packed colonies of bacteria resist treatment and subvert innate immune defenses. On the other hand, the transport of bacteria through soil plays an important role in bioremediation [7, 8] and rhizosphere bacteria protect plant roots to promote growth [9].

In Fig. 1.1, we show a schematic of a bacterium as well as two example crowded

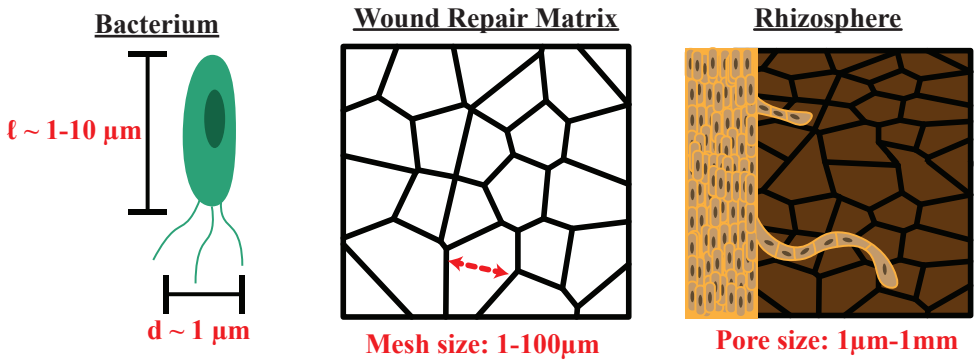

Figure 1.1: Schematic demonstrating the relevant length scales in bacteria penetration of wound repair material (like collagen or fibrin) and the rhizosphere near plant roots. Microbes exist in dense, crowded environments.

environments: a polymer matrix designed to promote wound healing or tissue engineering, and the rhizosphere soil surrounding a plant root. These materials may have pore sizes of a similar magnitude to the length or diameter of the swimmer, inhibiting transport through the material. In a wound site, fibrin and collagen form a matrix to restore hemostasis and protect the body from invading bacteria [10, 11]. The outermost layer has small pores to prevent microbial penetration (1-10µm), but the inner layers need to be large enough for fibroblast proliferation and to encourage vascularization [12]. Similarly, bacteria can impact root nutrient uptake and promote plant growth [13]. In one gram of ectorhizosphere soil (within ∼2mm of the root) there are about 10^{10}-10^{12} other cells competing with each other in the sediment network [14, 15].

Recent advancements in micro/nanoscale synthesis have also led to the creation of artificial swimmers that are excellent tools in the study of autonomous self-propulsion [16–23]. Understanding the motion of these living and synthetic active matter constituents embedded within heterogeneous materials is a challenging problem because of the complex interactions between the swimmer and the material boundaries. Unfortunately, many biologically or industrially relevant porous materials are opaque and the details of the microstructure are challenging to resolve. Only recently have experiments been able

to directly observe and track individual cell motion through a 3D porous domain [24]. Therefore, the development of theoretical models to predict boundary effects on self-propelled constituents is critical to our understanding of active transport in complex physical environments.

Cytoskeletal filaments like F-actin and microtubules can also be studied using the mechanics of active matter. Inside single cells, these biopolymers are often self-propelled by molecular motors such as myosin, kinesin, or dynein. In vitro gliding assays bind motor proteins to a substrate and propel attached filaments using ATP [25]. These motility assays are commonly used to study the physics of cytoskeletal rearrangement and cargo transport in the cell. In addition to acting as a surrogate model for studying cells, gliding assays are a promising candidate in the creation of lab on-a-chip devices. By specifically patterning the topography of the substrate, researchers are able to create microfluidic computers or sensitive analyte detectors [26, 27].

The models developed in this dissertation are general, and may be applicable to a variety of self-propelled agents. In collaboration with experimentalists, we test these models against synthetic, microbial, and cytoskeletal active matter.

1.2 Diffusion in Porous Media

This thesis is focused on the diffusion of motile particles in confinement, so we will begin with a brief review of of non-motile (thermal) diffusion in porous materials. The diffusion of a colloidal species is generally described by its diffusivity tensor $\boldsymbol{D}$, which in principle can be a function of the temperature, concentration, and other experimental conditions. Generally it is assumed that motion is isotropic and a scalar-valued diffusivity is used instead $\boldsymbol{D} = D\boldsymbol{I}$.

Adding to the complexity is the presence of multiple—potentially overlapping—

definitions of diffusivity, all of which may be relevant when describing particle transport [28]. In a colloidal system, these are the *short-time* self-diffusivity, D_0^s, the *long-time* self-diffusivity, D_∞^s, and the *collective* diffusivity D^c. These are all equivalent in the simplest case of infinite dilution in a unbounded system, but each corresponds to a distinct physical process as shown in Fig. 1.2. The short-time self-diffusivity measures the local mobility at timescales long compared to the momentum relaxation of a particle $\tau_I = m/\zeta$ (where ζ is the relevant drag coefficient), but small compared to the time it takes the particle to move a fraction of its size (also called the Smoluchowski time) $\tau_S = \sigma^2\zeta/k_\mathrm{B}T$. Where k_B is the Boltzmann constant, T is the temperature, and σ is the particle size. The aptly named long-time self-diffusivity measures the dispersion of a particle at times much greater than τ_S and any other timescale in the system, when the particle has been able to fully explore its environment. Finally, the collective diffusivity corresponds to the diffusivity one would measure from Fick's first law. It describes the relationship between the net flux of collections of particles in the presence of a macroscopic concentration gradient.

In this dissertation, we will focus on determining the long-time self-diffusivity (also called the effective diffusivity $\boldsymbol{D}_E$). This quantity describes the relevant mobility of a single particle moving through a porous medium. The effective diffusivity is equivalent to the slope of the mean-squared displacement at long time,

$$\boldsymbol{D}_E = \frac{1}{2}\lim_{t\to\infty}\frac{d}{dt}\langle\Delta\boldsymbol{x}(t)\Delta\boldsymbol{x}(t)\rangle. \tag{1.1}$$

where $\langle\cdot\rangle$ is the ensemble average and $\Delta\boldsymbol{x}(t) = \boldsymbol{x}(t) - \boldsymbol{x}(0)$.

The long-time self-diffusivity captures all the effects (if any) from the surrounding hydrodynamics, finite concentration, and geometric confinement to provide an powerful descriptor of the spread of a particle at long time. For a vapor, the diffusion of molecules is determined by the molecular speed and the mean free path. Gas phase particles

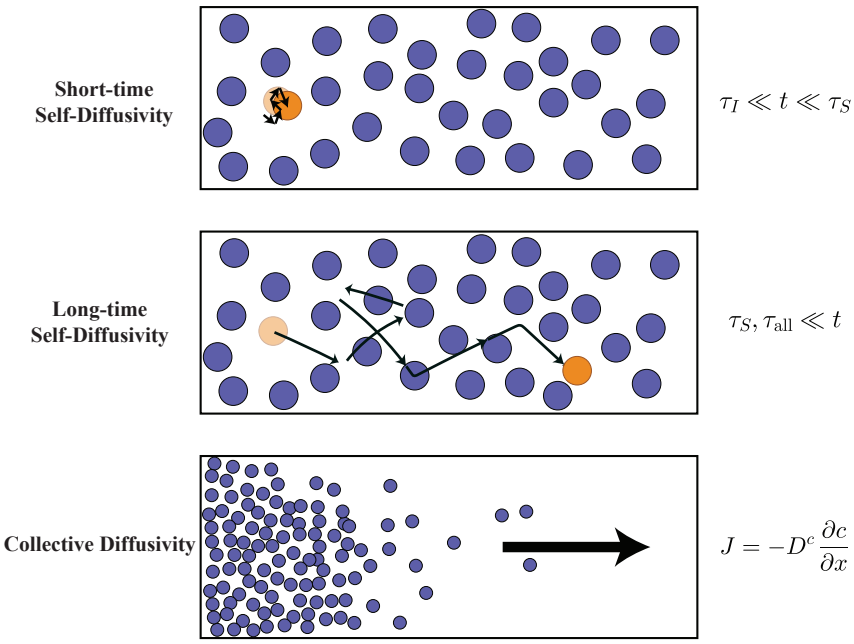

Figure 1.2: Schematic describing three relevant diffusivities of colloidal particles. The short-time self-diffusivity describes the mobility of a particle at times large compared to the inertial time, but small compared to the Smoluchowski time. The long-time self-diffusivity describes mobility at times large compared to all other time-scales of the system. The collective diffusivity relates the flux to macroscopic concentration gradients.

move at a high speed due to their kinetic energy, and rarely collide with each other, resulting in gaseous self-diffusion coefficients easily reaching several square-centimeters per second. Colloidal particle diffusion occurs due to collisions with the solvent and decreases rapidly with particle size. For a dilute suspension, the impact of other colloids is minimal and the short-time self-diffusivity converges to the traditional Stokes-Einstein-Sutherland diffusivity $D_T = k_{\text{B}}T/\zeta$, which is ~ 0.5 μm^2/s for a 1 μm diameter sphere in water at room temperature.

In a confined environment, colloidal transport is hindered by the boundaries. For a freely draining system, the short-time self-diffusivity of a colloid remains as D_T; however, the long-time particle mobility can be drastically reduced by the pore geometry. Strategies for estimating the effective diffusivity of Brownian particles are discussed in

Chapter 2 and compared against simulation and exact calculation for active particles.

1.3 Motion of Colloidal Swimmers

One example mechanism by which bacteria self-propel is using flagella—slender, helical appendages that rotate to induce motion [29]. The canonical examples of *Escherichia coli* and *Bacillus subtilis* have bundles of flagella that cooperatively rotate to push the surrounding fluid and generate a ballistic "run" followed by rapid reorientation in a "tumble".

In general, the dynamics of a particle suspended in a fluid are governed by the Langevin equation.

$$m\frac{d\boldsymbol{U}}{dt} = \boldsymbol{F}^B + \boldsymbol{F}^H + \boldsymbol{F}^P \tag{1.2a}$$

$$\boldsymbol{\mathcal{I}}\frac{d\boldsymbol{\Omega}}{\mathrm{d}t} = \boldsymbol{L}^B + \boldsymbol{L}^H + \boldsymbol{L}^P \tag{1.2b}$$

where m is the particle mass, $\boldsymbol{\mathcal{I}}$ is the moment of inertia tensor, $\boldsymbol{U}$ and $\boldsymbol{\Omega}$ are the translational and angular velocities. $\boldsymbol{F}$ and $\boldsymbol{L}$ are the forces and torques acting on the particle, with the superscript B representing Brownian motion from solvent fluctuations, H representing the remaining hydrodynamic components, and P representing the remaining interparticle and external forces and torques acting on the particle. Generally, defining the rotational and translational velocities of a body requires six degrees-of-freedom, three angular and three spatial, but for the purposes of this discussion we will ignore the roll rotation and assume the particle is axisymmetric.

The Reynolds number (Re) is a dimensionless number that describes flow conditions and indicates the ratio of inertial forces to viscous forces in the fluid. Near a swimmer, it is defined as $\mathrm{Re} = \rho LU/\mu$, where ρ is the fluid density, U is the swimming velocity, L is half the body length, and μ is the fluid viscosity. For most microscopic swimmers in water,

the Reynolds number is between $10^{-6} - 10^{-2}$ [30], indicating that inertia is negligible and particles move in the Stokes regime. For the purposes of this thesis, we will be considering motion in the Re = 0 regime and their motion is considered "force-free". Therefore, particle inertia can be safely ignored. Active particles swim in a so-called "force-free" manner by generating their own motion internally, such that there are no *external* forces acting on the particle to induce a velocity. Instead, the particle generates its own fluid flow via cilia or flagella (for microorganisms) or, say, self-diffusiophoresis / self-electrophoresis (for inanimate colloidal particles) [31, 32].

The velocity of the surrounding fluid at any point $\boldsymbol{r}$ along the swimmer surface is $\boldsymbol{u}(\boldsymbol{r}) = \boldsymbol{U} + \boldsymbol{\Omega} \times (\boldsymbol{r} - \boldsymbol{x}) + \boldsymbol{u}^{\text{slip}}(\boldsymbol{r})$. Where $\boldsymbol{x}$ is the body center and $\boldsymbol{u}^{\text{slip}}$ is the slip velocity. Following the convention of Takatori and Brady [33], the slip velocity can be expressed in terms of surface moments $\boldsymbol{u}^{\text{slip}} = \boldsymbol{E}^s \cdot \boldsymbol{x}' + \boldsymbol{B}^s : (\boldsymbol{x}'\boldsymbol{x}' - \boldsymbol{I}(x')^2) + \cdots$, where $\boldsymbol{x}' = \boldsymbol{r} - \boldsymbol{x}$, and the surface moment tensors are in general a function of time.

This method allows us to group the hydrodynamic forces (and torques) into a drag component and a swim component,

$$\boldsymbol{F}^H = [-\boldsymbol{R}_{FU} \cdot \boldsymbol{U} - \boldsymbol{R}_{F\Omega} \cdot \boldsymbol{\Omega}] + \left[-\boldsymbol{R}_{FE} : \boldsymbol{E}^s - \boldsymbol{R}_{FB} \vdots \boldsymbol{B}^s - \cdots\right] \tag{1.3a}$$

$$\boldsymbol{L}^H = [-\boldsymbol{R}_{L\Omega} \cdot \boldsymbol{\Omega} - \boldsymbol{R}_{LU} \cdot \boldsymbol{U}] + \left[-\boldsymbol{R}_{LE} : \boldsymbol{E}^s - \boldsymbol{R}_{LB} \vdots \boldsymbol{B}^s - \cdots\right], \tag{1.3b}$$

where the first grouping in each equation represents the drag, and the second grouping is the (internally generated) swim force / torque $\boldsymbol{F}^S$ and $\boldsymbol{L}^S$. In these equations $\boldsymbol{R}_{AB}$ is the resistance tensor coupling the motion B to the resulting force A (or torque, stress, etc.).

For now, we will ignore coupling between the translation and rotation in the drag ($\boldsymbol{R}_{LU} = \boldsymbol{R}_{F\Omega} = \boldsymbol{0}$), and assume that the self-propulsion mechanism imposes no net torque on the particles, allowing us to write the overdamped Langevin equations of

motion as

$$\frac{d\boldsymbol{x}}{dt} = \boldsymbol{R}_{FU}^{-1} \cdot \left[\boldsymbol{F}^B + \boldsymbol{F}^S + \boldsymbol{F}^P\right] \tag{1.4a}$$

$$\frac{d\boldsymbol{q}}{dt} = \boldsymbol{R}_{L\Omega}^{-1} \cdot \left[\boldsymbol{L}^B + \boldsymbol{L}^P\right] \tag{1.4b}$$

where $\boldsymbol{x}$ is the position vector and $\boldsymbol{q}$ is the orientation unit vector. The Brownian forces and torques $\boldsymbol{F}^B$ and $\boldsymbol{L}^B$ are subject to the fluctuation dissipation theorem,

$$\langle \boldsymbol{F}^B(t) \rangle = \boldsymbol{0} \tag{1.5a}$$

$$\langle \boldsymbol{F}^B(t)\boldsymbol{F}^B(0) \rangle = 2k_{\mathrm{B}}T\boldsymbol{R}_{FU}\delta(t) \tag{1.5b}$$

$$\langle \boldsymbol{L}^B(t) \rangle = \boldsymbol{0} \tag{1.5c}$$

$$\langle \boldsymbol{L}^B(t)\boldsymbol{L}^B(0) \rangle = 2k_{\mathrm{B}}T\boldsymbol{R}_{L\Omega}\delta(t) \tag{1.5d}$$

where k_{B} is the Boltzmann constant, T is the temperature, and δ is the Dirac delta function.

The active Brownian particle (ABP) model is a powerful tool to study the motion of an active swimmer. To a first approximation, the hydrodynamic resistance tensor is the Stokes drag factor $\boldsymbol{R}_{FU} = \zeta\boldsymbol{I}$, where $\zeta = 3\pi\mu\sigma$ in a Newtonian fluid of viscosity μ and particle diameter σ. Similarly, the resistance tensor for the rotation is $\boldsymbol{R}_{L\Omega} = \zeta_R\boldsymbol{I}$, with $\zeta_R = \pi\mu\sigma^3$. This model represents the self-propulsion as an internal body force $\boldsymbol{F}^S = \zeta u_0 \boldsymbol{q}$, in which the direction unit vector $\boldsymbol{q} = \cos(\theta)\hat{\boldsymbol{e}}_x + \sin(\theta)\hat{\boldsymbol{e}}_y$ migrates via Brownian motion. For a spherical active Brownian particle in two-dimensions, the ABP equation can be written as

$$\frac{d\boldsymbol{x}}{dt} = \sqrt{2D_T}\boldsymbol{\eta}(t) + \frac{1}{\zeta}\left(\zeta u_0 \boldsymbol{q} + \boldsymbol{F}^P\right) \tag{1.6a}$$

$$\frac{d\theta}{dt} = \sqrt{2D_R}\xi(t). \tag{1.6b}$$

The thermal and rotational diffusion coefficients are $D_T = k_{\mathrm{B}}T/\zeta$ and $D_R = k_{\mathrm{B}}T/\zeta_R$, the swim speed is u_0, and $(\boldsymbol{\eta},\ \xi)$ are random variables obeying the zero mean and variance consistent with the fluctuation-dissipation theorem.

While the trajectory of a single ABP can be found by solving the overdamped Langevin equation (Eq. 1.6), it requires precise knowledge and integration of the stochastic Brownian forces and torques acting on the particle for the period of interest. Instead, the dynamics of an active particle can be described by the conditional probability, $P(\boldsymbol{x}, \boldsymbol{q}, t|\boldsymbol{x}_0, \boldsymbol{q_0}, t_0)$, of finding the particle at position $\boldsymbol{x}$ and orientation $\boldsymbol{q}$ at time t, given that it was located at position $\boldsymbol{x}_0$ and orientation $\boldsymbol{q}_0$ at time t_0. This probability density obeys the Smoluchowski equation

$$\frac{\partial P(\boldsymbol{x}, \boldsymbol{q}, t)}{\partial t} + \nabla_T \cdot \boldsymbol{j}_T + \nabla_R \cdot \boldsymbol{j}_R \tag{1.7a}$$

$$\boldsymbol{j}_T = P\left[u_0\boldsymbol{q} - D_T\nabla_T \ln P + \frac{1}{\zeta}\boldsymbol{F}^P\right] \tag{1.7b}$$

$$\boldsymbol{j}_R = P\left[-D_R\nabla_R \ln P + \frac{1}{\zeta_R}\boldsymbol{L}^P\right]. \tag{1.7c}$$

with translational and rotational fluxes $\boldsymbol{j}_T$ and $\boldsymbol{j}_R$. The translational gradient is $\nabla_T = \frac{\partial}{\partial \boldsymbol{x}}$, and the rotational gradient is $\nabla_R = \boldsymbol{q} \times \frac{\partial}{\partial \boldsymbol{q}}$.

1.4 Structure of this Dissertation

This thesis consists of independent chapters presented as a form suitable for publication, with Chapters 2, 3, 4, and 6 already published. In Chapter 2, I present several case studies of example porous materials and discuss existing techniques for predicting passive (not self-propelled) diffusion. I then assess their validity in a nonequilibrium active system by comparing predictions to exact results calculated by simulation and direct numerical calculation. In Chapter 3, I isolate the unique coupling of surface cur-

vature and activity to the diffusivity, as well as validate our approach with experimental measurements of ABPs in randomly placed obstacles.

In Chapter 4, I consider the impact of soft confinement, where the motion along one axis is inhibited but not prohibited. When the swimmer is anisotropically shaped, the dispersion can be *increased* by confinement along one axis due to the nematic alignment for rod-shaped colloids in a confined medium. Chapter 5 uses the theory developed in previous chapters to describe the partitioning of bacteria in an aqueous two-phase system of dextran and polyethylene glycol.

In Chapter 6, I apply our methodology onto a system of practical interest, gliding assays of cytoskeletal filaments. Careful analysis and simulation demonstrates that local surface curvatures can create a form of soft-confinement that creates nematic swarms. The bending energy of F-actin competes with the self-propulsive force to determine whether the actin will align or bend out-of-plane and escape from a channel. This effect is subtle, it occurs only at intermediate channel spacing when the filament nematic order is coherent across the entire channel width. In Chapter 7, I summarize our findings as well as present areas for future work.

Bibliography

[1] D. Ribet and P. Cossart, *How bacterial pathogens colonize their hosts and invade deeper tissues*, *Microbes and Infection* **17** (2015), no. 3 173–183.

[2] S. X. Gu and S. R. Lentz, *Fibrin films: overlooked hemostatic barriers against microbial infiltration*, *Journal of Clinical Investigation* **128** (8, 2018) 3243–3245.

[3] C. Y. Kao, W. H. Lin, C. C. Tseng, A. B. Wu, M. C. Wang, and J. J. Wu, *The complex interplay among bacterial motility and virulence factors in different*

Escherichia coli infections, *European Journal of Clinical Microbiology & Infectious Diseases* **33** (12, 2014) 2157–2162.

[4] R. Lux, J. N. Miller, N.-H. Park, and W. Shi, *Motility and chemotaxis in tissue penetration of oral epithelial cell layers bytreponema denticola*, *Infection and Immunity* **69** (10, 2001) 6276–6283.

[5] S. S. Datta, A. Preska Steinberg, and R. F. Ismagilov, *Polymers in the gut compress the colonic mucus hydrogel*, *Proceedings of the National Academy of Sciences* **113** (6, 2016) 7041–7046.

[6] S. Balzan, C. De Almeida Quadros, R. De Cleva, B. Zilberstein, and I. Cecconello, *Bacterial translocation: Overview of mechanisms and clinical impact*, *Journal of Gastroenterology and Hepatology* **22** (3, 2007) 464–471.

[7] J. Gannon, U. Mingelgrin, M. Alexander, and R. Wagenet, *Bacterial transport through homogeneous soil*, *Soil Biology and Biochemistry* **23** (1, 1991) 1155–1160.

[8] J. S. T. Adadevoh, S. Triolo, C. A. Ramsburg, and R. M. Ford, *Chemotaxis Increases the Residence Time of Bacteria in Granular Media Containing Distributed Contaminant Sources*, *Environmental Science & Technology* **50** (1, 2016) 181–187.

[9] O. O. Babalola, *Beneficial bacteria of agricultural importance*, *Biotechnology Letters* **32** (7, 2010) 1559–1570.

[10] O. Moreno-Arotzena, J. Meier, C. del Amo, and J. García-Aznar, *Characterization of fibrin and collagen gels for engineering wound healing models*, *Materials* **8** (4, 2015) 1636–1651.

[11] I. K. Piechocka, R. G. Bacabac, M. Potters, F. C. MacKintosh, and G. H. Koenderink, *Structural hierarchy governs fibrin gel mechanics*, *Biophysical Journal* **98** (5, 2010) 2281–2289.

[12] M. R. MacEwan, S. MacEwan, T. R. Kovacs, and J. Batts, *What makes the optimal wound healing material? a review of current science and introduction of a synthetic nanofabricated wound care scaffold*, *Cureus* (10, 2017).

[13] Q. Saeed, W. Xiukang, F. U. Haider, J. Kučerik, M. Z. Mumtaz, J. Holatko, M. Naseem, A. Kintl, M. Ejaz, M. Naveed, M. Brtnicky, and A. Mustafa, *Rhizosphere bacteria in plant growth promotion, biocontrol, and bioremediation of contaminated sites: A comprehensive review of effects and mechanisms*, *International Journal of Molecular Sciences* **22** (9, 2021) 10529.

[14] J. R. Helliwell, C. J. Sturrock, S. Mairhofer, J. Craigon, R. W. Ashton, A. J. Miller, W. R. Whalley, and S. J. Mooney, *The emergent rhizosphere: imaging the development of the porous architecture at the root-soil interface*, *Scientific Reports* **7** (11, 2017) 14875.

[15] D. McNear Jr, *The rhizosphere-roots soil and everything in between*, *Nature Education Knowledge* **4** (2013) 3.

[16] R. Golestanian, T. B. Liverpool, and A. Ajdari, *Propulsion of a Molecular Machine by Asymmetric Distribution of Reaction Products*, *Physical Review Letters* **94** (6, 2005) 220801.

[17] J. R. Howse, R. A. L. Jones, A. J. Ryan, T. Gough, R. Vafabakhsh, and R. Golestanian, *Self-Motile Colloidal Particles: From Directed Propulsion to Random Walk*, *Physical Review Letters* **99** (7, 2007) 048102.

[18] S. Sanchez, A. N. Ananth, V. M. Fomin, M. Viehrig, and O. G. Schmidt, *Superfast Motion of Catalytic Microjet Engines at Physiological Temperature*, *Journal of the American Chemical Society* **133** (9, 2011) 14860–14863.

[19] R. Soto and R. Golestanian, *Self-Assembly of Catalytically Active Colloidal Molecules: Tailoring Activity Through Surface Chemistry*, *Physical Review Letters* **112** (2, 2014) 068301.

[20] X. Ma, A. Jannasch, U.-R. Albrecht, K. Hahn, A. Miguel-López, E. Schäffer, and S. Sánchez, *Enzyme-Powered Hollow Mesoporous Janus Nanomotors*, *Nano Letters* **15** (10, 2015) 7043–7050.

[21] X. Ma, K. Hahn, and S. Sanchez, *Catalytic Mesoporous Janus Nanomotors for Active Cargo Delivery*, *Journal of the American Chemical Society* **137** (4, 2015) 4976–4979.

[22] R. Dreyfus, J. Baudry, M. L. Roper, M. Fermigier, H. A. Stone, and J. Bibette, *Microscopic artificial swimmers*, *Nature* **437** (10, 2005) 862–865.

[23] A. Bricard, J.-B. Caussin, D. Das, C. Savoie, V. Chikkadi, K. Shitara, O. Chepizhko, F. Peruani, D. Saintillan, and D. Bartolo, *Emergent vortices in populations of colloidal rollers*, *Nature Communications* **6** (11, 2015) 7470.

[24] T. Bhattacharjee and S. S. Datta, *Bacterial hopping and trapping in porous media*, *Nature Communications* **10** (12, 2019) 2075.

[25] S. J. Kron and J. A. Spudich, *Fluorescent actin filaments move on myosin fixed to a glass surface.*, *Proceedings of the National Academy of Sciences* **83** (9, 1986) 6272–6276.

[26] A. Månsson, *The potential of myosin and actin in nanobiotechnology*, *Journal of Cell Science* **136** (3, 2023) jcs261025.

[27] G. Saper and H. Hess, *Synthetic systems powered by biological molecular motors*, *Chemical Reviews* **120** (9, 2019) 288–309.

[28] J. F. Brady, *The long-time self-diffusivity in concentrated colloidal dispersions*, *Journal of Fluid Mechanics* **272** (1994) 109–134.

[29] H. C. Berg, *Random Walks in Biology*. Princeton University Press, 12, 1984.

[30] C. Brennen and H. Winet, *Fluid mechanics of propulsion by cilia and flagella*, *Annual Review of Fluid Mechanics* **9** (1, 1977) 339–398.

[31] T. Ishikawa, *Fluid dynamics of squirmers and ciliated microorganisms*, *Annual Review of Fluid Mechanics* **56** (1, 2024) 119–145.

[32] J. L. Moran and J. D. Posner, *Phoretic self-propulsion*, *Annual Review of Fluid Mechanics* **49** (1, 2017) 511–540.

[33] S. C. Takatori and J. F. Brady, *Forces, stresses and the (thermo?) dynamics of active matter*, *Current Opinion in Colloid &; Interface Science* **21** (2, 2016) 24–33.

Chapter 2

Predicting the Dispersion of Active Matter in Porous Media

Physical boundaries play a key role in governing the overall transport properties of nearby self-propelled particles. In this chapter, we develop dispersion theories and conduct Brownian dynamics simulations to predict the coupling between surface accumulation and effective diffusivity of active particles in boundary-rich media. We focus on three models that are well-understood for passive systems: particle transport in (i) an array of fixed volume-excluding obstacles; (ii) a pore with spatially heterogeneous width; and (iii) a tortuous path with kinks and corners. While the impact of these entropic barriers on passive particle transport is well established, we find that these classical models of porous media flows break down due to the unique interplay between activity and the microstructure of the internal geometry. We study the activity-induced slowdown of effective diffusivity by formulating a Smoluchowski description of long-time self diffusivity which contains contributions from the density and fluctuation fields of the active particles. Particle-based and finite element simulations corroborate this perspective and reveal important nonequilibrium considerations of active transport.

This chapter includes content from our previously published article:

[1] K. J. Modica, A. K. Omar, and S. C. Takatori, *Boundary design regulates the diffusion of active matter in heterogeneous environments*, *Soft Matter* **19** (2, 2023), no. 10 1890–1899. KJM and SCT conceived of the study; all authors designed research; KJM performed simulations and analytical calculations; SCT supervised the study; and all authors wrote the paper.

2.1 Introduction

Porous media guides species transport through a combination of enthalpic and entropic interactions [2, 3]. In this chapter, we will focus our attention on entropic,

excluded-volume interactions between diffusing particles and hard external boundaries. Introducing even a dilute concentration of immobile obstacles with purely excluded-volume interactions can provide a substantial slowdown to diffusive flux [4–6]. While self-propelled bacteria move via nonequilibrium forcing, recent research has found success in describing swimmers as Brownian particles under a higher effective temperature and swim energy $k_{\mathrm{s}}T_{\mathrm{s}}$. This is then translated to a bulk diffusivity using the drag coefficient ζ by means of a modification to the Stokes-Einstein-Sutherland relation: $D_0 = (k_{\mathrm{B}}T + k_{\mathrm{s}}T_{\mathrm{s}})/\zeta$.

This effective temperature approach is an approximation of the true nonequilibrium behavior, but it has shown success in predicting swim pressure, bulk self-diffusivity, and the energy transferred to a tracer in an active bath [7–10]. For an active Brownian particle (ABP), one can define the swim energy in 2D [11]: $k_{\mathrm{s}}T_{\mathrm{s}} = \zeta U_0^2 \tau_R/2$. This corresponds to a long time self diffusivity of $D_0 = D_T + U_0^2\tau_R/2$, where $D_T = k_{\mathrm{B}}T/\zeta$ is the thermal diffusivity, U_0 is the self-propulsive velocity, τ_R is the reorientation time, and $D_R = 1/\tau_R$ is the rotational diffusion coefficient [12]. The effective temperature ansatz has been successful in describing the diffusivity of free suspensions; however, it may break down in the presence of excluded volume interactions or external boundaries. Boundaries are especially important for active matter systems due to their activity-induced enrichment along surfaces. Unlike passive (equilibrium) Brownian particles, active particles accumulate at boundaries due to their persistent motion, even in the absence of particle-boundary attraction [8, 13–17].

Many researchers have examined how confinement influences the behavior of self-propelled colloidal particles [6, 18–24]. In arrays of fixed obstacles, specific swimmer models and geometries allow one to observe subdiffusive [25, 26] and superdiffusive [27] transport. Increased concavity and surface area enhances the partitioning of ABPs at boundaries and perturbs the microstructure further from Boltzmann statistics [28, 29]. We hypothesize that the transport properties of active matter can be tuned by the careful

control of porous media microstructure, just as the steady-state properties can. We have recently determined that variations in boundary curvature reduces the mobility of nearby swimmers [29], but it is unclear how the design of porous materials reduces the macroscopic transport of swimmers from their well-known bulk diffusivity. Classical theories of diffusive transport in porous media rely on averaging over local degrees of freedom to find the effective diffusivity, D_E. These theories are accurate for a dilute suspension of passive Brownian particles that exhibit no accumulation on surfaces; however, their applicability to self-propelled swimmers is unclear.

In this chapter, we demonstrate that existing theories of porous media transport fail due to the accumulation of active swimmers on boundaries. Boundaries create significant, long-ranged disturbances to the distribution of active particles; we show that these disturbances correspond to a reduced scaled diffusivity in boundary-rich media.

2.2 Langevin and Smoluchowski Models

We design three representative examples of distinct porous media to interrogate the accuracy of the corresponding equilibrium-based model with the transport of active Brownian particles (Figure 2.1).

First, in Fig. 2.1A, we consider a lattice array of circular 2D inclusions. For a dilute concentration of inclusions, the swimmers collide with the hard boundaries and then escape without difficulty, leading to a minor slowdown that depends on the obstacle density and size. Second, in Fig. 2.1B, we consider the transport across a narrow constriction. This constriction can be considered as the limit of dense packing for a lattice array of obstacles. Finally, in Fig. 2.1C, we consider the diffusion along a tortuous path that represents a simple model of a porous network. Each model system is designed to test how the geometry-dependent accumulation of active particles cause deviations in classi-

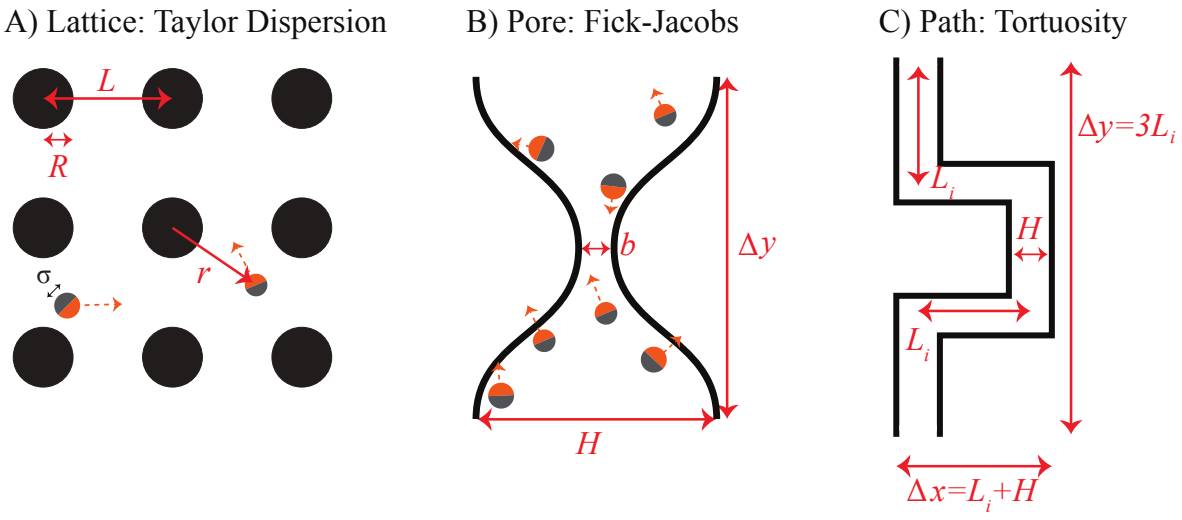

Figure 2.1: **Diagrams of the three sample systems used to probe diffusivity models. A)** An infinite lattice of hard spheres, used to study generalized Taylor dispersion theory. **B)** A narrow pore of varying constriction, used to probe Fick-Jacobs approximations. **C)** A winding path, used to test the applicability of tortuosity relations.

cal theories developed for passive Brownian systems. We focus on the transport of dilute ABPs in rigid, 2D porous media, such as swimmers in confined microfluidic devices, but our qualitative results and framework apply in 3D as well.

An ABP particle i follows the overdamped Langevin equation with a swim force of constant magnitude and white noise Brownian forces and torques [30–33]. To simulate a dilute system, the ABPs interact with obstacles via a purely repulsive potential, but do not interact with each other (i.e., the particles are "ideal").

$$\frac{d\boldsymbol{x}_i}{dt} = \sqrt{2D_T}\boldsymbol{\eta}_i(t) + \frac{\boldsymbol{F}_{i,rep}(\boldsymbol{R_i})}{\zeta} + \frac{\boldsymbol{F}_{i,swim}}{\zeta} \tag{2.1a}$$

$$\frac{d\theta_i}{dt} = \sqrt{2D_R}\xi_i(t). \tag{2.1b}$$

Here, $\boldsymbol{F}_{i,rep}$ is the repulsive force on particle i from the boundary excluded volume, ζ is the drag coefficient, and $\boldsymbol{F}_{i,swim}$ is the swim force. The swim force is set as $\boldsymbol{F}_{i,swim} = U_0\zeta\boldsymbol{q}_i$, where $\boldsymbol{q}_i = [\cos\theta_i, \sin\theta_i]$ is the unit vector describing particle i's orientation in 2D. Finally, the thermal and rotational diffusion coefficients are D_T and $D_R = 1/\tau_R$, with $(\boldsymbol{\eta}_i,\ \xi_i)$

as random variables obeying the zero mean and variance consistent with the fluctuation-dissipation theorem. The obstacle-particle repulsive force $\boldsymbol{F}_{i,rep}$ is implemented using the Weeks-Chandler-Andersen (WCA) [34] potential on overlapping spheres defining the obstacle surface (see Supplementary Information of [1] for details). We find the effective diffusivity tensor ($\boldsymbol{D}_E$) of an ABP in the porous medium from the slope of the mean squared displacement (MSD) at long times.

$$\boldsymbol{D}_E = \frac{1}{2}\lim_{t\to\infty}\frac{d}{dt}\left(\frac{1}{N}\sum_{i}^{N}\Delta\boldsymbol{x}_i(t)\Delta\boldsymbol{x}_i(t)\right) \tag{2.2}$$

As a complementary description of the Langevin equation, the probability distribution $P(\boldsymbol{x},\boldsymbol{q},t)$ of a single ABP at position $\boldsymbol{x}$ and orientation $\boldsymbol{q}$ in porous media can be studied using a dimensionless Smoluchowski equation:

$$\frac{\partial P}{\partial \tilde{t}} + \tilde{\nabla}\cdot\boldsymbol{j}_T - \frac{\partial^2 P}{\partial\theta^2} = 0 \tag{2.3a}$$

$$\boldsymbol{j}_T = \left(\frac{\ell}{L}\right)\boldsymbol{q}P - \left(\frac{\delta}{L}\right)^2\tilde{\nabla}P \tag{2.3b}$$

with the $\tilde{t} = t/\tau_R$, $\tilde{\boldsymbol{x}} = \boldsymbol{x}/L$, $\tilde{\nabla} = L\nabla$. We impose a no-flux boundary condition on any obstacle surface. Time is scaled by the reorientation time τ_R, and distance is scaled by a geometric feature of length L. In principle, $\boldsymbol{F}_{rep}(\boldsymbol{x})$ should also appear, but we are assuming hard excluded volume interactions which can be implemented as boundary conditions. This form of nondimensionalization introduces two important length scales. The run length $\ell = U_0\tau_R$ is the average distance an ABP self-advects before reorienting and the microscopic length $\delta = \sqrt{D_T\tau_R}$ is the root mean squared distance an ABP travels by thermal motion before reorienting. These represent the strength of active and thermal forces, respectively.

Taking orientational moments of the full Smoluchowski equation turns Eq. 2.3 into an infinite series of coupled conservation equations [35]. The density field $n(\boldsymbol{x},t) \equiv$

$\int P(\boldsymbol{x}, \boldsymbol{q}, t)\boldsymbol{dq}$ depends on the polar order, $\boldsymbol{m}(\boldsymbol{x}, t) \equiv \int P\boldsymbol{q}\mathrm{d}\boldsymbol{q}$, which depends on the nematic order, $\boldsymbol{Q}(\boldsymbol{x}, t) \equiv \int P\boldsymbol{q}\boldsymbol{q}\mathrm{d}\boldsymbol{q}$, and so on. We solve Eq. 2.3 numerically and take orientational moments of the solution to calculate the effective translational diffusivity using methods discussed in the following section. We will examine these equations using the list of relevant length scales shown in Table 2.1.

Table 2.1: Table of relevant length scales for active matter in boundary-rich materials

Length	Formula	Description
ℓ	$U_0\tau_R$	Run length of a free ABP.
δ	$\sqrt{D_T\tau_R}$	Thermal diffusive distance moved over one reorientation.
λ^{-1}	$\delta/\sqrt{1+\frac{1}{2}(\ell/\delta)^2}$	Screening length of ABP boundary layer.
σ	N/A	Diameter of the ABP $\sigma \ll R, L, H, b$
R, L, H, b	N/A	Material length scales

2.3 Case Studies of Porous Structures

2.3.1 Diffusion Around Rigid Inclusions

Background

Porous materials can be modelled as a continuous fluid interspersed with discrete rigid inclusions. As a model system, we study a repeating square lattice of disks of radius R and excluded area fraction $\phi = \rho\pi R^2$, where ρ is the disk number density.

For passive Brownian particles in a high porosity lattice ($\phi \ll 1$), as in Figure 2.2A, the effective diffusivity decreases linearly with the area density of obstacles $D_E/D_T = (1-\phi) + \mathcal{O}(\phi^2)$ [36, 37], and has been solved to arbitrary order using series solutions[4]. If the active particles are equivalent to passive Brownian particles at a higher effective temperature, their reduced diffusivity should track the series solution after replacing D_T

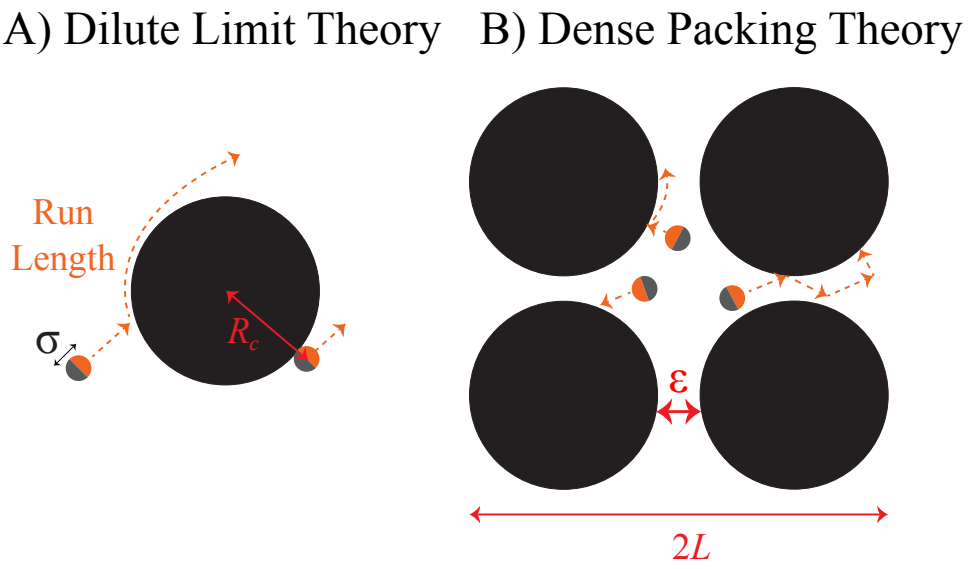

Figure 2.2: **Diffusivity of swimmers in a lattice array depends strongly on the obstacle density. A)** At high porosity, diffusivity decreases linearly with obstacle area density ϕ. The radius of the disk is defined as the volume excluded to the ABP $R_c = R_{disk} + \sigma/2$. In all our results, we keep σ constant and simplify notation by $R = R_c$. **B)** At dense packing, ABPs are trapped in small pockets with narrow escape domains of size ϵ. The lattice is made of disks centered in a unit cell of length L.

with $D_0 = D_T + U_0^2\tau_R/2$.

In addition to Brownian dynamics simulations, we numerically solve Eq. 2.3 using generalized Taylor dispersion theory [4, 6, 38–42]. We obtain the effective velocity vector $\boldsymbol{u}_E$ and diffusivity tensor $\boldsymbol{D}_E$ of the active particles by splitting the full distribution into local and global contributions. The ABPs position vector $\boldsymbol{x}$ is defined as the sum of the global unit cell vector ($\boldsymbol{X}$) and the local position inside the unit cell ($\boldsymbol{r}$). For a particle that enters an $L \times L$ unit cell containing a central obstacle, the normalized probability density of finding a particle at position $\boldsymbol{r}$ and orientation $\boldsymbol{q}$ at time t is denoted as $g_0(\boldsymbol{r}, \boldsymbol{q}, t)$. Particle density fluctuations due to the presence of obstacles give rise to an effective diffusivity that is distinct from the bulk diffusivity D_0. The strength and direction of these density fluctuations is measured by the fluctuation field $\boldsymbol{d}(\boldsymbol{r}, \boldsymbol{q}, t)$. Equations are kept in dimensional form for clarity. (see Supplementary Information of

[1] for full derivation):

$$0 = \frac{\partial g_0(\boldsymbol{r}, \boldsymbol{q}, t)}{\partial t} + \nabla_r \cdot [U_0 \boldsymbol{q} g_0 - D_T \nabla_r g_0] - D_R \frac{\partial^2 g_0}{\partial \theta^2} \tag{2.4a}$$

$$\begin{aligned} \mathbf{0} = \frac{\partial \boldsymbol{d}(\boldsymbol{r}, \boldsymbol{q}, t)}{\partial t} + [U_0 \boldsymbol{q} g_0 - D_T \nabla_r g_0] + \nabla_r \cdot [U_0 \boldsymbol{q} \boldsymbol{d} \\ - D_T (\boldsymbol{I} g_0 + \nabla_r \boldsymbol{d})] - D_R \frac{\partial^2 \boldsymbol{d}}{\partial \theta^2} \end{aligned} \tag{2.4b}$$

where ∇_r indicates the gradient operator over the local position variable r.

We solve these equations at steady state subject to no-flux boundary conditions along the surface of the inclusion, periodic boundary conditions at the unit cell edges, and normalization constraints $\langle g_0 \rangle_{q,r} = 1$,$\langle \boldsymbol{d} \rangle_{q,r} = \mathbf{0}$ using the finite element method. Where $\langle \bullet \rangle_{m,n} = \int (\bullet)\, \mathrm{d}m\mathrm{d}n$. We use the steady state solutions to compute the average effective velocity $\boldsymbol{u}_E$ and diffusivity $\boldsymbol{D}_E$ of the system:

$$\boldsymbol{u}_E = U_0 \langle \boldsymbol{q} g_0 \rangle_{q,r} - D_T \langle \nabla_r g_0 \rangle_{q,r} \tag{2.5a}$$

$$\boldsymbol{D}_E = D_T \boldsymbol{I} - U_0 \langle \boldsymbol{q} \boldsymbol{d} \rangle_{q,r} + D_T \langle \nabla_r \boldsymbol{d} \rangle_{q,r}. \tag{2.5b}$$

Results

In Fig. 2.3A, we summarize the results of our Brownian dynamics simulations and dispersion theory calculations. In the limit of high porosity ($\phi \to 0$), the microstructure of the ABPs is weakly perturbed from that of a uniform suspension. The self-diffusivity decreases linearly with obstacle volume fraction ϕ as described by effective temperature theories: $D_E = D_0(1 - \phi)$. However, as demonstrated in Fig. 2.3A, the initial slope of the scaled diffusivity varies for highly active particles ($\ell \gg \delta$ or $\ell \gg R$). The effective temperature expression only holds for obstacles spaced far enough apart that the ABPs interact with at most one obstacle over many reorientation times. Therefore, as the activity increases, the effective temperature is restricted to a smaller and smaller ϕ.

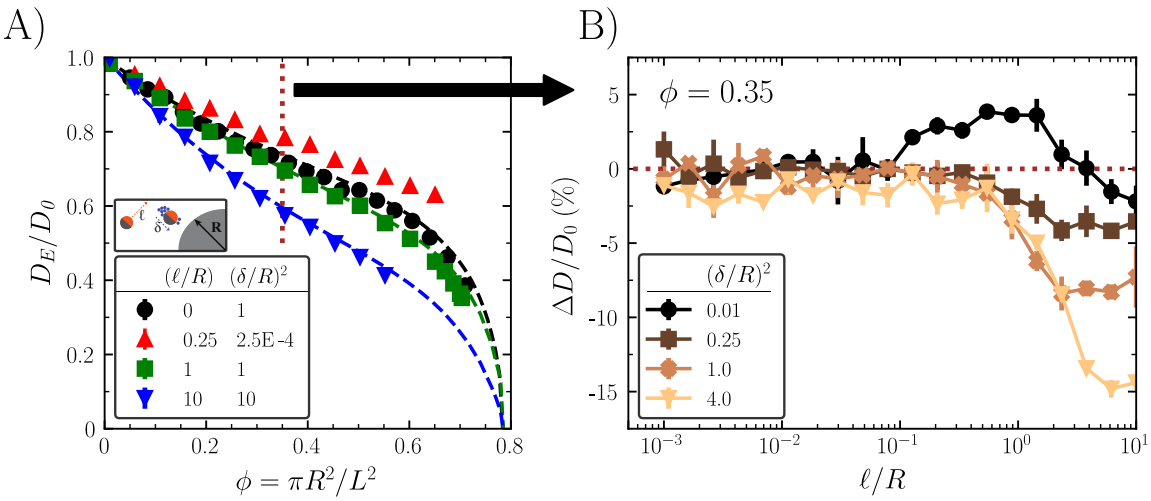

Figure 2.3: **The effective diffusivity of active swimmers depends non-monotonically on the run length (ℓ) and the microscopic length (δ).** **A)** Scaled diffusivity for an infinite square lattice as a function of obstacle volume density. The 4 sets represent example leaflets generated by varying particle activity. Points are Brownian dynamics simulations data, dashed lines are numerical solutions to dispersion theory. Dispersion theory calculations are not included for $\ell/R = 0.25$, $\delta^2/R^2 = 2.5\text{E-}4$ because the large relative activity $\ell \gg \delta$ generates a sharp boundary layer along the obstacle surface that is numerically challenging to resolve. **B)** Activity has a nonmonotonic effect on scaled diffusivity due to boundary layer coupling. Scaled diffusivity deviation as a function of run length and for various microscopic length at constant area fraction $\phi = 0.35$. Error bars in **A** and **B** are the standard deviation from 3 independent simulations, and when not visible are smaller than the marker size.

As the obstacle density increases, the diffusivities diverge from those predicted by the effective temperature theory. At intermediate obstacle densities, $\phi \approx 0.1 - 0.7$, the relative microscopic length (δ) and run length (ℓ) become important predictors of scaled diffusivity. While each curve monotonically decreases with higher obstacle density, at high activities there can be large deviations from the effective temperature theory.

Finally, as the system approaches close packing, $\phi \to \pi/4$, the diffusivities rapidly decrease to zero due to particle transport being limited by a narrow escape through a small pore.

To further examine the effect of run length and microscopic length on active transport

at intermediate obstacle densities, $\phi \approx 0.1 - 0.7$, we define the normalized deviation in measured diffusivity from the model's expected effective temperature diffusivity D_{Model} as the quantity $\Delta D/D_0$:

$$\frac{\Delta D}{D_0} = \frac{D_E - D_{\text{Model}}}{D_0} \tag{2.6}$$

This quantity measures the deviation in diffusivity the real ABPs experience compared to that predicted for a Brownian particle in the same system at a higher effective temperature. Therefore, Eq. 2.6 isolates the true coupling between activity-induced boundary accumulation and the obstacle-driven slowdown.

In Fig. 2.3B, we show the diffusivity deviation for a fixed obstacle density, $\phi = 0.35$, while varying both the run length and microscopic length of the ABPs. For weak activity, $\ell/R \ll 1$, the scaled diffusivity matches the expected results from the passive limit, leading to minimal departure from D_{Model}. As activity increases beyond $\ell/R \approx 1$, the effective temperature theories no longer hold. Reductions in transport coefficients are reflected through the increased accumulation within the boundary layer. Strongly active particles are "trapped" within the boundary layer until they reorient or slide off. In contrast, when activity is weak, translational Brownian fluctuations dominate and carry the ABP away from the boundary layer before reorientation occurs. Inactive or weakly active particles "forget" the obstacle surface much faster than their reorientation time or sliding time. As ℓ/R increases, more ABPs accumulate on the surface. While increasing $(\delta/R)^2$ may *decrease the magnitude of surface accumulation*, it also *increases the boundary layer thickness*, resulting in a net slowdown of scaled ABP diffusivity over the range of parameters studied.

Interestingly, for very small values of the microscopic length [$(\delta/R)^2 = 0.01$ in Fig. 2.3B], we see an enhancement in scaled diffusivity beyond the passive theory. We

suspect this is due to the unique geometry of the square lattice. When Brownian fluctuations are small in a square lattice, the particles exhibit sustained runs in the interstitial space, effectively lowering the number of obstacles an ABP runs into in a manner similar to the enhancement described by Pattanayak et al. [43].

The boundary-induced accumulation of ABPs occurs over a boundary layer [13] of size λ^{-1}:

$$\lambda^{-1} = \frac{\delta}{\sqrt{1 + \frac{1}{2}(\frac{\ell}{\delta})^2}} \tag{2.7}$$

In Fig. 2.4, we show contour plots to connect the ABP microstructure and the diffusivity reduction discussed previously. Figures 2.4A and 2.4D are the passive case, and exhibit a uniform density field in space. Moving across the top row of Fig. 2.4A-C, both the boundary layer width and strength are growing, leading to higher relative number of active particles that are influenced by the obstacle before moving to the bulk. The second row of Fig. 2.4D-F shows the corresponding local diffusivity deviation determined via Taylor dispersion theory that is then averaged over the free space to obtain the normalized effective diffusivity deviation $\Delta D/D_0$. As activity increases across Fig. 2.4D-F, the local diffusivity decreases in regions near the obstacle surface due to ABPs accumulating within the boundary layer. When an active swimmer is moving unobstructed through the bulk fluid, it spreads with its swim diffusivity D_0. The local diffusivity is quadrupolar near the obstacle, showing reductions at the surface along the axis of motion (in this case the left and right for D_{xx}), and enhancements above and below due to sliding. The increased surface accumulation in 2D along a weakly curved obstacle with curvature $1/R$ is described by [28]:

$$\frac{n^{surf}}{n^{\infty}} = 1 + \frac{\ell^2}{2\delta^2} - \frac{\ell^2\lambda}{R} + \mathcal{O}\left(\frac{\ell^2\lambda}{R}\right)^2 \tag{2.8}$$

At a constant density, larger obstacles and activities increase the surface accumulation, which perturbs the behavior of the ABPs away from the effective temperature theory

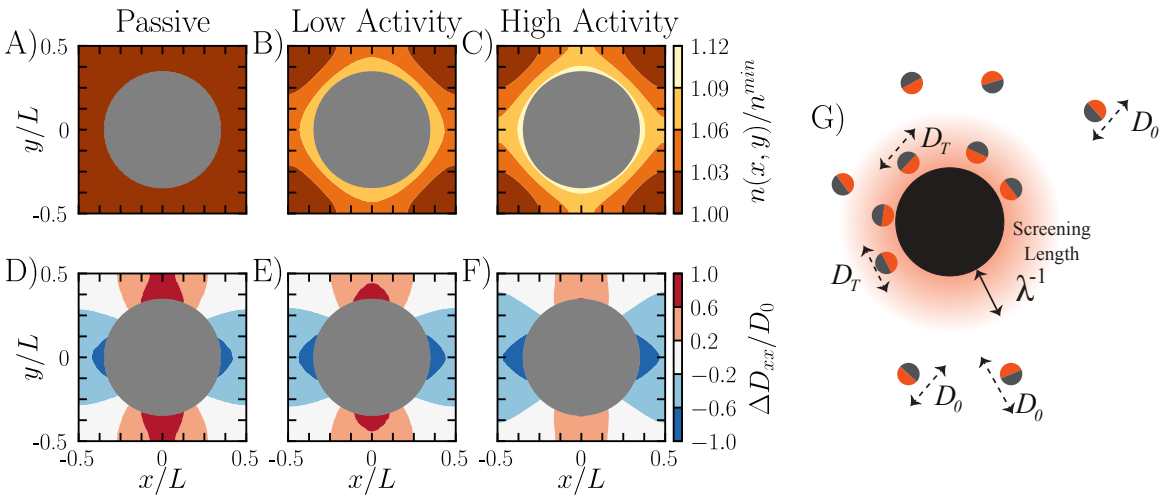

Figure 2.4: **Surface accumulation leads to slowdowns in scaled diffusivity.**. **A-C)** Local number density of particles for different activity parameters. As the activity increases in strength, the particles experience larger accumulation near the obstacle surface as shown through the contours. **D-F)** Pointwise diffusivity deviation along the x direction calculated numerically via dispersion theory (see Supplementary Information of [1] for more details). The pointwise diffusivity deviation is $\Delta D_{xx}/D_0 = \left(D_{xx}(x,y) - D_{\text{Model}}\right)/D_0$. The pointwise diffusivity has a quadrupolar form due to particles getting trapped in the leading and trailing wakes of the obstacles. **G)** Cartoon demonstrating that ABPs within the boundary layer move with a reduced diffusivity compared to the ABPs in the bulk. Subplots **A,D** correspond to $\ell/R = 0$ and $\delta^2/R^2 = \text{N/A}$. Subplots **B,E** correspond to $\ell/R = 1$ and $\delta^2/R^2 = 1$. Subplots **C,F** correspond to $\ell/R = 10$ and $\delta^2/R^2 = 10$. All data collected for $\phi = 0.38$

described by $k_{\text{s}}T_{\text{s}}$.

Figure 2.4G is a schematic demonstrating the relationship between surface accumulation and transport reduction. For ABPs inside the boundary layer, their self-propulsive force is directed inward against the wall. These ABPs are trapped against the surface until they reorient, and are therefore only diffusing by thermal motion until they escape. This indicates that there are three domains relevant to ABP transport through a packed bed: the occupied area of obstacles ϕ, the boundary layer around obstacles ϕ_{BL} (which must be weighted by the fraction of ABPs partitioned inside the boundary layer), and

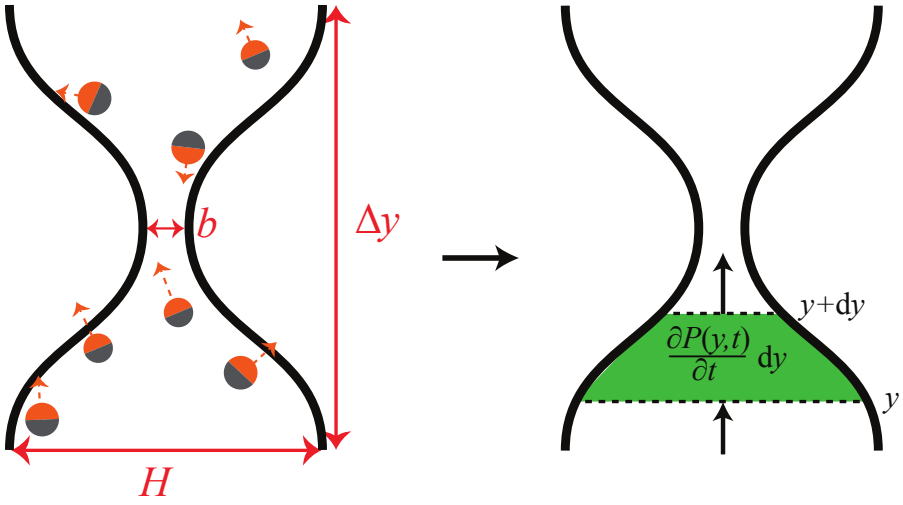

Figure 2.5: **Schematic of the periodic narrow pore used to describe the Fick-Jacobs approximation.**

then the bulk space ϕ_{Free}.

Within each of these domains, the ABP moves with a different effective diffusivity. Outside the boundary layer, an ABP in ϕ_{Free} does not feel any boundary effects and moves with bulk diffusivity D_0. Inside the boundary layer ϕ_{BL}, an ABP is slowed by collisions with the obstacles, and moves with a local diffusivity approximately equal to D_T. Finally, for impenetrable obstacles no transport can occur and therefore the diffusivity is zero.

2.3.2 Diffusion Through a Narrow Pore

Background

Taylor dispersion theory is a powerful tool to predict transport properties for dilute systems; however, analytical treatment becomes intractable as the packing density approaches the percolation threshold. Additionally, due to the close packing, the active boundary layers become numerically challenging to resolve. For all of these reasons,

we use a simpler Fick-Jacobs [44, 45] model of the diffusion reduction due to narrow constriction sites.

The Fick-Jacobs equation describes diffusion in a channel with a slowly varying cross section of width $w(y)$, $\left|\frac{\partial w(y)}{\partial y}\right| \ll 1$. Utilizing the methods described by Rubí and Reguera [46, 47], we consider the flux of Brownian particles through a thin pore as a 1D problem, with local variations in transverse width as an "entropic force". For a Brownian particle, the Fick-Jacobs equation is:

$$\frac{\partial P(y,t)}{\partial t} = \frac{\partial}{\partial y}\left[D_T \frac{\partial P}{\partial y} - D_T P \frac{\partial \ln w}{\partial y}\right], \tag{2.9}$$

See Supplementary Information of [1] for the full derivation. The Fick-Jacobs model connects the geometry of the pore with thermodynamic potentials; the constrictions and extensions of the boundaries create entropic traps of the form $V_{eff} = -k_{\mathrm{B}} T \ln(w)$ that reduce the axial flux. Rubí and Reguera [46, 47] show that the applicability of the 1D Fick-Jacobs equation can be extended via the introduction of a heuristically defined position dependent diffusion coefficient

$$D(y) = \frac{D_0}{[1 + (1/4)w'(y)^2]^{1/3}} \tag{2.10}$$

with the scaling exponent 1/3 used to empirically match a series solution developed by Zwanzig [45].

As shown earlier, if the self-propelled particles behave as Brownian particles at a higher effective temperature, one should be able to replace their thermal diffusivity with their bulk diffusivity, $D_0 = D_T + U_0 \tau_R/2$. This expression can be used to find the one-dimensional axial effective diffusivity by using the Lifson-Jackson formula [48] for motion in a periodic potential described by our entropic barrier

$$\frac{1}{D_E} = \langle w(y) \rangle_y \left\langle \frac{1}{D(y) w(y)} \right\rangle_y . \tag{2.11}$$

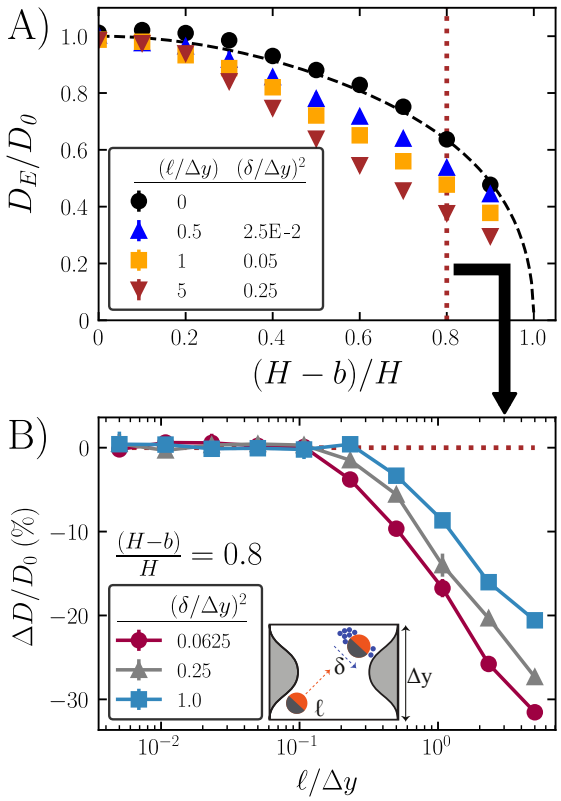

Figure 2.6: **Fick-Jacobs (FJ) theory overestimates the ABP scaled diffusivity. A)** ABP diffusivity decreases below the Brownian reference due to high accumulation along the concave regions of the boundary. $(H-b)/H$ is the degree of constriction due to increased amplitude of pore perturbations (sinusoidal amplitude). The case of $H = b$ corresponds to two flat plates, whereas at $b = 0$ the pore walls are touching and passage is impossible. The black dashed line is the FJ theory estimate. The data points are from simulations of ABPs. **B)** Diffusivity deviation of the ABPs from the Brownian FJ theory. For all simulations, we keep the max wall-wall distance constant at $H/\Delta y = 1$ with minimum distance controlled by changing the amplitude of the sinusoid. Lines are to guide the eye. Error bars are the standard deviation from 3 independent simulations, and when not visible are smaller than the marker size.

Results

The accuracy of the Fick-Jacobs (FJ) model is predicated on the assumption of rapid local equilibrium in the transverse direction compared to the axial direction. For passive systems, this assumption holds when variations in channel width are slow compared to diffusive motion ($|w'(y)| \ll 1$). For an active system, particles move ballistically for their

run length $\ell = U_0\tau_R$; therefore, we expect the FJ model to be the most accurate when the pore width varies slowly compared to the run length.

In Fig. 2.6A, we show the scaled diffusivity of several example active particle systems as a function of the nondimensional constriction. As the pore constricts $[(H-b)/H \to 1]$, transport through the small opening is blocked, rapidly reducing the diffusivity down to zero.

In Fig. 2.6B, we plot the scaled diffusivity deviation from the FJ theory as a function of run length and microscopic length. Over the range of parameters studied, FJ theories consistently overestimate the effective diffusivity past $\ell/\Delta y \approx 0.2$, with the exact deviation point depending on the pore amplitude and wavelength. Taylor dispersion theory is not used in Fig. 2.6 due to the high number of finite element meshing points needed to converge the solution at high activities. For example Taylor dispersion theory calculations of weakly active systems, see the Supplementary Information of [1] for 3 contour plots of ABP concentration and local diffusivity deviation in a sinusoidal pore.

Our results corroborate the previous findings by Sandoval and Dagdug [49], who found that a similar overestimation of diffusivity occurred for a zig-zag and semicircular cavity as the swim speed increased. Their work focused on the impact of varying swim speed U_0. However, our findings reveal this deviation is a result of geometric factors with ℓ and δ providing the true measure of activity.

Axial diffusivity is reduced primarily through the high accumulation of active particles along the concave regions of the pore. As demonstrated in Eq. 2.8, surface accumulation depends on the radius of curvature. For concave surfaces, the curvature κ is negative, causing surface accumulation to increase rapidly with more negative values of κ: $n^{surf} \approx 1+\ell^2/2\delta^2-\ell^2\lambda\kappa+\mathcal{O}\left(\ell^2\lambda\kappa\right)^2$. As the amplitude increases, the radius of curvature shrinks, leading to high accumulation at the *concave* valleys, away from the small *convex* pore, thus lowering scaled diffusivity further.

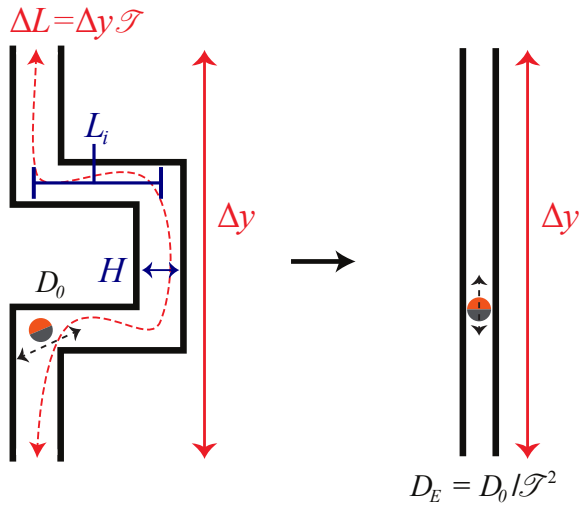

Figure 2.7: **The tortuosity is defined as $\mathcal{T} = \Delta L/\Delta y$, a ratio of the total path length divided by the vertical displacement.** For the tortuous paths considered in this chapter, the center-line path is $\Delta L = 5L_i$ and $\Delta y = 3L_i$, which gives a tortuosity of $\mathcal{T} = 5/3$.

2.3.3 Diffusion Through a Tortuous Path

Background

Porous materials often contain spatial and/or temporal heterogeneities in their microstructure that preclude detailed characterization. To differentiate between multiple materials with the same porosity, catalyst beds and soil sediments are often described with an empirically measured dimensionless tortuosity, $\mathcal{T}$.

Assuming all motion is diffusive, the tortuosity can be determined using a tracer particle of known diffusivity. The relative reduction in measured diffusivity compared to bulk provides an estimate of the reduction factor. Following our definition provided in Fig. 2.7, the ratio of measured diffusivity in the pore to bulk diffusivity is the ratio in paths traveled in the same amount of time; therefore, one can define a nondimensional tortuosity:

$$\mathcal{T}^2 = \left(\frac{\Delta L}{\Delta y}\right)^2 = \frac{D_0}{D_E}. \tag{2.12}$$

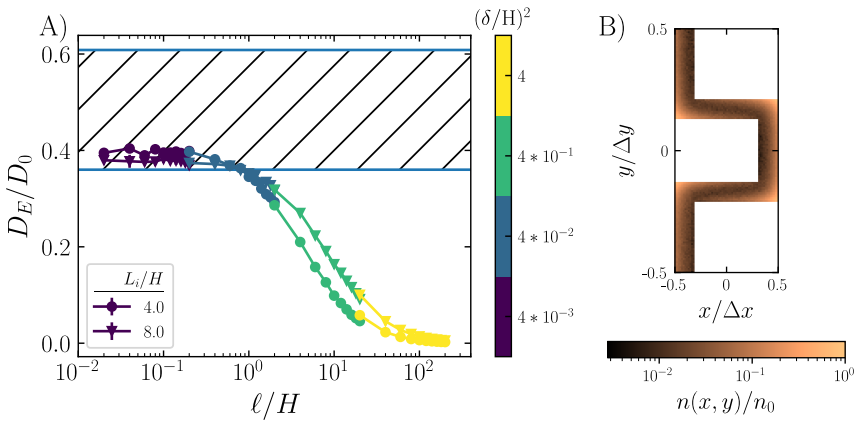

Figure 2.8: **Tortuosity scalings fail as run length increases beyond the channel width.** Brownian dynamics scaled effective diffusivity of active particles confined to the tortuous path. **A**) The scaled diffusivity decreases as the run length increases above the pore width. The different symbols correspond to paths of different aspect ratios. The hatched region represents the expected values described by tortuosity theory. The top line estimates ΔL as the shortest possible path through the maze, and the bottom line estimates ΔL as the path along the pore center-line. **B**) ABPs accumulate significantly at concave corners. The local number density was found via a histogram of particle positions in the Brownian simulation of bin size $0.04\sigma^2$. That histogram was then divided by the max value. When $\ell/H > 1$, strong corner accumulation decreases the diffusivity far below the tortuosity predictions. This image is from simulation data at $L_i/H = 4$, $\ell/H = 20$, and $\delta^2/H^2 = 4$. Error bars in A) are the standard deviation from 3 independent simulations, and when not visible are smaller than the marker size. Lines are to guide the eye.

In general, the tortuosity $\mathcal{T}$ is system dependent and measured experimentally or via image analysis; however, many models and correlations exist for simple structures[50]. In order to test the validity of the tortuosity effective temperature approach for active systems, we have designed a winding path that allows us to define the tortuosity directly from the geometry. Our system is made of 5 individual segments of length L_i and width H. Covering a vertical displacement $\Delta y = 3L_i$.

Results

In Fig. 2.8A, we show the scaled effective diffusivity measured from active Brownian particle (ABP) simulations. The hatched region between two horizontal lines represents the predictions from the tortuosity theory. The lower bound estimates ΔL as the path through the maze center-line. The upper bound estimates ΔL as the shortest possible path through the maze. While the shortest path changes depending on the geometry, in Fig. 2.8A we derive the diffusivity from the shortest path of the $L_i/H = 4$ geometry. Using the $L_i/H = 8$ geometry would lower the upper bound by 20%; therefore, this choice gives the broadest scaled diffusivity range.

At low activity, the scaled diffusivity matches the prediction from the center-line path $D_E/D_0 \approx 1/\mathcal{T}^2 = 0.36$. This indicates that the diffusion of ABPs roughly follows that of the center-line path, without extreme deviations due to backtracking or strong accumulation.

Our geometry informed tortuosity begins to fail when the run length $\ell = U_0\tau_R$ approaches the same size as either the segment length L_i or pore width H. Motion is still diffusive over the unit cell, but the transport through each individual segment becomes increasingly ballistic. ABPs move along a segment until getting trapped in a corner. Eventually, the ABP reorients enough to hop across the next segment.

At high activities $(\ell/H) \gg 1$, the ABPs move ballistically along a segment until colliding with the corner and then spend a significant amount of time trapped before turning. This ballistic motion leads to the concentration profile shown in Fig. 2.8B. Particles deplete from the convex regions, and accumulate in the highly concave corners. The ballistic motion also increases the effective path length, creating a long-tailed reduction in scaled diffusivity, as shown in Fig. 2.8A. Further exploration of the parameter space (such as $L_i/H \gg 1$ and full sweeps of ℓ/H at constant $(\delta/H)^2$) can be found in the

Supplementary Information of [1]. Those additional simulations justify our scaling by H instead of L_i, as well as demonstrate that the solutions are relatively insensitive to $(\delta/H)^2$.

Unlike the narrow pore and the fixed obstacle array, the tortuous path never exhibits a complete blockage of flow, meaning that for networks of the type described in this section, a nonzero diffusivity is possible, even for an arbitrarily large number of segments. Changing the channel boundary patterning from flat walls is expected to further decrease diffusivity. Small pockets of local curvature create an effect similar to that of the sinusoidal pore, providing an additional barrier to whatever maze the ABPs must diffuse through. While this chapter focuses on a design with only one possible path, the addition of concave "dead ends" should partition the ABPs away from the optimal path, resulting in a larger relative reduction in diffusivity.

2.4 Discussion

In this chapter, we test the validity of classical geometric scaling laws for diffusion in heterogeneous environments using analytical theory and Brownian dynamics simulations. We find that even mildly active particles have a scaled diffusivity that deviates from simple effective temperature arguments. The nonequilibrium nature of self-propelled particles needs to be carefully considered in transport calculations, just as it must be for phase behavior and surface accumulation.

Through this chapter, we have examined the applicability (or lack thereof) of traditional porous media estimates for effective diffusivity in active matter. While Taylor dispersion theory is rigorous and accurate for all activities, numerical instabilities and analytic intractability create difficulty in practical use. Particle-based simulations allow for a micromechanical explanation of the decrease in scaled diffusivity due to accumulation.

Both the Fick-Jacobs and tortuosity relationships are accurate in the weakly active limit (provided that one includes the swim diffusivity when calculating the bulk diffusivity), but the strong accumulation at boundary layers and ballistic transport on length scales commensurate with the geometry reduce scaled diffusivity beyond predicted amounts. Interestingly, for a packed bed/ lattice, it is possible for ABPs to achieve scaled diffusivity above the passive predictions, and future work aims to understand this intriguing behavior.

Future work on this topic may look at modifications to the effective temperature theory when incorporating it into boundary rich environments. As a first correction, we can utilize the decreased local diffusivity in the boundary layer as $D_E \approx D_0\phi_{Free} + \alpha D_T\phi_{BL}$. With an unknown coefficient α related to the increased partitioning ABPs experience due to boundary curvature.

Previous research by Khatami et al. found that different models of active matter with the same bulk diffusivity have different transport rates when traversing through a maze[51]. They report that run and tumble models have a smaller mean first passage time than active Brownian particles. Additionally, Kurzthaler et. al.[52] found that the introduction of a reorientation mechanism may lead to greater absolute diffusivity when the reversal run length is commensurate with the maximal chord length of a 3D porous medium. These results indicate that porous media may be used as a novel sorting method for mixtures of active particles utilizing different self-propulsion mechanisms.

This work focuses on the introduction of rigid, immobile obstacles and walls, similar to those found in soil sediments and etched microfluidic devices. However, soft porous materials present a rich opportunity for future study. Boundary fluctuations are important for passive transport in mucus, hydrogels, and other polymeric networks [2, 53]. For example, active particles can push through pores smaller than their diameter, if the pore or the particle can deform under thermal or swim forces.

Polymer networks are well-known to reduce the passive (non-motile) particle transport. Steric hindrance, nonspecific interactions (hydrophobicity, electrostatics), and specific interactions (ligand-receptor binding), all play a part to trap foreign debris [2, 3]. While this chapter focused only on the effect of the obstacle excluded volume, other forms of interactions can lead to controllable transport based on the swimmer and obstacle chemistry.

External torques also influence transport in a nontrivial matter. Rod-shaped bacteria can align with the boundaries and with other bacteria to create nematic ordering/ flocking [54]. Chemoattractants, repellents, light sources, and other external fields can influence the favored direction of bacteria in the absence of hard-wall interactions. For example, a random array of point-source repellents can lead to subdiffusive transport in closed spirals [25, 26].

Hydrodynamic interactions can provide qualitative or quantitative changes to active transport [55, 56]. Hydrodynamic coupling to walls leads to strong interactions between swimmers and surfaces, which would further alter the boundary-accumulation effect on transport [57]. Pusher type active matter (like bacteria and sperm) are hydrodynamically driven to align parallel to the walls, while puller types align perpendicular to the walls [58]. In addition, the surface-modified flow field creates a constant torque leading to motion via counterclockwise (for *E. Coli.*) spirals [59].

Finally, in 3D there are additional degrees of freedom a swimmer can use to avoid obstacles. In 2D, close packing of disks precludes transport; however, a close packed bed of monodispersed spheres in 3D is permeable, resulting in a reduced but nonzero diffusivity. Future work in this space would benefit from mean field approximations for the network, in addition to a detailed analysis of the variance of pore sizes.

Bibliography

[1] K. J. Modica, A. K. Omar, and S. C. Takatori, *Boundary design regulates the diffusion of active matter in heterogeneous environments*, *Soft Matter* **19** (2, 2023) 1890–1899.

[2] L.-H. Cai, S. Panyukov, and M. Rubinstein, *Hopping Diffusion of Nanoparticles in Polymer Matrices*, *Macromolecules* **48** (2, 2015) 847–862.

[3] J. Witten and K. Ribbeck, *The particle in the spider's web: transport through biological hydrogels*, *Nanoscale* **9** (2017), no. 24 8080–8095.

[4] M. Mangeat, T. Guérin, and D. S. Dean, *Effective diffusivity of Brownian particles in a two dimensional square lattice of hard disks*, *The Journal of Chemical Physics* **152** (6, 2020) 234109.

[5] M. Saxton, *Anomalous diffusion due to obstacles: a Monte Carlo study*, *Biophysical Journal* **66** (2, 1994) 394–401.

[6] R. Alonso-Matilla, B. Chakrabarti, and D. Saintillan, *Transport and dispersion of active particles in periodic porous media*, *Physical Review Fluids* **4** (4, 2019) 043101, [arXiv:1809.0008].

[7] D. Loi, S. Mossa, and L. F. Cugliandolo, *Effective temperature of active matter*, *Phys. Rev. E* **77** (5, 2008) 051111.

[8] S. C. Takatori and J. F. Brady, *Forces, stresses and the (thermo?) dynamics of active matter*, *Current Opinion in Colloid 'I&' Interface Science* **21** (2, 2016) 24–33.

[9] G. Szamel, *Self-propelled particle in an external potential: Existence of an effective temperature*, *Phys. Rev. E* **90** (7, 2014) 012111.

[10] E. Fodor, C. Nardini, M. E. Cates, J. Tailleur, P. Visco, and F. van Wijland, *How far from equilibrium is active matter?*, *Phys. Rev. Lett.* **117** (7, 2016) 038103.

[11] S. C. Takatori and J. F. Brady, *Towards a thermodynamics of active matter*, *Phys. Rev. E* **91** (3, 2015) 032117.

[12] H. C. Berg, *Random Walks in Biology*. Princeton University Press, 1, 1984.

[13] W. Yan and J. F. Brady, *The force on a boundary in active matter*, *Journal of Fluid Mechanics* **785** (12, 2015) R1, [arXiv:1510.0773].

[14] F. Smallenburg and H. Löwen, *Swim pressure on walls with curves and corners*, *Phys. Rev. E* **92** (9, 2015) 032304.

[15] S. C. Takatori, W. Yan, and J. F. Brady, *Swim pressure: Stress generation in active matter*, *Phys. Rev. Lett.* **113** (7, 2014) 028103.

[16] G. Volpe, S. Gigan, and G. Volpe, *Simulation of the active brownian motion of a microswimmer*, *American Journal of Physics* **82** (2014), no. 7 659–664.

[17] C. M. Kjeldbjerg and J. F. Brady, *Partitioning of active particles into porous media*, *Soft Matter* **18** (2022) 2757–2766.

[18] T. Bhattacharjee and S. S. Datta, *Bacterial hopping and trapping in porous media*, *Nature Communications* **10** (12, 2019) 2075.

[19] L. J. Perez, T. Bhattacharjee, S. S. Datta, R. Parashar, and N. L. Sund, *Impact of confined geometries on hopping and trapping of motile bacteria in porous media*, *Physical Review E* **103** (1, 2021) 012611.

[20] N. A. Licata, B. Mohari, C. Fuqua, and S. Setayeshgar, *Diffusion of Bacterial Cells in Porous Media*, *Biophysical Journal* **110** (1, 2016) 247–257.

[21] V. K. Truong, D. E. Mainwaring, P. Murugaraj, D. H. K. Nguyen, and E. P. Ivanova, *Impact of confining 3-D polymer networks on dynamics of bacterial ingress and self-organisation*, *Journal of Materials Chemistry B* **3** (2015), no. 44 8704–8710.

[22] M. Brun-Cosme-Bruny, E. Bertin, B. Coasne, P. Peyla, and S. Rafaï, *Effective diffusivity of microswimmers in a crowded environment*, *The Journal of Chemical Physics* **150** (3, 2019) 104901.

[23] M. Kumar, J. S. Guasto, and A. M. Ardekani, *Transport of complex and active fluids in porous media*, *Journal of Rheology* **66** (3, 2022) 375–397.

[24] A. Martínez-Calvo, C. Trenado-Yuste, and S. S. Datta, *Active Transport in Complex Environments*, in *Out-of-equilibrium Soft Matter*. The Royal Society of Chemistry, 03, 2023.

[25] O. Chepizhko and F. Peruani, *Diffusion, Subdiffusion, and Trapping of Active Particles in Heterogeneous Media*, *Physical Review Letters* **111** (10, 2013) 160604, [arXiv:1310.0830].

[26] A. Morin, D. Lopes Cardozo, V. Chikkadi, and D. Bartolo, *Diffusion, subdiffusion, and localization of active colloids in random post lattices*, *Physical Review E* **96** (10, 2017) 042611, [arXiv:1702.0765].

[27] M. Zeitz, K. Wolff, and H. Stark, *Active Brownian particles moving in a random Lorentz gas*, *The European Physical Journal E* **40** (2, 2017) 23.

[28] W. Yan and J. F. Brady, *The curved kinetic boundary layer of active matter*, *Soft Matter* **14** (2018), no. 2 279–290, [arXiv:1711.0145].

[29] K. J. Modica, Y. Xi, and S. C. Takatori, *Porous media microstructure determines the diffusion of active matter: Experiments and simulations*, *Frontiers in Physics* **10** (4, 2022) 869175.

[30] M. R. Shaebani, A. Wysocki, R. G. Winkler, G. Gompper, and H. Rieger, *Computational models for active matter*, *Nature Reviews Physics* **2** (4, 2020) 181–199.

[31] C. Bechinger, R. Di Leonardo, H. Löwen, C. Reichhardt, G. Volpe, and G. Volpe, *Active Particles in Complex and Crowded Environments*, *Reviews of Modern Physics* **88** (11, 2016) 045006.

[32] M. C. Marchetti, J. F. Joanny, S. Ramaswamy, T. B. Liverpool, J. Prost, M. Rao, and R. A. Simha, *Hydrodynamics of soft active matter*, *Reviews of Modern Physics* **85** (7, 2013) 1143–1189.

[33] A. P. Solon, M. E. Cates, and J. Tailleur, *Active brownian particles and run-and-tumble particles: A comparative study*, *The European Physical Journal Special Topics* **224** (7, 2015) 1231–1262.

[34] J. D. Weeks, D. Chandler, and H. C. Andersen, *Role of Repulsive Forces in Determining the Equilibrium Structure of Simple Liquids*, *The Journal of Chemical Physics* **54** (6, 1971) 5237–5247.

[35] D. Saintillan and M. J. Shelley, *Instabilities and Pattern Formation in Active Particle Suspensions: Kinetic Theory and Continuum Simulations*, *Physical Review Letters* **100** (4, 2008) 178103.

[36] J. C. Maxwell, *A Treatise on Electricity and Magnetism*. Clarendon Press, 1881.

[37] G. K. Batchelor, *Brownian diffusion of particles with hydrodynamic interaction*, *Journal of Fluid Mechanics* **74** (3, 1976) 1–29.

[38] S. C. Takatori and J. F. Brady, *Swim stress, motion, and deformation of active matter: effect of an external field*, *Soft Matter* **10** (2014), no. 47 9433–9445.

[39] R. N. Zia and J. F. Brady, *Single-particle motion in colloids: force-induced diffusion*, *Journal of Fluid Mechanics* **658** (9, 2010) 188–210.

[40] S. C. Takatori and J. F. Brady, *Superfluid Behavior of Active Suspensions from Diffusive Stretching*, *Physical Review Letters* **118** (1, 2017) 018003.

[41] Z. Peng and J. F. Brady, *Upstream swimming and Taylor dispersion of active Brownian particles*, *Physical Review Fluids* **5** (7, 2020) 073102.

[42] E. W. Burkholder and J. F. Brady, *Tracer diffusion in active suspensions*, *Physical Review E* **95** (5, 2017) 052605.

[43] S. Pattanayak, R. Das, M. Kumar, and S. Mishra, *Enhanced dynamics of active Brownian particles in periodic obstacle arrays and corrugated channels*, *The European Physical Journal E* **42** (5, 2019) 62, [arXiv:1807.0776].

[44] M. H. Jacobs, *Diffusion Processes*. Springer Berlin Heidelberg, Berlin, Heidelberg, 1967.

[45] R. Zwanzig, *Diffusion past an entropy barrier*, *The Journal of Physical Chemistry* **96** (5, 1992) 3926–3930.

[46] D. Reguera and J. M. Rubí, *Kinetic equations for diffusion in the presence of entropic barriers*, *Physical Review E* **64** (11, 2001) 061106.

[47] D. Reguera, G. Schmid, P. S. Burada, J. M. Rubí, P. Reimann, and P. Hänggi, *Entropic Transport: Kinetics, Scaling, and Control Mechanisms*, *Physical Review Letters* **96** (4, 2006) 130603.

[48] S. Lifson and J. L. Jackson, *On the Self-Diffusion of Ions in a Polyelectrolyte Solution*, *The Journal of Chemical Physics* **36** (5, 1962) 2410–2414.

[49] M. Sandoval and L. Dagdug, *Effective diffusion of confined active Brownian swimmers*, *Physical Review E - Statistical, Nonlinear, and Soft Matter Physics* **90** (12, 2014) 062711.

[50] L. Shen and Z. Chen, *Critical review of the impact of tortuosity on diffusion*, *Chemical Engineering Science* **62** (7, 2007) 3748–3755.

[51] M. Khatami, K. Wolff, O. Pohl, M. R. Ejtehadi, and H. Stark, *Active Brownian particles and run-and-tumble particles separate inside a maze*, *Scientific Reports* **6** (12, 2016) 37670.

[52] C. Kurzthaler, S. Mandal, T. Bhattacharjee, H. Löwen, S. S. Datta, and H. A. Stone, *A geometric criterion for the optimal spreading of active polymers in porous media*, *Nature Communications* **12** (12, 2021) 7088.

[53] I. V. Bodrenko, S. Salis, S. Acosta-Gutierrez, and M. Ceccarelli, *Diffusion of large particles through small pores: From entropic to enthalpic transport*, *The Journal of Chemical Physics* **150** (6, 2019) 211102.

[54] M. Bär, R. Großmann, S. Heidenreich, and F. Peruani, *Self-Propelled Rods: Insights and Perspectives for Active Matter*, *Annual Review of Condensed Matter Physics* **11** (3, 2020) 441–466.

[55] E. Lauga and T. R. Powers, *The hydrodynamics of swimming microorganisms*, *Reports on Progress in Physics* **72** (9, 2009) 096601.

[56] K. Drescher, J. Dunkel, L. H. Cisneros, S. Ganguly, and R. E. Goldstein, *Fluid dynamics and noise in bacterial cell-cell and cell-surface scattering*, *Proceedings of the National Academy of Sciences* **108** (7, 2011) 10940–10945.

[57] S. Rode, J. Elgeti, and G. Gompper, *Sperm motility in modulated microchannels*, *New Journal of Physics* **21** (1, 2019) 013016.

[58] A. P. Berke, L. Turner, H. C. Berg, and E. Lauga, *Hydrodynamic Attraction of Swimming Microorganisms by Surfaces*, *Physical Review Letters* **101** (7, 2008) 038102.

[59] R. G. Winkler and G. Gompper, *Hydrodynamics in Motile Active Matter*, in *Handbook of Materials Modeling*, pp. 1–21. Springer International Publishing, Cham, 2018.

Chapter 3

Sensitivity of Active Particle Diffusivity to Surface Curvature

Active swimmers are known to accumulate along external boundaries owing to their persistent self-motion, resulting in a significant reduction in their effective mobility through heterogeneous and tortuous materials. The dynamic interplay between the slowdown experienced by the active constituents near boundaries and their long-time diffusivity is critical for understanding and predicting active transport in porous media. In this chapter, we study the impact of boundary layer accumulation on the effective diffusivity of active matter by analyzing the motion of active Brownian particles in an array of fixed obstacles. We combine Janus particle experiments, Brownian dynamics simulations, and a theoretical analysis based on the Smoluchowski equation. We find that the shape, curvature, and microstructure of the obstacles play a critical role in governing the effective diffusivity of active particles. Indeed, even at dilute packing fractions of obstacles, ϕ =12%, we observed a 25% reduction in the effective diffusivity of active particles, which is much larger than the hindrance experienced by passive Brownian particles. Our combined experimental and computational results demonstrate a strong coupling between the active force and the porous media microstructure. This chapter provides a framework to predict and control the transport of active matter in heterogeneous materials.

This chapter includes content from our previously published article:

[1] K. J. Modica, Y. Xi, and S. C. Takatori, *Porous media microstructure determines the diffusion of active matter: Experiments and simulations*, *Frontiers in Physics* **10** (4, 2022) 869175. KJM and SCT conceived of the study; KJM and SCT designed research; KJM performed finite element calculations; KJM and YX performed simulations and analyzed data; SCT performed experiments; SCT supervised the study; and KJM, YX, and SCT wrote the paper.

Reproduced with permission from Frontiers in Physics.

3.1 Introduction

The transport of living, colloidal-sized species through crowded environments plays a crucial function in many natural and synthetic processes. For example, the transport of bacteria through soil plays a beneficial role in bioremediation, [2, 3] and novel drug delivery mechanisms seek to utilize the proliferation of *S. typhimurium* to access tumor tissues that have been conventionally out of reach [4, 5]. In contrast, the transport of pathogens into wounds sites and mucosa can lead to life-threatening infections without proper treatment [6–8]. The effective transport properties of bacteria in crowded environments depend on the interplay between the swimmer motility and the boundaries that make up the porous material [9]. Many forms of microscopic life enhance their transport via directed self-propulsion, including *E. coli* bacteria, spermatozoa cells, and *C. reinhardtii* algae [10–12]. In addition to living swimmers, advancements in micro/nanoscale synthesis have also led to the creation of synthetic active particles that are excellent tools in the study of autonomous self-propulsion [13–20]. Understanding the motion of active matter embedded within heterogeneous materials is made especially challenging because the transport is dictated by the complex interactions between the swimmer and the material boundaries. For porous materials composed of polymer networks, particle transport may be affected by steric hindrance, nonspecific interactions (hydrophobicity, electrostatics), and specific interactions (ligand-receptor binding) [21, 22]. This behavior is not unique to polymer networks; introducing even a dilute concentration of immobile obstacles with purely excluded-volume interactions provides a substantial slowdown to diffusive flux [23–25].

In addition to the interactions experienced by non-motile Brownian particles, active particles accumulate at physical boundaries due to their persistent self-motion, characterized by a boundary layer near the surface. This accumulation occurs even in the

absence of attractive interactions; the active particles propel freely until hitting a surface and continue to propel themselves toward the surface until they reorient and escape into the bulk fluid. This behavior has been observed experimentally and in simulations of rods and spheres, both with and without hydrodynamic interactions [26–41]. A mechanistic understanding of how the local accumulation near physical boundaries affects the macroscopic mobility of active matter through heterogeneous and tortuous materials is lacking. In this chapter, we study the impact of boundary accumulation on the effective diffusivity of active matter by analyzing the motion of active Brownian particles (ABPs) in a system of rigid 2D obstacles. The presence of boundaries in active systems reduces the effective long-time self diffusivity by an amount that depends on the average swimming speed (U_0) and the average reorientation time (τ_R). This is in sharp contrast to passive Brownian particles, which do not accumulate along boundaries, and whose effective diffusivity depends primarily on the packing fraction of the obstacles [24, 42].

Many studies on active transport focus on the effect of alignment along surfaces due to steric or hydrodynamic torques aligning the swimmer parallel or perpendicular to boundaries [28, 37, 39, 41, 43–47]. However, a connection between transport and surface accumulation of active matter [29, 33–35, 38, 48, 49] without any imposed torques has not been fully explored. For active systems, the precise shape and curvature of the boundary can have a strong effect on motility induced accumulation [34, 35, 50]. This increased accumulation corresponds to more time spent "trapped" in the boundary layer, which inhibits the transport of active matter in tight pores. Therefore, we hypothesize that active swimmers experience a strong reduction to relative diffusivity in porous media due to the synergistic effects of active boundary accumulation and boundary shape.

While many existing theories predict the diffusive transport of passive Brownian particles through porous media [21, 23, 51–55], the unique accumulation of active matter along boundaries — especially at regions of large curvature — leads to unexpected diffu-

sive slowdowns that are not captured in traditional theories. In this chapter, we combine Janus particle experiments, Brownian dynamics simulations, and theory to demonstrate that the transport of active matter in heterogeneous materials is a strong function of the obstacle shape, curvature, and microstructure. Experimentally, we rely upon optical tracking of active particle trajectories, which has been a powerful tool to study both living and artificial swimmers in porous environments [50, 56–63], and allows for direct comparisons to particle based simulations [64–72]. In addition to advancing our basic understanding of active matter transport, our work provides a mechanism to control the transport of active matter in heterogeneous materials.

3.2 Material and Methods

3.2.1 Experiment Preparation

Lipid-coated silica beads were created by coating silica micro-beads with a supported lipid bilayer (SLB). Small unilamellar vesicles (SUVs) were prepared by rehydrating a lipid sheet composed of a mixture of phospholipids with pure deionized water to a concentration of 0.2 mg/mL. For the Janus particles, we used 1,2-dioleoyl-sn-glycero-3-phos-phocholine (DOPC) with 5% of 1,2-dioleoyl-sn-glycero-3-phospho-L-serine (DOPS) and 0.3% of Atto 488-1,2-dioleoyl-sn-glycero-3-phosphoethanolamine (DOPE-Atto 488) fluorescent dye. For the obstacle particles, we used DOPC with 5% of 1,2-dioleoyl-3-trimethylammonium-propane (DOTAP) and 0.3% of Atto 647-DOPE (DOPE-Atto 647). After rehydrating the lipids for 30 min, the solution was vigorously vortexed, sonicated at low-power (20% power) using a tip sonicator (Branson SFX250 Sonifier). The resulting SUV solution was buffered with a MOPS buffer (50 mM MOPS, 100 mM sodium chloride, pH 7.5). DOPC (catalog number: 850375), DOPS (catalog number: 840035), and

DOTAP (catalog number: 890890) were purchased from Avanti polar lipids. DOPE-Atto 488 and DOPE-Atto 647 were purchased from ATTO-TEC GmbH. Silica microspheres (4.0 µm; catalog code: SS05002 and 6.5 µm; catalog code: SS06N) were purchased from Bangs Laboratories.

Silica microspheres with diameters 4 µm and 6.5 µm were cleaned using a 3:2 mixture of sulfuric acid:hydrogen peroxide (Piranha) for 30 minutes in a bath sonicator, and were spun down at 1000g and washed 3 times before being resuspended in pure water. We fabricated Janus particles from the cleaned 4 µm particles by depositing a monolayer on a glass slide, and coating half of the particle surface with a 2 nm-thick layer of chromium and 8 nm-thick layer of platinum using an E-beam evaporator at a deposition rate of 0.1 $\mathring{A}/s$. To form SLBs on the Janus particles and the beads, 50 µL of SUV solution was mixed gently with 10 µL of clean bead suspension. The bead/SUV mixture was incubated for 15 minutes at room temperature while allowing the beads to sediment to the bottom of the tube. Beads were washed 5 times with pure deionized water by gently adding/removing the liquid without resuspending the beads into solution. We verified the fluidity of the SLB by imaging beads on a glass coverslip at high laser intensity, where the diffusion of labeled lipids was visible after photo-bleaching a small region.

For the 4 µm Janus particles, the SLBs coated only half of the particle surface exposed to clean silica. The side with the platinum did not get coated with an SLB. When these SLB half-coated Janus particles were deposited in a 2% solution of hydrogen peroxide, the particles self-propelled pointing away from their platinum half-coating via self-diffusiophoresis. Since silica is more dense than water, the Janus particles moved in 2D along the bottom of the imaging chamber. Within the time frame of our experimental measurements, we did not observe any significant degradation of the SLB from hydrogen peroxide.

For the 6.5 µm obstacle particles, we obtained a uniform SLB across the entire surface

of the silica bead. We added a positively-charged DOTAP lipid to the SLB to facilitate a strong electrostatic attraction between the obstacle particles and the borosilicate coverslip substrate. We found that most obstacle particles remained fixed along the bottom substrate with no observable Brownian motion. We did not observe any adhesion or fusion of the SLBs between the obstacles and the Janus particles.

The SLB-coated obstacle particles were added into the imaging chamber at a desired density, followed by the SLB half-coated Janus particles. We added 2% hydrogen peroxide into the chamber and conducted time lapse imaging. All imaging was carried out on an inverted Nikon Ti2-Eclipse microscope (Nikon Instruments) using an oil-immersion objective (Apo 60x, numerical aperture (NA) 1.4, oil). Lumencor SpectraX Multi-Line LED Light Source was used for excitation (Lumencor, Inc). Fluorescent light was spectrally filtered with emission filters (515/30 and 680/42, Semrock, IDEX Health & Science) and imaged on a Photometrics Prime 95 CMOS Camera (Teledyne Photometrics). Experimental results presented in this chapter are an average over 6 independent replicates of systems with obstacles and 3 independent replicates of systems without obstacles as a control.

3.2.2 Particle Tracking in Experiments

To determine the effect of the porous media on transport, we measured the Janus particle trajectories with and without the presence of the fixed obstacles. We used a modified MATLAB script based on IDL code by Crocker and Grier [73] to track the individual Janus particles by identifying each particle center and tracking its trajectory over time using an image stack with one frame taken every second. We removed any macroscopic drifts by enforcing that the mean displacement over all particles was zero at any time. We filtered out any Janus particles that were immobile due to defects of

the particle (defined as moving less than 30 µm over 100 seconds or if it moved in only 1 direction via macroscopic drifts). In all experimental results, we tracked the particles for times $t > 7\tau_R$. We obtained the Janus particle mean swim speed, U_0, and reorientation time, τ_R, using the control experiments in the absence of obstacles. We obtained the mean swim speed by averaging all tracked particles' velocity over time,

$$U_0 = \left\langle \frac{\Delta r}{\Delta t} \right\rangle. \tag{3.1}$$

The mean swim speed was determined to be $U_0 = 0.84 \pm 0.01$ µm/s with the reported error as the standard error of the mean. We obtained the reorientation time by measuring the bulk diffusivity for the control experiment in the absence of obstacles,

$$D_0 = D_T + \frac{U_0^2 \tau_R}{2}, \tag{3.2}$$

where $D_T \approx 0.1$ µm^2/s is the thermal Brownian diffusivity for 4 µm diameter spheres using the Stokes-Einstein-Sutherland relation [74–76]. We note that the thermal Brownian diffusivity is negligible compared to the self-propulsive component. Using the experimental measurement of the bulk diffusivity, $D_0 = 5.1$ µm^2/s, we obtained the reorientation time and it's standard deviation $\tau_R = 14 \pm 2$ s using Eq. 3.2. As a separate measurement, we computed τ_R using the Janus particle orientation autocorrelation in 2D,

$$\langle \boldsymbol{q}(t) \cdot \boldsymbol{q}(0) \rangle = e^{-t/\tau_R}. \tag{3.3}$$

We obtained the Janus particle orientations directly from particle tracking, and we obtained a reorientation time $\tau_R \approx 10s$ using Eq. 3.3. This measurement is similar to the value we obtained using Eq. 3.2, especially considering the difficulty in finding the orientation using the velocity vector. We concluded that the particles are behaving as active Brownian particles in 2D. In principle, the Janus particles are located along a 2D plane but can reorient in 3D. However, the platinum coating makes the catalytic half-surface

more heavy and causes the Janus particles to tilt downwards, making the particle move effectively in 2D. We note that the direction of self-propulsion points away from the platinum half-surface, so the configuration of the platinum half-surface pointing vertically down appears to be an unstable state.

3.2.3 Brownian Dynamics (BD) Simulations

The parameters (U_0,τ_R) obtained from the control experiment are then used as inputs into our Brownian dynamics simulations in Fig. 3.2. In Fig. 3.5, the parameters were chosen as described in the caption. We implemented our simulations using HOOMD-blue, a molecular dynamics (MD) simulation package in Python [77]. We focused on the dilute limit of a single active Brownian particle (ABP) in 2D interacting with fixed hard-sphere obstacles. Hydrodynamic interactions are ignored in these simulations. The ABP model describes a swimmer with constant propulsion force but white noise torques [12, 78–81]. Hard-sphere like interactions between the obstacles and the ABPs were implemented using the Weeks-Chandler-Andersen (WCA) [82] potential (Eq. 3.5). For the nonspherical Cassini Oval, the structure was formed using overlapping rigid surface particles offset so that the surfaces of the particles formed the boundaries of the Cassini Oval.

The ABPs were initialized and integrated according to the overdamped Langevin equations of motion:

$$\frac{d\boldsymbol{x}_i}{dt} = \sqrt{2D_T}\boldsymbol{\eta}_i(t) + \frac{\boldsymbol{F}_{wca}(x_i, x_j)}{\zeta} + U_0\boldsymbol{q} \tag{3.4a}$$

$$\frac{d\theta_i}{dt} = \sqrt{2D_R}\xi_i(t) \tag{3.4b}$$

where $\boldsymbol{F}_{wca}$ is the force on the particle from all potentials and constraints, ζ is the drag coefficient, $\boldsymbol{q} = [\cos\theta, \sin\theta]$ is the unit vector describing particle orientation in 2D, $D_R = 1/\tau_R$ is the rotational diffusion coefficient, and ($\boldsymbol{\eta}_i$, ξ_i) are random variables

obeying the zero mean and variance consistent with the fluctuation-dissipation theorem. We used a timestep of $\Delta t = 0.001$ seconds, and set the thermal diffusivity to match our experiments at $D_T = 0.1$ μm^2/s. The drag coefficient and the energy scale of the potential were chosen such that force induced velocity at contact is $\frac{24\varepsilon}{\zeta\sigma_{avg}} = 0.6$ μm/s, which is similar in magnitude as the self-propelled velocity U_0. The WCA force is given by

$$\boldsymbol{F}_{wca} = -\nabla V_{wca} \tag{3.5a}$$

$$V_{wca}(r_{ij}) = 4\varepsilon\left[\left(\frac{\sigma}{r_{ij}}\right)^{12} - \left(\frac{\sigma}{r_{ij}}\right)^{6}\right] + \varepsilon,\ r \leq 2^{1/6}\sigma. \tag{3.5b}$$

The particle diameters σ_{ABP} and σ_{obs} were preset to 4 μm and 6.5 μm for Fig. 3.2, and for Fig. 3.5 they were chosen to be small compared to the radius of the disk shown in Fig. 3.5B, $\sigma/R = 1/20$. We used periodic boundary conditions to simulate a continuous domain. Simulations are visualized using OVITO [83].

3.3 Results

To obtain a mechanistic understanding of boundary layer accumulation and slowdown of active matter in heterogeneous materials, we combined Janus particle experiments, Brownian dynamics (BD) simulations, and analytical theory. In our experiments, we immobilized 6.5 μm lipid bilayer-coated silica particles in a random distribution at the bottom of an imaging chamber at $\phi \approx 12\%$ area fraction. We added a dilute concentration of 4 μm silica Janus particles, coated on one side with a thin layer of platinum and the other side with a lipid bilayer containing fluorescently-labeled lipids (see Materials and Methods). The silica beads sedimented to the bottom of the imaging chamber, so our experiments are conducted in 2D. The lipid bilayers on the obstacles and Janus half-coating contain different fluorescent dyes, which enabled us to track both types of particles simultaneously in different fluorescence channels. Upon adding 2% hydrogen peroxide in

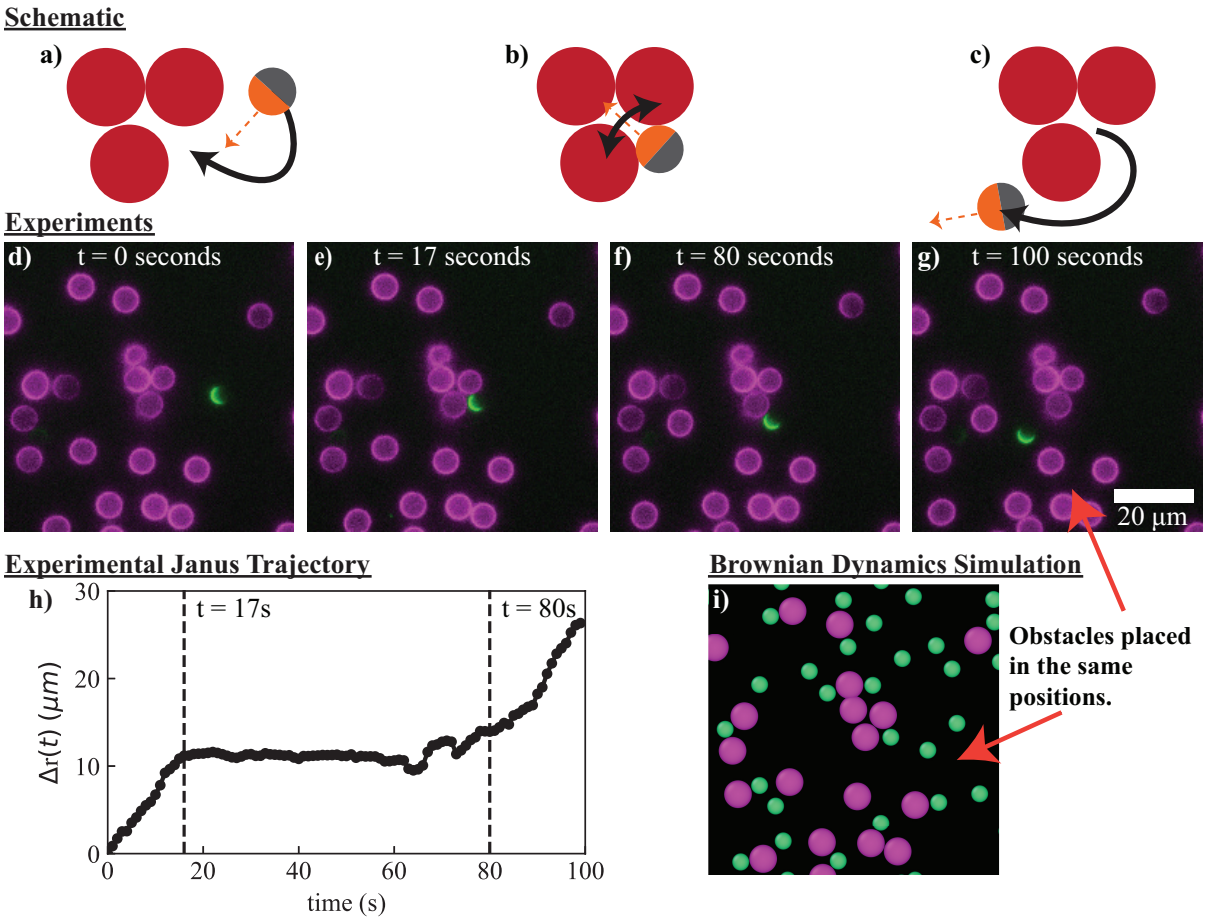

Figure 3.1: **Active particles experience a significant slowdown near obstacle boundaries and a reduction in effective diffusivity in a random array of fixed obstacles.** **(A-C)**: Schematic demonstrating the obstructed motion of an active particle near a grouping of 3 obstacles. **(D-G)**: Experimental images of a 4 µm Janus particle (green semicircle) moving through 6.5 µm obstacle particles (magenta). **(H)** Displacement of the active Janus particle (green semicircle) tracked for 100 seconds. **(I)** Brownian Dynamics (BD) simulation snapshot of active Brownian particles moving through a recreated copy of the same porous media as in the experiments. More individual particle trajectories are available in the Supplementary Information of [1](SI Fig. 1).

Milli-Q water, the Janus particles self-propelled [84–86] with speed $U_0 = 0.84 \pm 0.01$ µm/s and reorientation time $\tau_R = 14 \pm 2$ s. The self-propulsive speed and the reorientation time were determined via the mean instantaneous velocity and a fit to the known mean squared displacement (see Eq. 3.1 and Eq. 3.2 in Materials and Methods). We conducted

time lapse imaging and tracked the positions of the obstacles and the Janus particles using a tracking algorithm [73]. In Fig. 3.1, we show the motion of a single Janus particle moving through a random array of obstacles, punctuated by an obstructed motion of over 1 min in a local grouping of obstacles creating a concave boundary. Eventually, the Janus particle reoriented, propelled away from the concave boundary, and resumed an active random walk (Fig. 3.1H).

To corroborate our experiments, we developed BD simulations in which the motion of ABPs are evolved following the overdamped Langevin equation (see Materials and Methods). We compare the experimental mean squared displacement (MSD) with simulated active Brownian particle MSD to determine if this simple model quantitatively captures the transport behavior observed in the Janus particle experiments in Fig. 3.2. Comparing the two MSDs also allowed us to determine that the entropic effect of immobile obstacles was the cause of the diffusivity reduction, and not some unaccounted for mechanism (e.g. hydrodynamic forces or interparticle attractions). To simulate a dilute system, the active Brownian particles interact with obstacle particles via a purely repulsive potential, but do not interact with each other ("ideal gas" particles). We chose the active particle swimming speed and reorientation time to match our Janus particles, and we placed obstacles of the same size in the same positions as the experiments. By using the experimental obstacle particle positions as inputs into our simulations, we recapitulated our precise experimental system in the simulations (Fig. 3.1I). Consistent with our experimental observations, we also observed a similar accumulation of particles in local groupings of obstacles that form a concave boundary.

To quantify the effect of active particle accumulation and slowdown near boundaries, we computed the mean squared displacement (MSD) of the active particles in our experiments and BD simulations, $\mathrm{MSD}(t) = \langle |\boldsymbol{r}(t) - \boldsymbol{r}(0)|^2 \rangle$, where $\boldsymbol{r}(t)$ is the position of the active particle at time t. We obtained the slope of the MSD at large times to find

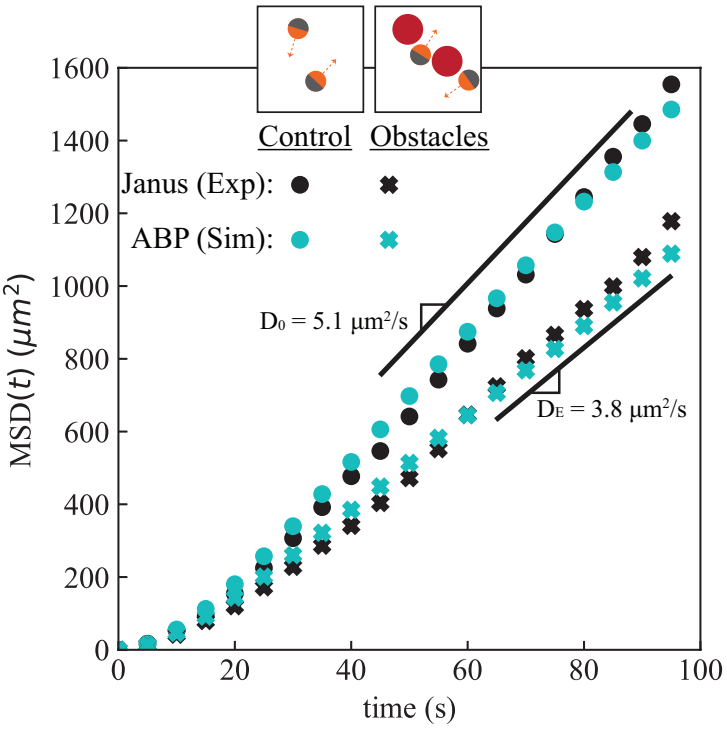

Figure 3.2: **The effective diffusivity of active particles decreased by** 25% **in a random array of fixed obstacles at** $\phi_A \approx 12\%$ **area fraction.** The mean squared displacement (MSD) of 4 μm active Janus colloids in experiments (black symbols) agrees with that in our BD simulation of the equivalent system using the active Brownian particle (ABP) model (cyan symbols), for both the control case without obstacles (circles) and with a random distribution of 6.5 μm obstacles (cross marks). Labelled diffusivities correspond to the fit to the slope at times past 50 seconds in the experiments. Standard error of the mean for the MSDs is available in the Supplementary Information of [1] (SI Fig. 2). Additional MSD simulation data for different ABP activities is available in SI Fig. 3.

the long-time self diffusivity of the active particles in the experiments and simulations, $D = \lim_{t\to\infty}(1/4)\,(\mathrm{dMSD}/\mathrm{d}t)$. As shown in Fig. 3.2, we found that the effective diffusivity of active Janus particles decreases by 25 % in the presence of fixed obstacles, from $D_0 = 5.1 \pm 0.2$ μm^2/s (without obstacles) to $D_E = 3.8 \pm 0.2$ μm^2/s (with obstacles). An ABP in a dilute suspension in two dimensions has a self diffusivity of $D_0 = D_T + U_0^2\tau_R/2$ without any obstacles present. Our BD simulations agreed quantitatively with the ex-

perimental values when we used identical activity parameters with obstacles placed in the same positions, confirming that our active Brownian particle simulations are a proficient model of the experiments. For passive Brownian particles in a dilute packing of rigid obstacles, the effective diffusivity reduces to $D_T(1-\phi)$ where D_T is the thermal Brownian diffusivity of an isolated particle [23]. Therefore, our 25% reduction in the effective diffusivity for active particles is about twice as large as the relative reduction experienced by passive Brownian particles at the same obstacle packing fraction, 12%.

In our experiments, we noticed that several 6.5 µm obstacle particles formed local groupings with narrow constrictions (Fig. 3.3A), even at semi-dilute packing fractions ($\phi \approx 12\%$). Indeed, we quantified the crowding by finding the number of other obstacle neighbors located within a surface-to-surface distance of 4 µm (Fig. 3.3B). We observed that the Janus particles spent significantly more time in the concave region of these emergent shapes as opposed to the convex side (Fig. 3.3C). We therefore hypothesized that the presence of these structures with curved geometries plays an important role in reducing the effective transport properties of active particles beyond the $1-\phi$ correction observed in passive particles. Furthermore, we anticipated that the role of obstacle geometry on the effective diffusivity is much larger for active particles undergoing persistent self-propulsion compared to passive particles translating due to thermal Brownian motion.

To test our hypothesis and to develop a micromechanical understanding of the role of obstacle geometry on active particle diffusion, we analyzed the distribution of active particles near obstacle boundaries, $P(x, y, \theta, t)$, which satisfies the Smoluchowski equation

$$\frac{\partial P}{\partial t} + \nabla \cdot (U_0 \boldsymbol{q} P - D_T \nabla P) - D_R \frac{\partial^2 P}{\partial \theta^2} = 0, \tag{3.6}$$

where U_0 is the self-propulsive speed of the active particles, $\boldsymbol{q} = [\cos(\theta), \sin(\theta)]$ is the unit orientation vector indicating the direction of self-propulsion, and D_T and $D_R = 1/\tau_R$

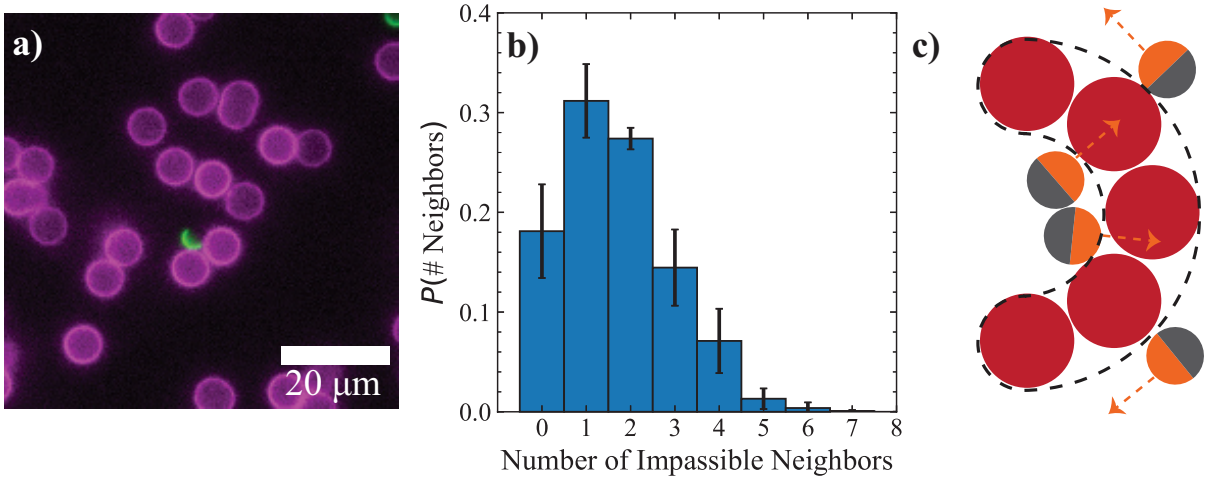

Figure 3.3: **Active Janus particles spent a significant amount of time near obstacle clusters that formed curved boundaries with narrow constriction sites.** **(A)** Image of an active Janus particle interacting with a grouping of obstacles that form a curved boundary with concavity. **(B)** Histogram quantifying obstacle particle grouping. Number of impassible neighbors is found by counting all the obstacle neighbors within distance 4 μm from a reference obstacle's surface. Groups of obstacles within this distance are impassible by a Janus swimmer with diameter 4 μm. Error bars are the standard deviation from 6 independent experiments. **(C)** Schematic demonstrating the concave shape formed by the packing of obstacles.

are the translational and rotational diffusivity, respectively. Equation 3.6 is subject to the no-flux boundary condition along the obstacle surface, $\hat{\boldsymbol{n}} \cdot [U_0 \boldsymbol{q} P - D_T \nabla P] = 0$, and periodic boundary conditions across the unit cell. The probability distribution is normalized, $\iiint P \, dxdyd\theta = 1$. We computed the density and polar order fields of active particles at steady state ($\partial P/\partial t = 0$) by solving Eq. 3.6 using the finite element method via the software *Freefem++* [87].

We obtained steady-state density and polar order fields by taking orientational integrals over the full probability distribution,

$$n(x,y) = \int_0^{2\pi} P(x,y,\theta) \, \mathrm{d}\theta, \tag{3.7a}$$

$$\boldsymbol{m}(x,y) = \int_0^{2\pi} P(x,y,\theta)\boldsymbol{q}(\theta) \, \mathrm{d}\theta, \tag{3.7b}$$

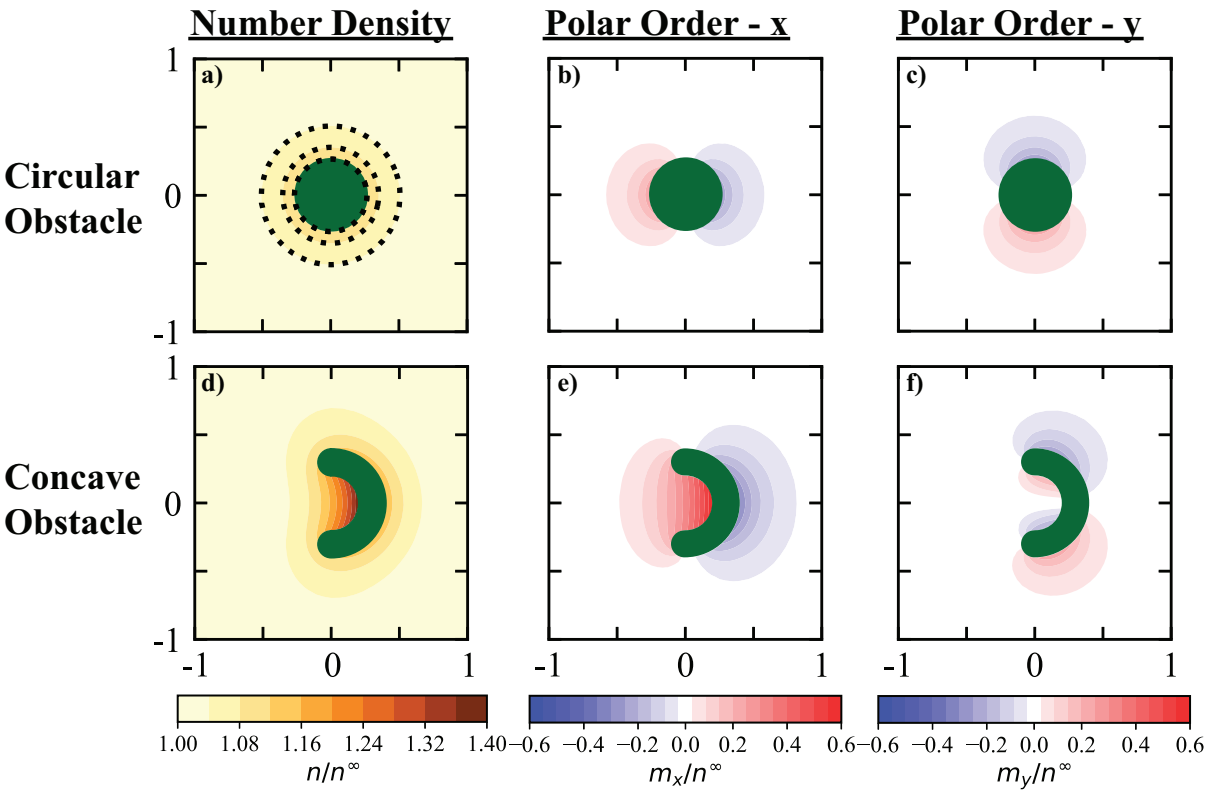

Figure 3.4: **Active constituents accumulate along boundaries due to their persistent self-motion, with a significant increase in density and polar order along curved boundaries with large concavity. (A-C)**: Density and polarization fields around a circular obstacle (radius over run length $R/(U_0\tau_R) = \sqrt{7}/4$) with dashed lines to guide the eye around the faint increase in contours. The fields are normalized by n^∞, the bulk concentration of active particles far away from the boundary. **(D-F)**: the concentration and polarization fields around a curved obstacle with large concavity ($R_{\text{inner}}/(U_0\tau_R) = 1/2$, $R_{\text{outer}}/(U_0\tau_R) = 1$). A convex, circular obstacle experiences a 12% increase in active particle accumulation, while a concave shape in the same active bath experiences a 40% increase in active particle accumulation at the inner side, indicating that the specific arrangement and shape of obstacles play a key role in the effective diffusivity of active particles. We used the same obstacle area fraction of $\approx 5.5\%$ and activity $U_0\tau_R/\delta = 1$ in both cases, where $\delta = \sqrt{D_T\tau_R}$ is the microscopic length.

We numerically solved the full Smoluchowski equation for a point-sized active particle around fixed obstacles with different shapes. For a circular obstacle, we observed a small accumulation of active particles near the surface, as shown in Fig. 3.4A. In contrast, for a curved obstacle, we observed a significant increase in the number density $n(x, y)$ and polar

order vector $\boldsymbol{m}(x, y)$ near the obstacle surface, especially at regions of large concavity (Fig. 3.4D-F). Our results in Fig. 3.4 are presented for a mild activity of $U_0\tau_R/\delta = 1$ to ensure numerical stability, where $\delta = \sqrt{D_T\tau_R}$ is the microscopic length describing how far the active particle thermally diffuses before it reorients. Even for mild activity, we observed a 40% increase in density accumulation along the inner surface compared to only 12% near the circular obstacle. The active Janus particles in our experiments have an activity of $U_0\tau_R/\delta = 100$, which would cause an even larger increase in the density and polar order enhancement at concave boundaries. Our Smoluchowski analysis suggests that the obstacle arrangement and shape play a critical role in governing local trapping of active particles in porous media.

Motivated by our micromechanical understanding of active particles near curved obstacles (Fig. 3.4), we hypothesized that the effective diffusivity of active particles in an array of obstacles should depend on the specific shape of the obstacles. To these ends, we conducted BD simulations of active Brownian particles moving through a square lattice of obstacles, carefully varying the curvature while preserving the packing fraction to keep the excluded volume constant within a unit cell. As a model obstacle shape with smoothly-varying curvature, we utilized the "Cassini Oval" (Fig. 3.5B-D), which is described by the equation

$$\left[(x+a)^2 + y^2\right]\left[(x-a)^2 + y^2\right] = b^4, \tag{3.8a}$$

$$A = 2b^2 E\left(\frac{a^4}{b^4}\right), \tag{3.8b}$$

$$\kappa^* = \frac{1}{b}\left(\frac{2a^2/b^2 - 1}{\sqrt{1 - a^2/b^2}}\right) \tag{3.8c}$$

where a and b are two shape parameters ($a < b$), κ^* is the maximum curvature in the shape, A is the shape area, and $E(x)$ is the complete elliptic integral of the second kind. The Cassini Oval is a modification of the traditional ellipse with the product of the dis-

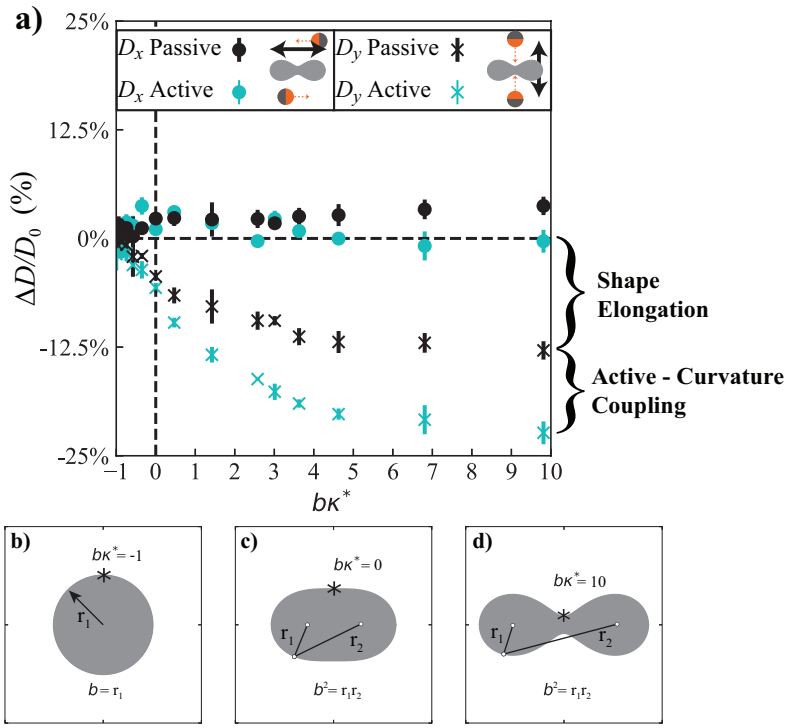

Figure 3.5: **Curved obstacles with a large concavity generate a significant slowdown in diffusive transport of active particles compared to purely convex shapes at the same packing fraction.** **(A)** Scaled diffusivity deviation as a function of shape concavity for the Cassini Oval shape described by Eq. 3.8, where $b\kappa^*$ is the non-dimensional curvature at the top of the inclusion. The diffusivity along the direction facing the concavity, D_y, decreases by 24% for the active particles for highly concave obstacles compared to 12.5% for the passive Brownian particles, indicating that the coupling between the active force and curvature plays a key role. Total packing fraction is fixed at $\phi \approx 5.5\%$, and error bars are the standard deviation of three independent trials. **(B-D)**: Schematics of area preserving Cassini Ovals for three different parameter sets. The two foci are separated a distance of $2a$. Beyond a critical distance, $a = b/\sqrt{2}$, the shape becomes concave.

tance to two foci (located at $x = \pm a$) kept constant at b^2. The shape extends laterally and shrinks vertically as it is deformed at constant area, which would generate anisotropies and slowdowns in the effective diffusivity for even passive Brownian particles. Since we wish to isolate the effects of curvature, and not the artifacts from lateral elongation of the shape, we performed BD simulations on both passive and active Brownian particles to

quantify the effects of curvature and shape elongation. Passive Brownian particles with purely excluded-volume interactions do not accumulate along boundaries, so any change in their diffusivity is due to shape elongation within the unit cell. We have conducted BD simulations at different activities and obstacle packing fractions, and found that the effective diffusivity is well-approximated by the expression $D_0(1-\phi)$ for dilute packing fractions, where D_0 is the bulk diffusivity in 2D in the absence of any obstacles. This is a proficient analytical expression for all activities at dilute obstacle densities (See SI Fig. 4 and 5 in [1]). However, at larger packing fractions of obstacles (greater than $\approx 5\%$), we observe deviations in this expression as a function of varying activity parameters. For example, as $(U_0\tau_R)\kappa^* > 1$, the scaled diffusivity decreases compared to the passive case, due to the reduced swim diffusivity in the boundary layer.

To isolate the diffusivity reduction due to obstacle shape, we computed a scaled diffusivity deviation given by

$$\frac{\Delta D}{D_0} = \frac{D_E - \tilde{D}}{D_0}, \tag{3.9}$$

where D_E is the effective diffusivity measured from the MSD, $D_0 = D_T + U_0^2\tau_R/2$ is the diffusivity without any obstacles, and $\tilde{D} = D_0(1-\phi)$ is a first correction to the diffusion constant due to excluded volume effects of circles in a square lattice [23]. In Fig. 3.5, we show our BD simulation results for an obstacle packing of $\phi = 0.055$. Using active particles of diameter σ, we set the activity as $U_0\tau_R/\sigma = 100$, $\delta/\sigma = 5\sqrt{2}$, and the shape area as $A/\sigma^2 = 400\pi$. As the concave curvature of the obstacle increased, we found a large reduction in the effective diffusivity along the direction facing the concavity (D_y) whereas the diffusivity along the other direction (D_x) remained approximately constant. As the local curvature of the shape increased, the conserved area moves off to the sides, slightly thinning its vertical projection and expanding its horizontal projection. The effect of obstacle shape elongation on the effective diffusivity is measured by the deviation in

the passive case (black circles and crosses in Fig. 3.5A). In the active case, there is an additional contribution that we designate as the active-curvature coupling.

As shown in our data for D_y in Fig. 3.5A, the active-curvature coupling contribution to the effective diffusivity is equally as large as the diffusivity reduction due to obstacle shape elongation. Due to their persistent self-propulsion, the active particles experience a large accumulation of density and polar order fields near boundaries with large concavity, consistent with our Smoluchowski analysis in Fig. 3.4. The magnitude of this boundary layer accumulation is a strong function of curvature and activity, and we have observed that the effect becomes more important at high activity and semi-dilute obstacle packing (see SI Fig. 4 and SI Fig. 5 in [1]). Our results validate our hypothesis that the shape and curvature of the obstacles play a critical role in governing the effective mobility of active particles in porous materials. The physical mechanism behind this phenomenon is that active matter accumulates along boundaries, especially along curved and concave surfaces, where active particles are trapped. Therefore, the specific shape and arrangement of obstacles within a porous material modulate the effective diffusivity of the active particles in a manner that is more significant compared to passive Brownian particles.

3.4 Discussion

In this chapter, we discovered that the obstacle packing fraction alone is insufficient to provide an accurate prediction of effective active particle diffusivity. The specific shape and distribution of physical obstacles plays a critical role in determining active transport. The *microscopic* details of the external boundary strongly influences the *macroscopic* observables like the long-time self diffusivity. Both in our experiments and simulations, a random packing of obstacles led to concave structures with narrow constriction sites that gave rise to a significant accumulation of active particles. We showed that the local

slowdown of active particles within the boundary layers has a direct effect on their overall mobility across the porous material. We focused on obstacle curvature and microstructure as metrics for predicting the effective diffusivity, which is complementary to other porosity metrics, like chord-length distributions [88] or tortuosity measurements [53].

Our scientific basis for focusing on the obstacle shape and curvature was inspired by the strong connection between active matter accumulation and its force generation along boundaries [33, 86, 89, 90]. For example, Burkholder and Brady derived a macrotransport based model to connect fluctuations in surface accumulation and the enhancement in diffusivity of passive spherical tracers [91]. Furthermore, the surface accumulation is highly dependent on surface curvature [29, 32, 34, 35]; the accumulation on certain parts of an asymmetric shape can lead to a pressure imbalance and net translation of anisotropic colloidal tracers [12, 92]. These studies showed that active matter can impart forces on its environment; however, in our work, we focused on how the micromechanical details of the environment, like curved boundaries, can alter the dynamical properties of the active particles. We validated that a strong coupling between surface curvature and active matter accumulation decreases the diffusivity of active particles by a much larger relative degree than the slowdown expected for equivalent passive Brownian particles.

The surface accumulation of active particles around a single obstacle with small curvature ($(U_0\tau_R), \delta \ll 1/\kappa$) is shown by Yan and Brady [34]:

$$\frac{n_{\text{surf}}}{n^\infty} = 1 + \frac{\ell^2}{2\delta^2} + \kappa\ell^2\lambda' + \mathcal{O}(\kappa\ell^2\lambda')^2, \tag{3.10}$$

where n^∞ is the bulk concentration of active particles, κ is the curvature in units of inverse obstacle length, $\ell = U_0\tau_R$ is the run length, and $\lambda' = \sqrt{(1 + \frac{1}{2}(\ell/\delta)^2}/\delta$ is the inverse screening length of the boundary layer. As the curvature goes from $\kappa = 0$ (e.g. a flat wall) to a convex curvature $\kappa < 0$ (e.g. the outside of a circle), the surface accumulation decreases proportionally. However, if regions of the shape have a concave curvature $\kappa > 1$

(e.g. the inside of a circle), the accumulation increases. To first order in curvature, the accumulation described in Eq. 3.10 predicts no net force on an asymmetric surface [34], and higher order curvature expansions are needed to get a nonzero force. The need for large curvatures is consistent with our simulations (Fig. 3.5), where we found that the active-curvature coupling effect on the diffusivity is small until the nondimensional curvature is large, $\kappa\ell \gg 1$, (see SI Fig. 4 in [1]). For our most curved obstacle in Fig. 3.5D, our analysis from Eq. 3.10 leads us to define our grouping of $\kappa\ell^2\lambda' \approx 7 \times 10^3$. The effect of active-curvature coupling is expected to increase dramatically in dense, tortuous media, leading to the mechanism of hopping and trapping transport. Other mechanisms of motility, such as the run-reverse mechanism seen in bacteria and archaea [93, 94], can enable swimmers to avoid the slowdown resulting from boundary accumulation and enhance transport between highly curved pores [65].

We focused on the effects of immobile obstacles with purely excluded volume interactions. However, soft porous materials present a rich opportunity for future study. Boundary fluctuations of soft surfaces are important for particle transport in mucus, hydrogels, and other polymeric networks [21, 95, 96]. Active particles have been shown to induce large deformations on soft membranes [97, 98], changing the curvature and transport drastically. Hydrogel networks and sediments in 3D provide an additional degree of freedom for a swimmer to avoid obstacles. In 2D, close packing of disks precludes transport; however, a close packing of spheres in 3D allows for bicontinous percolation, resulting in a reduced but nonzero diffusivity.

Our work opens up opportunities for future experimental work to control active matter diffusion via the design of obstacle shape and arrangement. Convex, nonspherical inclusions can be used to control transport and create anisotropic spreading of bacteria along a predefined axis. Novel sorting mechanisms have already been developed using asymmetric blockers [38], and the method could be extended to sort mixtures of swim-

mers with different types of motility [99]. Precise consideration of the activity-curvature coupling on transport serves as a promising route to increase the efficacy of these sorting methods, and may lead to more accurate predictions of bacterial transport coefficients.

Bibliography

[1] K. J. Modica, Y. Xi, and S. C. Takatori, *Porous media microstructure determines the diffusion of active matter: Experiments and simulations*, *Frontiers in Physics* **10** (4, 2022) 869175.

[2] J. Gannon, U. Mingelgrin, M. Alexander, and R. Wagenet, *Bacterial transport through homogeneous soil*, *Soil Biology and Biochemistry* **23** (1, 1991) 1155–1160.

[3] J. S. T. Adadevoh, S. Triolo, C. A. Ramsburg, and R. M. Ford, *Chemotaxis Increases the Residence Time of Bacteria in Granular Media Containing Distributed Contaminant Sources*, *Environmental Science & Technology* **50** (1, 2016) 181–187.

[4] B. J. Toley and N. S. Forbes, *Motility is critical for effective distribution and accumulation of bacteria in tumor tissue*, *Integrative Biology* **4** (2, 2012) 165–176.

[5] R. W. Kasinskas and N. S. Forbes, *Salmonella typhimurium specifically chemotax and proliferate in heterogeneous tumor tissue in vitro*, *Biotechnology and Bioengineering* **94** (2006), no. 4 710–721, [https://onlinelibrary.wiley.com/doi/pdf/10.1002/bit.20883].

[6] D. Ribet and P. Cossart, *How bacterial pathogens colonize their hosts and invade deeper tissues*, *Microbes and Infection* **17** (2015), no. 3 173–183.

[7] S. X. Gu and S. R. Lentz, *Fibrin films: overlooked hemostatic barriers against microbial infiltration*, *Journal of Clinical Investigation* **128** (8, 2018) 3243–3245.

[8] C. Y. Kao, W. H. Lin, C. C. Tseng, A. B. Wu, M. C. Wang, and J. J. Wu, *The complex interplay among bacterial motility and virulence factors in different Escherichia coli infections*, *European Journal of Clinical Microbiology & Infectious Diseases* **33** (12, 2014) 2157–2162.

[9] A. Martínez-Calvo, C. Trenado-Yuste, and S. S. Datta, *Active Transport in Complex Environments*, in *Out-of-equilibrium Soft Matter*. The Royal Society of Chemistry, 03, 2023.

[10] B. Chaban, H. V. Hughes, and M. Beeby, *The flagellum in bacterial pathogens: For motility and a whole lot more*, *Seminars in Cell & Developmental Biology* **46** (2015) 91–103. Biomineralisation & Motorisation of pathogens.

[11] D. Woolley, *Motility of spermatozoa at surfaces*, *Reproduction* (8, 2003) 259–270.

[12] C. Bechinger, R. Di Leonardo, H. Löwen, C. Reichhardt, G. Volpe, and G. Volpe, *Active Particles in Complex and Crowded Environments*, *Reviews of Modern Physics* **88** (11, 2016) 045006.

[13] R. Golestanian, T. B. Liverpool, and A. Ajdari, *Propulsion of a Molecular Machine by Asymmetric Distribution of Reaction Products*, *Physical Review Letters* **94** (6, 2005) 220801.

[14] J. R. Howse, R. A. L. Jones, A. J. Ryan, T. Gough, R. Vafabakhsh, and R. Golestanian, *Self-Motile Colloidal Particles: From Directed Propulsion to Random Walk*, *Physical Review Letters* **99** (7, 2007) 048102.

[15] S. Sanchez, A. N. Ananth, V. M. Fomin, M. Viehrig, and O. G. Schmidt, *Superfast Motion of Catalytic Microjet Engines at Physiological Temperature*, *Journal of the American Chemical Society* **133** (9, 2011) 14860–14863.

[16] R. Soto and R. Golestanian, *Self-Assembly of Catalytically Active Colloidal Molecules: Tailoring Activity Through Surface Chemistry*, *Physical Review Letters* **112** (2, 2014) 068301.

[17] X. Ma, A. Jannasch, U.-R. Albrecht, K. Hahn, A. Miguel-López, E. Schäffer, and S. Sánchez, *Enzyme-Powered Hollow Mesoporous Janus Nanomotors*, *Nano Letters* **15** (10, 2015) 7043–7050.

[18] X. Ma, K. Hahn, and S. Sanchez, *Catalytic Mesoporous Janus Nanomotors for Active Cargo Delivery*, *Journal of the American Chemical Society* **137** (4, 2015) 4976–4979.

[19] R. Dreyfus, J. Baudry, M. L. Roper, M. Fermigier, H. A. Stone, and J. Bibette, *Microscopic artificial swimmers*, *Nature* **437** (10, 2005) 862–865.

[20] A. Bricard, J.-B. Caussin, D. Das, C. Savoie, V. Chikkadi, K. Shitara, O. Chepizhko, F. Peruani, D. Saintillan, and D. Bartolo, *Emergent vortices in populations of colloidal rollers*, *Nature Communications* **6** (11, 2015) 7470.

[21] L.-H. Cai, S. Panyukov, and M. Rubinstein, *Hopping Diffusion of Nanoparticles in Polymer Matrices*, *Macromolecules* **48** (2, 2015) 847–862.

[22] J. Witten and K. Ribbeck, *The particle in the spider's web: transport through biological hydrogels*, *Nanoscale* **9** (2017), no. 24 8080–8095.

[23] M. Mangeat, T. Guérin, and D. S. Dean, *Effective diffusivity of Brownian particles*

in a two dimensional square lattice of hard disks, *The Journal of Chemical Physics* **152** (6, 2020) 234109.

[24] M. Saxton, *Anomalous diffusion due to obstacles: a Monte Carlo study*, *Biophysical Journal* **66** (2, 1994) 394–401.

[25] R. Alonso-Matilla, B. Chakrabarti, and D. Saintillan, *Transport and dispersion of active particles in periodic porous media*, *Physical Review Fluids* **4** (4, 2019) 043101, [arXiv:1809.0008].

[26] G. Volpe, S. Gigan, and G. Volpe, *Simulation of the active brownian motion of a microswimmer*, *American Journal of Physics* **82** (2014), no. 7 659–664.

[27] A. Wysocki, J. Elgeti, and G. Gompper, *Giant adsorption of microswimmers: Duality of shape asymmetry and wall curvature*, *Phys. Rev. E* **91** (5, 2015) 050302.

[28] J. Elgeti and G. Gompper, *Self-propelled rods near surfaces*, *EPL (Europhysics Letters)* **85** (2, 2009) 38002.

[29] J. Elgeti and G. Gompper, *Wall accumulation of self-propelled spheres*, *EPL (Europhysics Letters)* **101** (2, 2013) 48003.

[30] J. Elgeti, R. G. Winkler, and G. Gompper, *Physics of microswimmers—single particle motion and collective behavior: a review*, *Reports on Progress in Physics* **78** (5, 2015) 056601.

[31] H. H. Wensink and H. Löwen, *Aggregation of self-propelled colloidal rods near confining walls*, *Phys. Rev. E* **78** (9, 2008) 031409.

[32] M. Wang, *Effect of boundaries on noninteracting weakly active particles in different geometries*, *Phys. Rev. E* **103** (4, 2021) 042609.

[33] W. Yan and J. F. Brady, *The force on a boundary in active matter*, *Journal of Fluid Mechanics* **785** (12, 2015) R1, [arXiv:1510.0773].

[34] W. Yan and J. F. Brady, *The curved kinetic boundary layer of active matter*, *Soft Matter* **14** (2018), no. 2 279–290, [arXiv:1711.0145].

[35] F. Smallenburg and H. Löwen, *Swim pressure on walls with curves and corners*, *Phys. Rev. E* **92** (9, 2015) 032304.

[36] S. C. Takatori, W. Yan, and J. F. Brady, *Swim pressure: Stress generation in active matter*, *Phys. Rev. Lett.* **113** (7, 2014) 028103.

[37] A. P. Berke, L. Turner, H. C. Berg, and E. Lauga, *Hydrodynamic attraction of swimming microorganisms by surfaces*, *Phys. Rev. Lett.* **101** (7, 2008) 038102.

[38] R. Martinez, F. Alarcon, J. L. Aragones, and C. Valeriani, *Trapping flocking particles with asymmetric obstacles*, *Soft Matter* **16** (2020) 4739–4745.

[39] D. Giacché, T. Ishikawa, and T. Yamaguchi, *Hydrodynamic entrapment of bacteria swimming near a solid surface*, *Phys. Rev. E* **82** (11, 2010) 056309.

[40] P. Galajda, J. Keymer, P. Chaikin, and R. Austin, *A Wall of Funnels Concentrates Swimming Bacteria*, *Journal of Bacteriology* **189** (12, 2007) 8704–8707.

[41] M. Molaei, M. Barry, R. Stocker, and J. Sheng, *Failed escape: Solid surfaces prevent tumbling of escherichia coli*, *Phys. Rev. Lett.* **113** (8, 2014) 068103.

[42] J. Kalnin, E. Kotomin, and J. Maier, *Calculations of the effective diffusion coefficient for inhomogeneous media*, *Journal of Physics and Chemistry of Solids* **63** (3, 2002) 449–456.

[43] G. Li and J. X. Tang, *Accumulation of microswimmers near a surface mediated by collision and rotational brownian motion*, *Phys. Rev. Lett.* **103** (8, 2009) 078101.

[44] O. Sipos, K. Nagy, R. Di Leonardo, and P. Galajda, *Hydrodynamic trapping of swimming bacteria by convex walls*, *Phys. Rev. Lett.* **114** (6, 2015) 258104.

[45] S. Das, A. Garg, A. I. Campbell, J. Howse, A. Sen, D. Velegol, R. Golestanian, and S. J. Ebbens, *Boundaries can steer active Janus spheres*, *Nature Communications* **6** (12, 2015) 8999.

[46] D. Takagi, J. Palacci, A. B. Braunschweig, M. J. Shelley, and J. Zhang, *Hydrodynamic capture of microswimmers into sphere-bound orbits*, *Soft Matter* **10** (2014) 1784–1789.

[47] A. Morin, D. Lopes Cardozo, V. Chikkadi, and D. Bartolo, *Diffusion, subdiffusion, and localization of active colloids in random post lattices*, *Physical Review E* **96** (10, 2017) 042611.

[48] S. Das, G. Gompper, and R. G. Winkler, *Confined active Brownian particles: theoretical description of propulsion-induced accumulation*, *New Journal of Physics* **20** (1, 2018) 015001.

[49] C. M. Kjeldbjerg and J. F. Brady, *Theory for the casimir effect and the partitioning of active matter*, *Soft Matter* **17** (2021) 523–530.

[50] G. Volpe, I. Buttinoni, D. Vogt, H.-J. Kümmerer, and C. Bechinger, *Microswimmers in patterned environments*, *Soft Matter* **7** (2011) 8810–8815.

[51] D. Reguera and J. M. Rubí, *Kinetic equations for diffusion in the presence of entropic barriers*, *Physical Review E* **64** (11, 2001) 061106.

[52] H. Brenner and D. A. Edwards, *Macrotransport Processes*. Elsevier, 1993.

[53] L. Shen and Z. Chen, *Critical review of the impact of tortuosity on diffusion*, *Chemical Engineering Science* **62** (7, 2007) 3748–3755.

[54] P. S. Burada, P. Hänggi, F. Marchesoni, G. Schmid, and P. Talkner, *Diffusion in Confined Geometries*, *ChemPhysChem* **10** (1, 2009) 45–54, [arXiv:0808.2345].

[55] L. Ning, P. Liu, F. Ye, M. Yang, and K. Chen, *Diffusion of colloidal particles in model porous media*, *Physical Review E* **103** (2, 2021) 022608.

[56] L. J. Perez, T. Bhattacharjee, S. S. Datta, R. Parashar, and N. L. Sund, *Impact of confined geometries on hopping and trapping of motile bacteria in porous media*, *Physical Review E* **103** (1, 2021) 012611.

[57] T. Bhattacharjee and S. S. Datta, *Bacterial hopping and trapping in porous media*, *Nature Communications* **10** (12, 2019) 2075.

[58] N. Figueroa-Morales, L. Dominguez-Rubio, T. L. Ott, and I. S. Aranson, *Mechanical shear controls bacterial penetration in mucus*, *Scientific Reports* **9** (12, 2019) 9713.

[59] V. K. Truong, D. E. Mainwaring, P. Murugaraj, D. H. K. Nguyen, and E. P. Ivanova, *Impact of confining 3-D polymer networks on dynamics of bacterial ingress and self-organisation*, *Journal of Materials Chemistry B* **3** (2015), no. 44 8704–8710.

[60] R. Bansil, J. P. Celli, J. M. Hardcastle, and B. S. Turner, *The Influence of Mucus Microstructure and Rheology in Helicobacter pylori Infection*, *Frontiers in Immunology* **4** (2013) 310.

[61] H. Wu, B. Greydanus, and D. K. Schwartz, *Mechanisms of transport enhancement for self-propelled nanoswimmers in a porous matrix*, *Proceedings of the National Academy of Sciences* **118** (2021), no. 27 e210180711, [https://www.pnas.org/content/118/27/e2101807118.full.pdf].

[62] N. A. Licata, B. Mohari, C. Fuqua, and S. Setayeshgar, *Diffusion of Bacterial Cells in Porous Media*, *Biophysical Journal* **110** (1, 2016) 247–257.

[63] M. Brun-Cosme-Bruny, E. Bertin, B. Coasne, P. Peyla, and S. Rafaï, *Effective diffusivity of microswimmers in a crowded environment*, *The Journal of Chemical Physics* **150** (3, 2019) 104901.

[64] M. Sandoval and L. Dagdug, *Effective diffusion of confined active Brownian swimmers*, *Physical Review E - Statistical, Nonlinear, and Soft Matter Physics* **90** (12, 2014) 062711.

[65] C. Kurzthaler, S. Mandal, T. Bhattacharjee, H. Löwen, S. S. Datta, and H. A. Stone, *A geometric criterion for the optimal spreading of active polymers in porous media*, *Nature Communications* **12** (12, 2021) 7088.

[66] O. Chepizhko and F. Peruani, *Diffusion, Subdiffusion, and Trapping of Active Particles in Heterogeneous Media*, *Physical Review Letters* **111** (10, 2013) 160604, [arXiv:1310.0830].

[67] C. Reichhardt and C. J. Olson Reichhardt, *Active matter transport and jamming on disordered landscapes*, *Phys. Rev. E* **90** (7, 2014) 012701.

[68] C. J. O. Reichhardt and C. Reichhardt, *Avalanche dynamics for active matter in heterogeneous media*, *New Journal of Physics* **20** (2, 2018) 025002.

[69] T. Jakuszeit, O. A. Croze, and S. Bell, *Diffusion of active particles in a complex environment: Role of surface scattering*, *Phys. Rev. E* **99** (1, 2019) 012610.

[70] A. Chamolly, T. Ishikawa, and E. Lauga, *Active particles in periodic lattices*, *New Journal of Physics* **19** (11, 2017) 115001.

[71] G. Volpe and G. Volpe, *The topography of the environment alters the optimal search strategy for active particles*, *Proceedings of the National Academy of Sciences* **114** (2017), no. 43 11350–11355, [https://www.pnas.org/content/114/43/11350.full.pdf].

[72] C. Yuan, A. Chen, B. Zhang, and N. Zhao, *Activity–crowding coupling effect on the diffusion dynamics of a self-propelled particle in polymer solutions*, *Physical Chemistry Chemical Physics* **21** (11, 2019) 24112–24125.

[73] J. C. Crocker and D. G. Grier, *Methods of digital video microscopy for colloidal studies*, *Journal of Colloid and Interface Science* **179** (1996), no. 1 298–310.

[74] W. Sutherland, *Lxxv. a dynamical theory of diffusion for non-electrolytes and the molecular mass of albumin*, *The London, Edinburgh, and Dublin Philosophical Magazine and Journal of Science* **9** (1905), no. 54 781–785, [https://doi.org/10.1080/14786440509463331].

[75] M. von Smoluchowski, *Zur kinetischen theorie der brownschen molekularbewegung und der suspensionen*, *Annalen der Physik* **326** (1906), no. 14 756–780, [https://onlinelibrary.wiley.com/doi/pdf/10.1002/andp.19063261405].

[76] A. Einstein, *Eine neue bestimmung der moleküldimensionen*, *Annalen der Physik* **324** (1906), no. 2 289–306, [https://onlinelibrary.wiley.com/doi/pdf/10.1002/andp.19063240204].

[77] J. A. Anderson, J. Glaser, and S. C. Glotzer, *HOOMD-blue: A Python package for high-performance molecular dynamics and hard particle Monte Carlo simulations*, *Computational Materials Science* **173** (2, 2020) 109363.

[78] S. C. Takatori and J. F. Brady, *Forces, stresses and the (thermo?) dynamics of active matter*, *Current Opinion in Colloid & Interface Science* **21** (2, 2016) 24–33.

[79] M. R. Shaebani, A. Wysocki, R. G. Winkler, G. Gompper, and H. Rieger, *Computational models for active matter*, *Nature Reviews Physics* **2** (4, 2020) 181–199.

[80] M. C. Marchetti, J. F. Joanny, S. Ramaswamy, T. B. Liverpool, J. Prost, M. Rao, and R. A. Simha, *Hydrodynamics of soft active matter*, *Reviews of Modern Physics* **85** (7, 2013) 1143–1189.

[81] A. P. Solon, M. E. Cates, and J. Tailleur, *Active brownian particles and run-and-tumble particles: A comparative study*, *The European Physical Journal Special Topics* **224** (7, 2015) 1231–1262.

[82] J. D. Weeks, D. Chandler, and H. C. Andersen, *Role of Repulsive Forces in Determining the Equilibrium Structure of Simple Liquids*, *The Journal of Chemical Physics* **54** (6, 1971) 5237–5247.

[83] A. Stukowski, *Visualization and analysis of atomistic simulation data with OVITO–the open visualization tool*, *Modelling and Simulation in Materials Science and Engineering* **18** (12, 2009) 015012.

[84] W. F. Paxton, K. C. Kistler, C. C. Olmeda, A. Sen, S. K. St. Angelo, Y. Cao, T. E. Mallouk, P. E. Lammert, and V. H. Crespi, *Catalytic nanomotors: Autonomous*

movement of striped nanorods, *Journal of the American Chemical Society* **126** (2004), no. 41 13424–13431, [https://doi.org/10.1021/ja047697z]. PMID: 15479099.

[85] J. R. Howse, R. A. L. Jones, A. J. Ryan, T. Gough, R. Vafabakhsh, and R. Golestanian, *Self-motile colloidal particles: From directed propulsion to random walk*, *Phys. Rev. Lett.* **99** (7, 2007) 048102.

[86] S. C. Takatori, R. De Dier, J. Vermant, and J. F. Brady, *Acoustic trapping of active matter*, *Nature communications* **7** (2016), no. 1 1–7.

[87] F. Hecht, *New development in freefem++*, *Journal of Numerical Mathematics* **20** (1, 2012) 251–266.

[88] S. Torquato and B. Lu, *Chord-length distribution function for two-phase random media*, *Phys. Rev. E* **47** (4, 1993) 2950–2953.

[89] S. C. Takatori and J. F. Brady, *Swim stress, motion, and deformation of active matter: effect of an external field*, *Soft Matter* **10** (2014), no. 47 9433–9445.

[90] A. K. Omar, Z.-G. Wang, and J. F. Brady, *Microscopic origins of the swim pressure and the anomalous surface tension of active matter*, *Physical Review E* **101** (1, 2020) 012604.

[91] E. W. Burkholder and J. F. Brady, *Tracer diffusion in active suspensions*, *Physical Review E* **95** (5, 2017) 052605.

[92] A. Kaiser, A. Peshkov, A. Sokolov, B. ten Hagen, H. Löwen, and I. S. Aranson, *Transport powered by bacterial turbulence*, *Phys. Rev. Lett.* **112** (4, 2014) 158101.

[93] K. Son, J. S. Guasto, and R. Stocker, *Bacteria can exploit a flagellar buckling instability to change direction*, *Nature Physics* **9** (8, 2013) 494–498.

[94] K. L. Thornton, J. K. Butler, S. J. Davis, B. K. Baxter, and L. G. Wilson, *Haloarchaea swim slowly for optimal chemotactic efficiency in low nutrient environments*, *Nature Communications* **11** (12, 2020) 4453.

[95] I. V. Bodrenko, S. Salis, S. Acosta-Gutierrez, and M. Ceccarelli, *Diffusion of large particles through small pores: From entropic to enthalpic transport*, *The Journal of Chemical Physics* **150** (6, 2019) 211102.

[96] R. Ledesma-Aguilar and J. M. Yeomans, *Enhanced Motility of a Microswimmer in Rigid and Elastic Confinement*, *Physical Review Letters* **111** (9, 2013) 138101, [arXiv:1303.7325].

[97] S. C. Takatori and A. Sahu, *Active contact forces drive nonequilibrium fluctuations in membrane vesicles*, *Phys. Rev. Lett.* **124** (4, 2020) 158102.

[98] H. R. Vutukuri, M. Hoore, C. Abaurrea-Velasco, L. van Buren, A. Dutto, T. Auth, D. A. Fedosov, G. Gompper, and J. Vermant, *Active particles induce large shape deformations in giant lipid vesicles*, *Nature* **586** (10, 2020) 52–56.

[99] M. Khatami, K. Wolff, O. Pohl, M. R. Ejtehadi, and H. Stark, *Active Brownian particles and run-and-tumble particles separate inside a maze*, *Scientific Reports* **6** (12, 2016) 37670.

Chapter 4

Using Soft Confinement to Enhance Transport of Self-Propelled Rods

In this chapter, we present an analytical framework for evolving the dynamics of active rods under any periodic external potential, including confining channels and arrays of harmonic traps. As a proof of concept, we analyze the structure and dispersion of self-propelled rods under a soft, periodic one-dimensional (1D) confinement potential and under a two-dimensional (2D) periodic radial harmonic trap. While passive rods and polymers nematically order under 1D confinement, their diffusive transport along the director is limited by thermal diffusion. In contrast, self-propelled rods can generate large convective fluxes when combined with nematic ordering, producing a strong dispersion along the director. Combining theory and simulation, we demonstrate that nematic alignment and self-propulsion generates an exponential enhancement in active diffusivity along the director, in contrast to passive rods that experience at most a 2-fold increase.

This chapter includes content from our previously published article:

[1] K.J. Modica and S.C. Takatori, *Soft confinement of self-propelled rods: simulation and theory*, *Soft Matter* **20** (2, 2024), no. 10 2331–2337. All authors conceived of the study and designed research; KJM performed simulations and analytical calculations; SCT supervised the study; and all authors wrote the paper.

4.1 Introduction

Active rods, characterized by their anisotropic shape and nonequilibrium motion, are a powerful model for describing the behavior of biological constituents across a range of systems, from motile bacteria to cytoskeletal filaments.[2–4] While self-propelled systems are often studied for their collective behaviors, even dilute systems of active particles can present unexpected physics. Despite significant prior work, predicting and controlling the transport and structure of active rods remains an ongoing challenge.

One method to study and control active matter is through geometric confinement.[5–12] Confinement introduces additional complexities to the dynamics of active matter, as interactions with boundaries profoundly influence the emergent properties of the system.[13–21] For active rods, the proportion of normal and parallel alignment to the confinement direction is set by the competition between activity-induced boundary accumulation (normal alignment) and entropy-mediated reorientation (parallel alignment).[22–26]

In addition to impenetrable walls, many systems exhibit a softer form of confinement where escape is made possible (if unlikely) by thermal fluctuations or active forcing. Actin and microtubule filaments placed in shallow channels are known to leave the confining channels when propelled by motor proteins, requiring specific geometries to prevent escape.[27–30] Optical and acoustic tweezers provide another mechanism of weakly confining bacteria and active particles for measuring their motility.[31–33] Despite the wide prevalence of soft confinement on self-propelled rods, the topic remains under-explored theoretically and in simulation. Existing work on anisotropic colloidal particles uses dynamical density functional theory (DDFT).[34–36] While DDFT has been used to model the mean-field interactions between particles, in the presence of an external field, the user needs to convert the local potential field acting across the mass density of the finite body into a potential energy determined by the particle's center of mass position and orientation.

In this chapter, we demonstrate a framework for studying dilute active rods in any periodic external field by converting a local potential energy density into a position and orientation dependent potential energy on the rod center of mass. We apply our framework for the special case of a 1D periodic potential to illustrate that soft confinement in channels increases the axial transport even for dilute concentrations of swimmers when the rod length is commensurate to the channel size. Lastly, inspired by optical tweezers,

we also apply our framework on a periodic array of harmonic traps to demonstrate the utility of our approach to more complex forms of soft confinement.

4.2 Modeling Active Rods

In the overdammped limit, the motion of self-propelled rods follows the Langevin equation with no inertia. The rod is treated as a rigid body that propels by an active force directed along the long axis. The active, Brownian, and external forces and torques are summed to generate translational and rotational motion. To simulate a dilute system, the self-propelled rods do not interact with each other (i.e., the rods are "ideal"). The evolution equation for the ith rod's center of mass is:

$$\frac{d\boldsymbol{r}_i}{dt} = \sqrt{2D_T}\boldsymbol{\eta}_i(t) + \frac{\boldsymbol{F}_i^{ext}}{\zeta_T} + \frac{\boldsymbol{F}_i^{act}}{\zeta_T} \tag{4.1a}$$

$$\frac{d\theta_i}{dt} = \sqrt{2D_\theta}\xi_i(t) + \frac{L_i^{ext}}{\zeta_\theta}. \tag{4.1b}$$

where ζ_T and ζ_θ are the translational and rotational drag coefficients, $\boldsymbol{F}_i^{act}$ is the swim force, $\boldsymbol{F}_i^{ext}$ is the force on the rod center of mass from the external potential, and L_i^{ext} is the torque on the rod center of mass from the external potential. The swim force $\boldsymbol{F}_i^{act} = U_0\zeta_T\boldsymbol{u}_i$ is of constant magnitude, with the direction set by the rod orientation unit vector $\boldsymbol{u}_i = \cos(\theta_i)\hat{\boldsymbol{e}}_x + \sin(\theta_i)\hat{\boldsymbol{e}}_y$ in 2D. Finally, the translational and rotational diffusion coefficients are D_T and D_θ, with $(\boldsymbol{\eta}_i,\ \xi_i)$ as random variables with zero mean and a variance consistent with the fluctuation-dissipation theorem.

As a complementary description of the Langevin equation, the probability distribution $f(\boldsymbol{r}, \theta, t)$ of a self-propelled Brownian rod at position $\boldsymbol{r}$, orientation angle θ and time t confined in 2-dimensions follows the Smoluchowski diffusion equation:

$$\frac{\partial f(\boldsymbol{r}, \theta, t)}{\partial t} + \nabla \cdot \boldsymbol{J}_T + \frac{\partial}{\partial \theta} J_\theta = 0 \tag{4.2a}$$

$$\boldsymbol{J}_T = \left[U_0 \boldsymbol{u} f - \boldsymbol{D}(\boldsymbol{u}) \cdot \left(\nabla f + f \nabla \left[\frac{V}{k_\mathrm{B} T} \right] \right) \right] \tag{4.2b}$$

$$J_\theta = -D_\theta \left(\frac{\partial}{\partial \theta} f + f \frac{\partial}{\partial \theta} \left[\frac{V}{k_\mathrm{B} T} \right] \right). \tag{4.2c}$$

The Smoluchowski equation can be derived by noise averaging the Langevin equation for the rod.[37, 38] It describes the normalized probability density f of rods moving at constant velocity U_0 due to a force acting along its center of mass and oriented along its long axis in direction $\boldsymbol{u}$. The rods undergo Brownian motion with a (potentially orientationally dependent) translational diffusion tensor $\boldsymbol{D}(\boldsymbol{u})$ and rotational diffusion constant D_θ. $k_\mathrm{B}T$ is the thermal energy, and V is the potential energy of the entire body in the presence of an external field. $\boldsymbol{J}_T$ and J_θ represent the translational and angular flux, with the translational gradient operator $\nabla = \frac{\partial}{\partial x}\hat{\boldsymbol{e}}_x + \frac{\partial}{\partial y}\hat{\boldsymbol{e}}_y$. For the purpose of this study, interactions between rods are neglected to probe the dilute limit.

When studying anisotropic particles, Eq. 4.2 is complicated by the calculation of the constituent's potential energy given a potential energy field ϕ and mass distribution ρ

$$V(\boldsymbol{r}, \theta) = \int \phi(\boldsymbol{r} - \boldsymbol{s}) \rho(\boldsymbol{s}) d\boldsymbol{s}. \tag{4.3}$$

The mass distribution ρ is zero everywhere except in the region $\boldsymbol{r} + \boldsymbol{s}$ where $\boldsymbol{r}$ is the rod center of mass, $\boldsymbol{s} = s\boldsymbol{u}$ is the displacement along the rod long axis in direction $\boldsymbol{u}$ from the rod center, with distance spanning from $s = -L_{Rod}/2$ to $s = L_{Rod}/2$ (see Supplementary Information Section I. of [1]).

To find an analytical expression for V, one would traditionally perform a multipole series expansion on ϕ. This Taylor series expansion about the rod center is slow to converge when the potential energy changes rapidly relative to the length of the rod. In fact, a multipole series of a periodic monochromatic field with wavelength λ diverges for $2\pi L_{Rod} \geq \lambda$. To overcome this challenge, we have instead chosen to expand ϕ as a Fourier series and compute the Fourier coefficients (rather than the multipole moments)

of $V(\boldsymbol{r}, \theta)$. We compute the convolution in Eq. 4.3 as a product in Fourier space:

$$\hat{V}_{nm}(\theta) = \hat{\phi}_{nm}\hat{\rho}_{nm}(\theta). \tag{4.4}$$

The Fourier transform of the line density $\hat{\rho}_{nm}$ can be derived analytically as described in Supplementary Information Section I. of [1], allowing us to determine an expression for the center of mass potential directly:

$$V(\boldsymbol{r}, \theta) = \sum_{n,m} \hat{\phi}_{nm} e^{i2\pi \boldsymbol{k}_{nm}\cdot\boldsymbol{r}} \mathrm{sinc}\left(\pi L_{Rod} \boldsymbol{k}_{nm} \cdot \boldsymbol{u}\right). \tag{4.5}$$

The wavevector is defined as $\boldsymbol{k}_{nm} = \frac{n}{L_x}\hat{\boldsymbol{e}}_x + \frac{m}{L_y}\hat{\boldsymbol{e}}_y$. This method converges rapidly for periodic potentials with a low-wavenumber power spectrum. The $\mathrm{sinc}(\pi L_{Rod}\boldsymbol{k}_{n,m} \cdot \boldsymbol{u})$ term comes from the Fourier transform of the segment density for a rod[39] and couples the orientation of the rod to the potential energy.

Although Eqs. 4.2-4.5 are true for any periodic potential, we will focus on a particular case of active rods confined in a 1D monochromatic potential field as shown in Fig. 4.1. In this field, the rod potential energy is

$$V(x, \theta) = -A\cos\left(\frac{2\pi x}{\lambda}\right)\mathrm{sinc}\left(\frac{\pi L_{Rod}\cos(\theta)}{\lambda}\right). \tag{4.6}$$

We compare the solutions to the Smoluchowski equations to discrete simulations of thin rods using Brownian dynamics (BD) simulations. The rods are composed of coarse-grained beads separated by distance σ connected by rigid body constraints. Each bead on the rigid rod feels the potential energy field ϕ, and the resultant forces and torques move the rod center of mass and rotate the body. The center of mass potential energy in this discrete system is slightly modified from the continuum limit (see Supplementary Information Section I. of [1]), but Eq. 4.5 is suitable within error for our results when $L_{Rod}/\sigma \gtrsim 10$. For the following results, we set $L_{Rod}/\sigma = 21$. As mentioned in Fig. 4.1, this study is focused on dilute systems and as such the coarse-grained beads are point

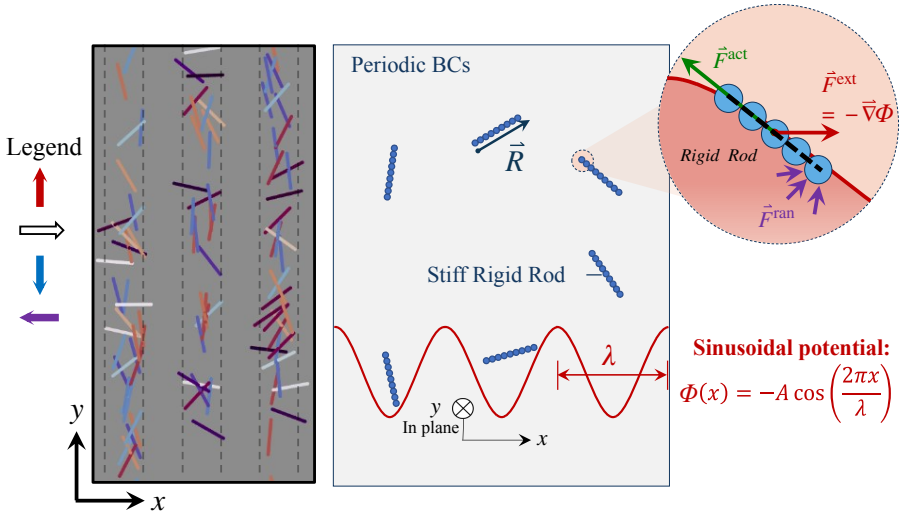

Figure 4.1: Schematic of active rods in a monochromatic potential energy field ϕ. The rods are modelled in simulation as a rigid assembly of coarse-grained beads. Left: Simulation snapshot of self-propelled rotors in the potential field, colored by their direction. Right: Schematic demonstrating rotors which are composed of spherical point masses that are pushed by random forces, active forces along the rod contour, and the potential energy field. In all simulations, the rod is composed of 21 coarse–grained beads separated by bond length σ. In the dilute limit, the beads are point masses and do not interact with each other. Therefore, the rod diameter is zero, and the aspect ratio $L_{Rod}/d_{Rod} = \infty$.

masses that have no interparticle interactions. Therefore, the rod diameter is zero, and the aspect ratio $L_{Rod}/d_{Rod} = \infty$.

Based on the form of the external potential, and ignoring any directional dependence to the translational drag $D_{\parallel} \approx D_{\perp} = D_T$, there are four dimensionless groupings present in the system: the ratio of rod length to the confinement wavelength L_{Rod}/λ, the ratio of active run length to the rod length $U_0/(D_\theta L_{Rod})$, the translational diffusivity over the rotational diffusivity $D_T/(D_\theta L_{Rod}^2)$, and the trap strength divided by the thermal energy $A/(k_{\mathrm{B}}T)$. For all systems discussed, we choose $D_T/(D_\theta L_{Rod}^2) = 1/6$, following the traditional scaling of rotational diffusion for a thin rod in dilute conditions.[38]

In addition to solving the steady state Smoluchowski equation in a periodic unit cell,

we utilize the mechanics of generalized Taylor dispersion theory to calculate the long-time self-diffusivity of the dilute rods in confinement.[40–42] For brevity, we save the mechanics of the derivation and solution to the dispersion equations for Supplementary Information Section II. of [1].

We implemented our simulations using HOOMD-blue, a molecular dynamics (MD) simulation package in Python.[43] We integrate the Langevin equation using a timestep size of $\Delta t = 0.01\sigma^2/D_T$ for at least $2 * 10^7$ timesteps. Numerical solutions to the field equations were conducted using spectral methods implemented in Dedalus.[44]

4.3 Results and Discussion

To compare the effect of confinement on passive and active rods, we plot the component of the normalized nematic tensor aligned orthogonal to the external field $\langle Q_{yy} \rangle$ in Fig. 4.2 a) and b). The angled brackets indicate the ensemble average of the quantity over all particles and timesteps ($N_{samples}$) for BD simulations. For the solutions to the Smoluchowski equation, the angled brackets indicate the expected value calculated by integrating the probability distribution.

$$\langle Q_{yy} \rangle_{sim} = \frac{1}{N_{samples}} \sum_{i}^{N_{samples}} \left(2\sin^2(\theta_i) - 1\right) \tag{4.7a}$$

$$\langle Q_{yy} \rangle_{theory} = \iint_{\boldsymbol{r},\theta} f(\boldsymbol{r}, \theta)(2\sin^2(\theta) - 1)\mathrm{d}\boldsymbol{r}\mathrm{d}\theta \tag{4.7b}$$

These values are equivalent at steady state.

As the potential strength $A/(k_\mathrm{B}T)$ increases, the rods experience an aligning torque due to their finite length. The potential energy is minimized when all monomers on the rod are located at $x = 0$; therefore, energy is minimized at the expense of rotational entropy by the rotation of the entire rod. In addition to large potential strengths ($A \gg k_\mathrm{B}T$), Q_{yy} is maximized when the rod length increases relative to the wavelength; the

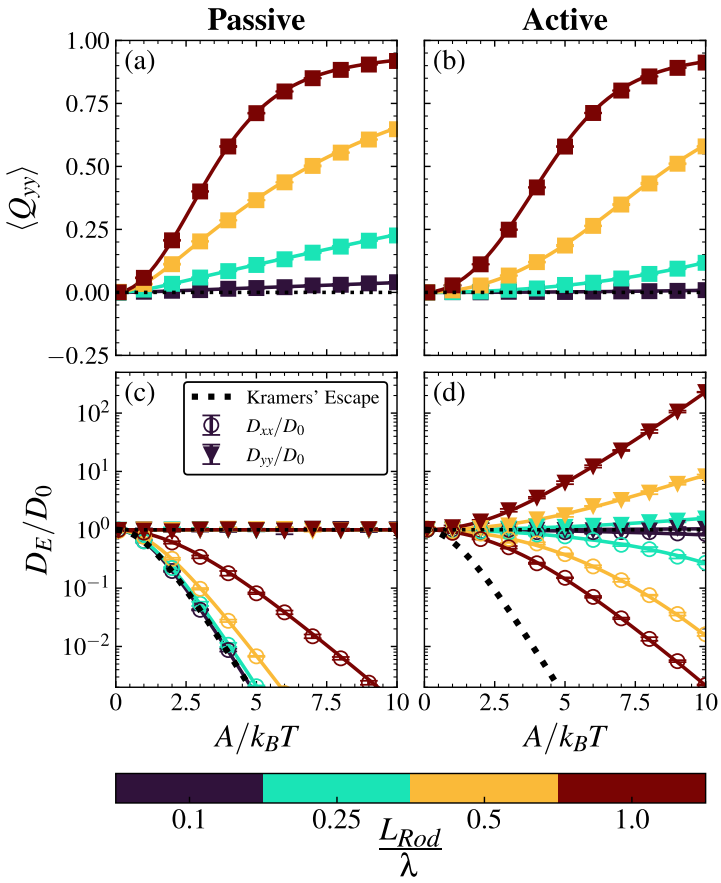

Figure 4.2: Softly confined active rods exhibit significant nematic ordering and dispersion in a direction orthogonal to confinement. Panels (a) and (c) are passive whereas panels (b) and (d) are self-propelled rods with activity $U_0/(D_\theta L_{Rod}) = 3.5$. Panels (a) and (b) show the axial component of the traceless ensemble averaged nematic tensor. Panels (c) and (d) show the components of the effective diffusivity scaled by the bulk diffusivity in the absence of confinement. While the diffusivity across confining channels (D_{xx}/D_0) decreases for both active and passive rods, the active rods exhibit enhanced diffusivity in the direction orthogonal to confinement (D_{yy}/D_0) as rod length and field strength increase. Markers are from Brownian dynamics simulations, solid lines are numerical solutions to the Smoluchoski and dispersion theories. Error bars are standard error of the mean calculated from three independent simulations and when not visible are smaller than the marker size. Dotted lines in panels (c) and (d) are the Kramers' escape solution for diffusivity of a point particle.

energy penalty increases as more of the rod density is moved further from the potential energy minimum. Both active and passive rods exhibit increased nematic ordering as the field strength and rod length increase. Compared to the passive rods, self-propelled

rods at the activity studied exhibit slightly less nematic order at the same trap strength due to their increased ability to escape the trap basin and reorient at a more favorable location.

In Fig. 4.2 c) and d), we calculate the long time self diffusivity of the confined active rods scaled by the bulk diffusivity in the absence of external fields, D_E/D_0. The bulk diffusivity, $D_0 = D_T + U_0^2/(2D_\theta)$, is defined as the sum of the Stoke-Einstein-Sutherland diffusivity D_T and the "swim diffusivity" $U_0^2/(2D_\theta)$ for active species. In the absence of confinement $D_E = D_0$. This normalization isolates the impact of the activity-confinement coupling, instead of capturing the well studied enhancement in bulk diffusivity due to activity.

We plot the components of the diffusivity aligned with the external field, D_{xx}/D_0, and orthogonal to the external field, D_{yy}/D_0, for passive and active rods. For passive rods, D_{xx}/D_0 decreases following a standard Kramers' escape process (dashed black line). Kramers' theory[45–47] indicates that the effective diffusivity scales linearly with the curvature of the potential well and exponentially with the activation energy barrier to hopping. Note that when the rod length is comparable to the wavelength $L_{Rod}/\lambda = 1$, the scaled diffusivity is slightly higher due to the coupling between the density and higher order moments (e.g. nematicity) from the potential. Long rods near the top of the trap are able to reorient so that part of their mass density is in the next basin, creating a weaker activation barrier to escape. In contrast, the scaled dispersivity perpendicular to the field D_{yy}/D_0 remains unaffected by confinement. Transport in the axial direction follows a 1D random walk at its bulk diffusivity $D_{yy} = D_0$. For the purpose of this chapter, we ignored any orientation dependence to the Stokes-Einstein-Sutherland diffusivity, but at most that would modify the results by a factor of two for an infinitely long and thin rod.

For active rods in Fig. 4.2 d), the effective diffusivity between channels (D_{xx}/D_0) decreases as rod length increases. The active forcing is powerful enough to overcome

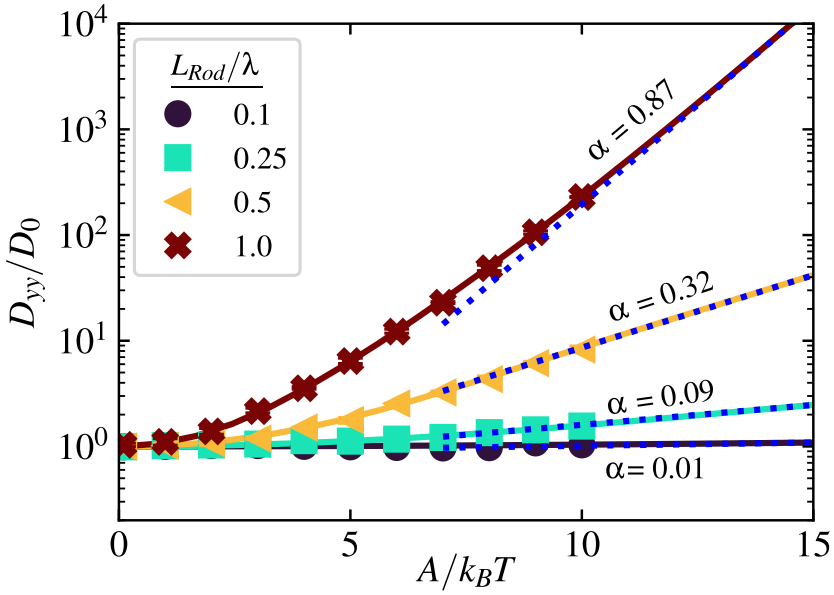

Figure 4.3: 1D monochromatic potentials increase active rod dispersion orthogonal to confinement by preventing reorientation. As rod length increases, the activation barrier against rotation grows. Data points are measured from Brownian dynamics simulations and the solid lines are numerical solutions to the full dispersion theory. The dotted lines are predictions from Eq. 4.8 with n=2. Activity $U_0/(D_\theta L_{Rod}) = 3.5$ Error bars are from three independent simulations and when not visible are smaller than the marker size.

the external field in all cases $F^{act}/F^{ext}_{max} = (U_0 k_B T/D_T)/(A/\lambda) > 1$; however, the large nematic order present as L_{Rod}/λ increases prevents reorientation and inhibits facilitated active escape.

Most surprisingly, the axial diffusivity of active rods in confinement increases by many orders of magnitude such that $D_{yy}/D_0 \gg 1$. Rod alignment via the external potential couples with persistent self-propulsion to increase the dispersion. At strong field strengths and long rod lengths, the rods align nematically inside the channel field, moving ballistically until an energetically unlikely reorientation event occurs. The time between direction reversals is increased by the potential barrier, leading to exponentially longer ballistic runs.

To understand the cause of the increase in dispersion, we can examine the energetics

of direction reversal for confined rods. At strong field strengths, $A \gg k_{\mathrm{B}}T$, the rod number density is focused primarily in the center of the channel. A rod sitting in the center oriented vertically ($\theta = \pi/2$) has an activation energy barrier to change direction to $\theta = 3\pi/2$, which for $L_{Rod}/\lambda \leq 1$ is the energy needed to rotate through the completely horizontal state: $E_{a,rot} = A\left[1 - \mathrm{sinc}\left(\frac{\pi L_{Rod}}{\lambda}\right)\right]$. This activation energy determines the frequency of direction reversal. The activation barrier exponentially lowers the effective *rotational* diffusion coefficient ($D_{E,\theta}$); however, due to the coupling between orientation and persistent self-propulsion, the reduced rotational diffusion increases the effective translational diffusion.

We propose that when the rod is strongly confined, the effective translational diffusivity of an active rod in an external potential may be approximated as

$$D_{E,yy}/D_0 \sim e^{\alpha} \approx e^{nE_{a,rot}/k_BT}, \tag{4.8}$$

where $E_{a,rot}$ is the activation barrier for the rod to rotate and reverse polarity. And n is a factor depending weakly on rod length. Over the course of our study, we found $n \approx 2$, but it is not necessarily constant for all systems.

In Fig. 4.3), we compare the effective diffusivity from our Brownian dynamics simulations (via slope of the mean-squared displacement) with our proposed theoretical model in Eq. 4.8. When confinement strength is weak ($A \ll k_{\mathrm{B}}T$), the effective diffusivity is equivalent to the bulk diffusivity. As the confinement strength increases to $A \gg k_{\mathrm{B}}T$, the effective diffusivity increases exponentially, based on the formation of an activation barrier to rotation $D_{E,yy} \sim 1/D_{E,\theta} \sim e^{\alpha}$. Across an order of magnitude of rod lengths, we obtain proficient agreement between the simulation data and our proposed theoretical model, Eq. 4.8.

Our Smoluchowski formulation allows for a detailed view of the local rod structure found via the probability distribution. In Fig. 4.4a) - c), we calculate the local density,

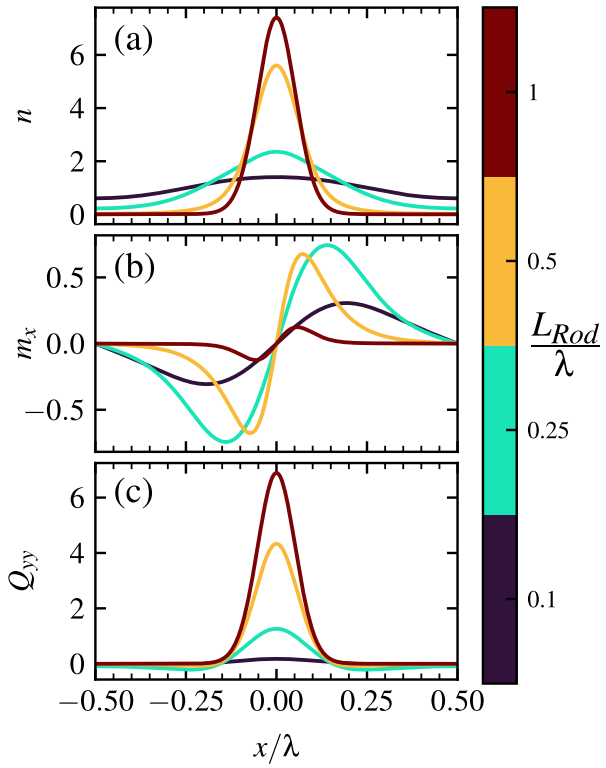

Figure 4.4: Steady state moments of the probability distribution found numerically via Eq. 4.2 for a 1D monochromatic potential $\phi = -A\cos(2\pi x/\lambda)$. Active rods at potential strength $A/(k_{\mathrm{B}}T) = 10$ and activity $U_0/(D_\theta L_{Rod}) = 3.5$. (a) Rod number density (n) across the channel increases due to the large nematic order preventing active escape. (b) Rod polar order against the channels (m_x) exhibits a maximum at intermediate L_{Rod}/λ because the maximum restoring force (A/λ) and active force balance before succumbing to nematic reorientation. (c) Rod nematic order in the channels (Q_{yy}) increases as L_{Rod}/λ grows due to the increased barrier to reorientation.

polarity, and nematicity fields across a single channel at a fixed potential strength of $A/(k_{\mathrm{B}}T) = 10$. The local density ($n(x) = \iint f(x, y, \theta)\mathrm{d}y\mathrm{d}\theta$) increases as L_{Rod}/λ increases. For low L_{Rod}/λ, the active force is easily able to overcome the potential energy barrier and there is a broad density distribution. At large L_{Rod}/λ, the small wavelengths lead to large gradients of the potential energy creating a restoring force similar in magnitude to the active force $A/\lambda \approx 0.48U_0(k_{\mathrm{B}}T/D_T)$ (for $L_{Rod} = \lambda$). Additionally, the strong torques at large L_{Rod}/λ prevents rod orientation (and therefore self-propulsion) out of

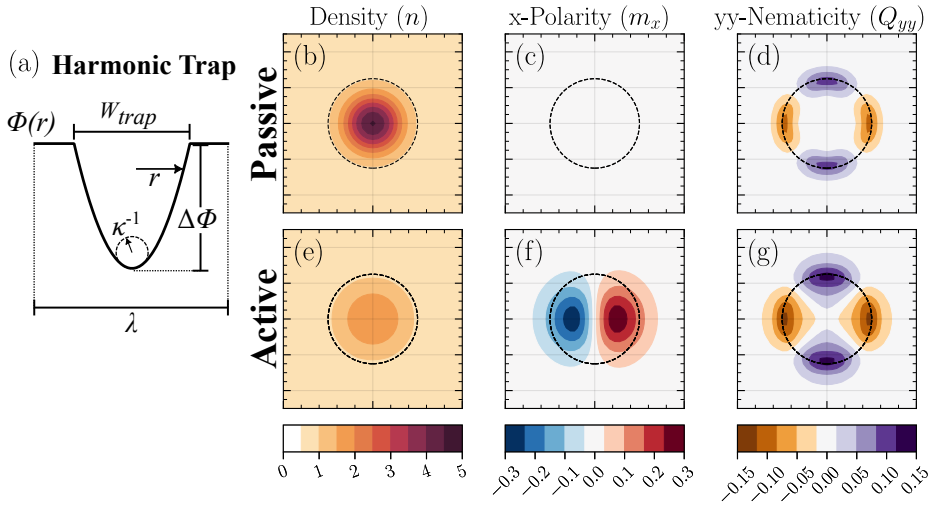

Figure 4.5: (a) An optical trap potential energy field $\phi(r)$ defined as a radially harmonic trap with curvature κ, width W_{trap} and depth $\Delta\phi = \frac{1}{8}\kappa W_{trap}^2$. (b)-(g) Moments of the steady-state probability distribution for rods in an array of optical traps in two dimensions. Upper panels (b,c and d) are for passive (not self-propelled) rods in a harmonic trap, lower panels (e,f and g) are for self-propelled rods with activity set as $U_0/(D_\theta L_{Rod}) = 1.0$. Panels (b) and (e) are the number density of rods, center panels (c) and (f) are the polar order of rods in the x-direction, and right panels (d) and (g) are the nematic order in the y-direction. The circular dashed line represents the edge of the trap. The trap width $W_{trap} = 0.5\lambda$ and trap depth $\Delta\phi = 2k_BT$ gives a curvature $\kappa = 64\lambda^{-1}$. For this example, rod length $L_{Rod} = 0.25\lambda$.

the basin.

Interestingly, the polarity in the x-direction ($m_x(x) = \iint f(x,y,\theta)\cos(\theta)\mathrm{d}y\mathrm{d}\theta$) increases non-monotonically as a function of wavelength. When L_{Rod}/λ is small, the aligning torques on the rods are weak, and the self-propelled rods behave as active spheres, orienting against restoring forces. The polarity should increase with the restoring force, but eventually the torques on the rods dominate and prevent alignment with the x-axis (normal to the soft confinement). Finally, the nematic order ($Q_{yy}(x) = \iint f(x,y,\theta)(2\sin^2(\theta) - 1)\mathrm{d}y\mathrm{d}\theta$) increases with L_{Rod}/λ as large gradients in potential energy along a single filament length rotate the particle.

Although we focused on the special case of a 1D sinusoidal potential, our spectral

formulation (Eq. 4.5) is universal for any well behaved periodic potential energy field. To demonstrate the application of our framework towards more complex potentials, we solved the steady-state probability distribution of a rod in a lattice array of radially parabolic potentials, inspired by an array of optical traps.[42] Optical traps do not necessarily have a parabolic profile for anisotropic colloidal particles[48]; however, this model provides a useful demonstration of the range of energy fields made possible to study.

In Fig. 4.5a), we show a schematic of a parabolic potential described by the trap curvature κ, width W_{trap} and depth $\Delta\phi = \frac{1}{8}\kappa W_{trap}^2$. This parabolic trap biases the rod density to the center, but may also impact the (local) polarity and nematicity of the rods, especially with activity. We cut off the parabolic potential at the width W_{trap} to create a finite activation barrier to escape, we then tile the potential in a square lattice to measure properties of the entire suspension as opposed to motion within a single stiff trap. In Fig. 4.5b)-g), we show the density, x-direction polarity, and yy-direction nematicity for both passive and self-propelled rods, respectively. In Fig. 4.5b) and e), the number density is maximized at the center of the trap. However, the addition of activity allows for particles to more easily escape from the harmonic trap, as previously shown for spherical active particles.[32, 49–52]

Self-propulsion adds an orientation-dependent force to the translational flux, thereby coupling the polar order to potential and concentration gradients in a way not present for passive rods. As shown in Fig. 4.5c) and f), this coupling generates local polar order from the propulsive force "pushing" against the energy barrier, which corresponds to a maxima in polar order in locations where the potential energy gradient is the strongest.

The isotropic nature of the trap prevents global orientational ordering vertically or horizontally; however, the rods will tend to align in such a way that they "hang" over the edge, thereby lowering their potential energy. This creates the quadrupolar structure present in Fig. 4.5d) and g). This effect is modified for active particles because the polar

order induced by pushing against the trap feeds into the local nematic order in regions of high restoring force.

4.4 Conclusions

This chapter presents a general method to study anisotropic active rods in two dimensions under a range of periodic external fields. Extensions to this work include the study of rods in three dimensional confinement, where the Fourier transform of the rod density ($\text{sinc}(\pi L_{Rod}\boldsymbol{k}_{n,m} \cdot \boldsymbol{u})$) remains the same provided that $\boldsymbol{u}$ is now the unit vector in spherical coordinates.

Extending this work to concentrated suspensions of active rods is possible using a modification to the Smoluchowski equation to incorporate a mean-field model.[38, 53, 54] However, mean-field models are only valid in the regime of low rod density, weak inter-particle interactions, and small density correlations, so phenomenological hydrodynamic models are often used to study concentrated active nematic systems.[54] For example, recent theoretical work by Gulati et. al.[55] on concentrated suspensions of polar fluids confined between walls demonstrates that by controlling the wall anchoring and the activity, one can transition between no flow, laminar, shear banded, and vortex lattice flow types. We believe that the machinery of Eq. 4.5 can also extend these phenomenological methods by enabling the addition of a variety of periodic potentials to rod models.

Bibliography

[1] K. J. Modica and S. C. Takatori, *Soft confinement of self-propelled rods: simulation and theory*, *Soft Matter* **20** (2, 2024) 2331–2337.

[2] A. Be'er and G. Ariel, *A statistical physics view of swarming bacteria*, *Movement Ecology* **7** (3, 2019) 9.

[3] M. Bär, R. Großmann, S. Heidenreich, and F. Peruani, *Self-propelled rods: Insights and perspectives for active matter*, *Annual Review of Condensed Matter Physics* **11** (3, 2020) 441–466.

[4] S. J. Kron and J. A. Spudich, *Fluorescent actin filaments move on myosin fixed to a glass surface.*, *Proceedings of the National Academy of Sciences* **83** (9, 1986) 6272–6276.

[5] R. Voituriez, J. F. Joanny, and J. Prost, *Spontaneous flow transition in active polar gels*, *Europhysics Letters (EPL)* **70** (5, 2005) 404–410.

[6] H. Wioland, F. G. Woodhouse, J. Dunkel, J. O. Kessler, and R. E. Goldstein, *Confinement stabilizes a bacterial suspension into a spiral vortex*, *Phys. Rev. Lett.* **110** (6, 2013) 268102.

[7] E. Lushi, H. Wioland, and R. E. Goldstein, *Fluid flows created by swimming bacteria drive self-organization in confined suspensions*, *Proceedings of the National Academy of Sciences* **111** (6, 2014) 9733–9738.

[8] K.-T. Wu, J. B. Hishamunda, D. T. N. Chen, S. J. DeCamp, Y.-W. Chang, A. Fernández-Nieves, S. Fraden, and Z. Dogic, *Transition from turbulent to coherent flows in confined three-dimensional active fluids*, *Science* **355** (2017), no. 6331 eaal1979, [https://www.science.org/doi/pdf/10.1126/science.aal1979].

[9] S. Chen, P. Gao, and T. Gao, *Dynamics and structure of an apolar active suspension in an annulus*, *Journal of Fluid Mechanics* **835** (11, 2017) 393–405.

[10] A. Opathalage, M. M. Norton, M. P. N. Juniper, B. Langeslay, S. A. Aghvami, S. Fraden, and Z. Dogic, *Self-organized dynamics and the transition to turbulence of confined active nematics*, *Proceedings of the National Academy of Sciences* **116** (2, 2019) 4788–4797.

[11] Z. You, D. J. G. Pearce, and L. Giomi, *Confinement-induced self-organization in growing bacterial colonies*, *Science Advances* **7** (1, 2021) 10694.

[12] C. G. Wagner, M. M. Norton, J. S. Park, and P. Grover, *Exact coherent structures and phase space geometry of preturbulent 2d active nematic channel flow*, *Phys. Rev. Lett.* **128** (1, 2022) 028003.

[13] A. Doostmohammadi, J. Ignés-Mullol, J. M. Yeomans, and F. Sagués, *Active nematics*, *Nature Communications* **9** (8, 2018) 3246.

[14] D. Needleman and Z. Dogic, *Active matter at the interface between materials science and cell biology*, *Nature Reviews Materials* **2** (7, 2017) 17048.

[15] C. Bechinger, R. D. Leonardo, H. Löwen, C. Reichhardt, G. Volpe, and G. Volpe, *Active particles in complex and crowded environments*, *Reviews of Modern Physics* **88** (11, 2016) 045006.

[16] S. P. Thampi, *Channel confined active nematics*, *Current Opinion in Colloid & Interface Science* **61** (10, 2022) 101613.

[17] K. J. Modica, A. K. Omar, and S. C. Takatori, *Boundary design regulates the diffusion of active matter in heterogeneous environments*, *Soft Matter* **19** (2023), no. 10 1890–1899.

[18] J. Elgeti and G. Gompper, *Wall accumulation of self-propelled spheres*, *EPL (Europhysics Letters)* **101** (2, 2013) 48003.

[19] Y. Fily, A. Baskaran, and M. F. Hagan, *Dynamics of self-propelled particles under strong confinement*, *Soft Matter* **10** (2014), no. 30 5609–5617.

[20] F. Smallenburg and H. Löwen, *Swim pressure on walls with curves and corners*, *Phys. Rev. E* **92** (9, 2015) 032304.

[21] W. Yan and J. F. Brady, *The curved kinetic boundary layer of active matter*, *Soft Matter* **14** (2018), no. 2 279–290.

[22] H. H. Wensink and H. Löwen, *Aggregation of self-propelled colloidal rods near confining walls*, *Physical Review E* **78** (9, 2008) 031409.

[23] J. Elgeti and G. Gompper, *Self-propelled rods near surfaces*, *EPL (Europhysics Letters)* **85** (2, 2009) 38002.

[24] G. Li and J. X. Tang, *Accumulation of microswimmers near a surface mediated by collision and rotational brownian motion*, *Phys. Rev. Lett.* **103** (8, 2009) 078101.

[25] A. Zöttl and H. Stark, *Emergent behavior in active colloids*, *Journal of Physics: Condensed Matter* **28** (5, 2016) 253001.

[26] Z. Wang, Y.-F. Chen, H.-Y. Chen, Y.-J. Sheng, and H.-K. Tsao, *Mechanical pressure, surface excess, and polar order of a dilute rod-like nanoswimmer suspension: role of swimmer–wall interactions*, *Soft Matter* **14** (2018), no. 15 2906–2914.

[27] J. Clemmens, H. Hess, J. Howard, and V. Vogel, *Analysis of microtubule guidance in open microfabricated channels coated with the motor protein kinesin*, *Langmuir* **19** (3, 2003) 1738–1744.

[28] J. Clemmens, H. Hess, R. Lipscomb, Y. Hanein, K. F. Böhringer, C. M. Matzke, G. D. Bachand, B. C. Bunker, and V. Vogel, *Mechanisms of microtubule guiding*

on microfabricated kinesin-coated surfaces: Chemical and topographic surface patterns, *Langmuir* **19** (12, 2003) 10967–10974.

[29] R. Bunk, J. Klinth, L. Montelius, I. A. Nicholls, P. Omling, S. Tågerud, and A. Månsson, *Actomyosin motility on nanostructured surfaces*, *Biochemical and Biophysical Research Communications* **301** (2, 2003) 783–788.

[30] R. Bunk, M. Sundberg, A. Månsson, I. A. Nicholls, P. Omling, S. Tågerud, and L. Montelius, *Guiding motor-propelled molecules with nanoscale precision through silanized bi-channel structures*, *Nanotechnology* **16** (4, 2005) 710–717.

[31] A. Ashkin and J. M. Dziedzic, *Optical trapping and manipulation of viruses and bacteria*, *Science* **235** (3, 1987) 1517–1520.

[32] S. C. Takatori, R. De Dier, J. Vermant, and J. F. Brady, *Acoustic trapping of active matter*, *Nature Communications* **7** (2016), no. 1 10694.

[33] T. L. Min, P. J. Mears, L. M. Chubiz, C. V. Rao, I. Golding, and Y. R. Chemla, *High-resolution, long-term characterization of bacterial motility using optical tweezers*, *Nature Methods* **6** (10, 2009) 831–835.

[34] H. H. Wensink, H. Löwen, M. Marechal, A. Härtel, R. Wittkowski, U. Zimmermann, A. Kaiser, and A. M. Menzel, *Differently shaped hard body colloids in confinement: From passive to active particles*, *The European Physical Journal Special Topics* **222** (11, 2013) 3023–3037.

[35] R. Wittkowski and H. Löwen, *Dynamical density functional theory for colloidal particles with arbitrary shape*, *Molecular Physics* **109** (12, 2011) 2935–2943.

[36] H. Hansen-Goos and K. Mecke, *Fundamental measure theory for inhomogeneous fluids of nonspherical hard particles*, *Phys. Rev. Lett.* **102** (1, 2009) 018302.

[37] A. Baskaran and M. C. Marchetti, *Hydrodynamics of self-propelled hard rods*, *Phys. Rev. E* **77** (1, 2008) 011920.

[38] M. Doi and S. F. Edwards, *The Theory of Polymer Dynamics (International Series of Monographs on Physics)*. Oxford University Press, 1988.

[39] M. Doi, T. Shimada, and K. Okano, *Concentration fluctuation of stiff polymers. II. dynamical structure factor of rod-like polymers in the isotropic phase*, *The Journal of Chemical Physics* **88** (3, 1988) 4070–4075.

[40] J. F. Morris and J. F. Brady, *Self-diffusion in sheared suspensions*, *Journal of Fluid Mechanics* **312** (4, 1996) 223–252.

[41] R. N. Zia and J. F. Brady, *Single-particle motion in colloids: force-induced diffusion*, *Journal of Fluid Mechanics* **658** (9, 2010) 188–210.

[42] J. M. Barakat and S. C. Takatori, *Enhanced dispersion in an oscillating array of harmonic traps*, *Physical Review E* **107** (1, 2023) 014601.

[43] J. A. Anderson, J. Glaser, and S. C. Glotzer, *HOOMD-blue: A python package for high-performance molecular dynamics and hard particle monte carlo simulations*, *Computational Materials Science* **173** (2, 2020) 109363.

[44] K. J. Burns, G. M. Vasil, J. S. Oishi, D. Lecoanet, and B. P. Brown, *Dedalus: A flexible framework for numerical simulations with spectral methods*, *Phys. Rev. Res.* **2** (4, 2020) 023068.

[45] H. Kramers, *Brownian motion in a field of force and the diffusion model of chemical reactions*, *Physica* **7** (4, 1940) 284–304.

[46] H. Brinkman, *Brownian motion in a field of force and the diffusion theory of chemical reactions*, *Physica* **22** (1, 1956) 29–34.

[47] H. Brinkman, *Brownian motion in a field of force and the diffusion theory of chemical reactions. ii*, *Physica* **22** (1, 1956) 149–155.

[48] J. L. Abbott, J. A. Spiers, Y. Gao, D. G. A. L. Aarts, and R. P. A. Dullens, *Colloidal rods in optical potential energy landscapes*, *Journal of Physics D: Applied Physics* **52** (1, 2019) 024002.

[49] A. Pototsky and H. Stark, *Active brownian particles in two-dimensional traps*, *EPL (Europhysics Letters)* **98** (6, 2012) 50004.

[50] A. Geiseler, P. Hänggi, and G. Schmid, *Kramers escape of a self-propelled particle*, *The European Physical Journal B* **89** (8, 2016) 175.

[51] D. Wexler, N. Gov, K. O. Rasmussen, and G. Bel, *Dynamics and escape of active particles in a harmonic trap*, *Phys. Rev. Res.* **2** (1, 2020) 013003.

[52] E. Woillez, Y. Kafri, and N. S. Gov, *Active trap model*, *Phys. Rev. Lett.* **124** (3, 2020) 118002.

[53] A. Baskaran and M. C. Marchetti, *Enhanced diffusion and ordering of self-propelled rods*, *Phys. Rev. Lett.* **101** (12, 2008) 268101.

[54] M. C. Marchetti, J. F. Joanny, S. Ramaswamy, T. B. Liverpool, J. Prost, M. Rao, and R. A. Simha, *Hydrodynamics of soft active matter*, *Rev. Mod. Phys.* **85** (7, 2013) 1143–1189.

[55] P. Gulati, S. Shankar, and M. C. Marchetti, *Boundaries control active channel flows*, *Frontiers in Physics* **10** (7, 2022) 1.

Chapter 5

Partitioning of Motile Bacteria in Aqueous Two-Phase Systems

In this short chapter I will utilize the theory developed in Chapter 4 to model the experimentally observed partitioning of *Bacillus subtilis* in a phase-separated dextran (DEX)/ polyethylene glycol (PEG) aqueous mixture. We hypothesize that the bacteria sequester into the two phases due to a chemical affinity between dextran polymer and the bacteria cell wall. Non-motile bacteria are observed to partition exclusively into the DEX-rich phase in all conditions tested, while motile bacteria penetrate across the soft DEX/PEG interface and partition variably among the two phases.

We model the two-phase system as a fixed, periodic, lamellar pattern in space. A square wave potential mimics the affinity a bacterium feels in the two domains. The low energy region corresponds to the DEX-rich phase and the high energy region corresponds to the PEG-rich phase. We fit the unknown parameters of a Smoluchowski-based model from the experimental data, and find strong agreement between the data and the model.

This chapter is the result of a collaboration with Prof. Joonwoo Jeong, Prof. Robert J. Mitchell, and Jiyong Cheon at the Ulsan National Institute of Science and Technology (UNIST), as well as Kyu Hwan Choi and Prof. Sho C. Takatori at UC Santa Barbara. JC and KHC performed all experiments. KJM developed the model and performed calculations. JJ, RJM, and SCT supervised the study.

An updated version of this work has been submitted for publication and is available on arXiv:

[1] J. Cheon, K. H. Choi, K. J. Modica, R. J. Mitchell, S. C. Takatori, and J. Jeong, *Motility modulates the partitioning of bacteria in aqueous two-phase systems*, (5,2024) arXiv:2405.0899.

5.1 Introduction

The behavior of living bacteria in multiphase aqueous suspensions plays an important role in many biological and ecological systems, including the determination of infection routes, and cell sorting [2–4]. Prior work has shown that living bacteria immersed in an aqueous two-phase system (ATPS) of dextran (DEX) and polyethylene glycol (PEG) eventually partition into one phase [5–10]. However, the basic mechanisms underlying the biased partitioning of living bacteria into different phases of ATPS mixtures, especially in the presence of bacteria motility, remain unknown.

For systems at thermodynamic equilibrium, passive colloidal particles immersed in a DEX/PEG mixture have been shown to partition into different bulk phases depending on the surface properties of the colloids[11–14]. By coating the colloidal surfaces with different chemical moieties, the partitioning of passive colloids into the DEX-rich versus PEG-rich phases follows the equilibrium-based Boltzmann distribution, $\sim \exp\left(-V(\mathbf{x})/(k_{\mathrm{B}}T)\right)$, where $V(\mathbf{x})$ describes the interaction energy landscape of the particle in the mixture [14–16]. In contrast, the partitioning of motile bacteria in two-phase systems is not guaranteed to obey Boltzmann statistics because the bacteria generate nonequilibrium forces through their motility.

In this chapter, we combine experiment and theory to study the partitioning of motile bacteria in a DEX/PEG system using *Bacillus subtilis* as a model organism. As shown in Fig. 5.1A-B, we confined the bacteria into a quasi-2D system immersed in a phase-separated mixture of PEG-rich domains surrounded by DEX-rich continous phase. We observed that non-motile *B. subtilis* undergo Brownian motion only and partitioned entirely into the DEX-rich phase (Fig. 5.1C). In contrast, the motile *B. subtilis* distributed more evenly across the two phases and reached a dynamic steady-state, with bacteria frequently crossing the DEX/PEG interface (Fig. 5.1D). When observing the crossing

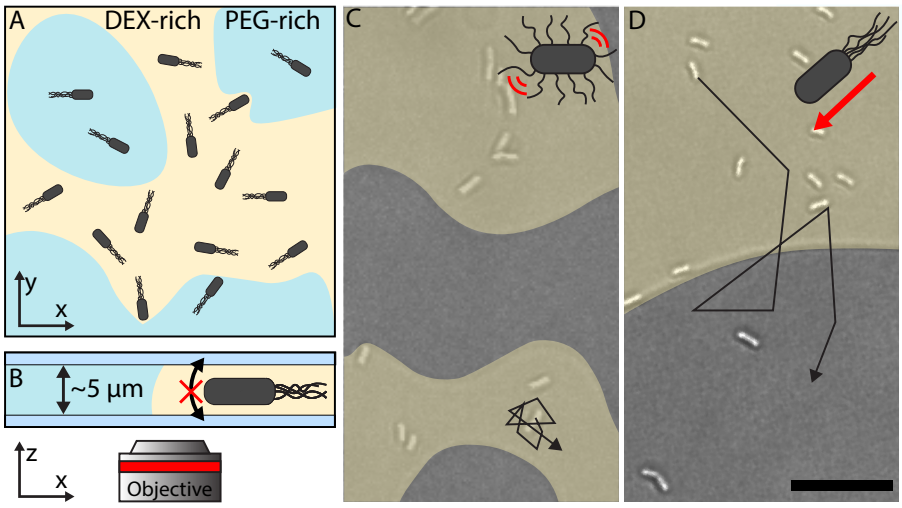

Figure 5.1: Motile bacteria *B. subtilis* immersed in an aqueous two-phase system (ATPS) of dextran (DEX) and polyethylene glycol (PEG) partition more evenly across the two phases compared to non-motile strains, which partition exclusively into the DEX-rich phrase. A) Top and B) side views of our quasi-2D setup for measuring bacterial partitioning. The chamber thickness is 5 µm to prevent the bacteria from orienting vertically (average body length $\approx$ 5 µm). C) The non-motile strain partitions exclusively into the DEX-rich phase (yellow region), whereas the D) motile strain partitions into both phases. Total DEX concentration is 3.2 wt/wt%, PEG concentration is 2.5 wt/wt%. The scale bar is 20 µm.

of bacteria across the two-phase boundary, we observed asymmetry in the interfacial deformation, always toward the DEX-rich phase: when crossing from DEX $\rightarrow$ PEG, we observed the interface bend outwards away from the bacterium, generating an antiparallel force against bacterial swimming. In contrast, when crossing from PEG $\rightarrow$ DEX, we observed the interface bend inwards towards the bacteria, generating a parallel force aligned with swimming. Based on these observations, we hypothesized that the chemical affinity between dextran sugars and the chemical components on the *B. subtilis* cell wall acts to weakly confine the bacteria within the DEX-rich phase, similar to the partitioning mechanism for synthetic colloids. However, motility can generate sufficient mechanical forces to overcome the soft confinement and propel the bacteria into the PEG-rich phase. A dynamic steady-state between these two forces gives a partitioning ratio of motile bacteria between the two phases.

5.2 Experiments of Bacteria in Aqueous Two-Phase Systems

To quantify the degree of bacterial partitioning, we define the partitioning ratio as the number of bacteria in the DEX-rich phase divided by the total number of bacteria in the sampled area (see Supplementary Figs. 5.5 and 5.6). As shown in Fig. 5.2, all non-motile *B. subtilis* are trapped in the DEX-rich phase across all dextran concentrations tested (1.5 - 8 wt/wt%) with fixed PEG concentration (2.5 wt/wt%). In contrast, the partitioning ratio for the motile bacteria increased monotonically from 0.58 ± 0.10 at 1.5 wt/wt% DEX concentration, to 1 (completely in the DEX-rich phase) at 8 wt/wt%.

Several possible mechanisms may explain the biased partitioning of the bacteria, including motility induced phase separation (MIPS), chemotaxis, and chemical affinity.

One possible mechanism is based on the difference in viscosities of the PEG-rich and DEX-rich phases. Larger drag in the DEX-rich phase may slow down the bacteria, leading to an accumulation in the DEX-rich phase from an effect analogous to MIPS of active Brownian particles [17–19]. In a control experiment, we measured the bacteria swim speeds in the DEX-rich phase (30.7 ± 6.1 μm/s) and in the PEG-rich phase (34.5 ± 6.4 μm/s) at 3.2 wt/wt% dextran concentration. Variable swimming speeds would produce a density distribution that scales as $n(x) \sim 1/U(x)$, and we expect the ≈ 10% slower speeds in the DEX-rich phase to give a partitioning ratio, $n_{\mathrm{DEX}}/(n_{\mathrm{DEX}} + n_{\mathrm{PEG}}) = (1 + U_{\mathrm{DEX}}/U_{\mathrm{PEG}})^{-1} \approx 0.52$, which does not fully explain the separation observed in our experiments, 0.78 ± 0.08. Another possible mechanism is bacterial sensing of chemical attractants through chemotaxis. *B. subtilis* is attracted by sugar gradients [20]. Upon imaging the DEX-PEG interface using dextran-FITC (see Supplementary Fig. 5.7), we observed a sharp gradient of dextran near the interface over a narrow width of ≈ 2 μm, surrounded by a constant dextran concentration in the bulk phases outside of this narrow interface. Since chemotaxis requires chemical gradients to persist over distances larger than the run length (≫ 100 μm) and the body length of an individual bacterium (≈ 5 μm) [21], chemotaxis is unlikely to explain the biased partitioning of motile bacteria in our experiments.

We hypothesized that the chemical affinity of the DEX-rich phase with the chemical components on the bacterial cell wall [10] drives the partitioning. To these ends, we performed optical tweezer experiments to drag a single bacterium across the DEX-PEG interface and measured the forces required to cross the two-phase boundary (Fig. 5.3A). We attached a tracer silica bead as a calibration handle to the bacteria cell wall using click chemistry (See Fig. 5.3A, Supplementary Figs. 5.8). We used silica beads because precise forces are easier to compute on spherical trapped particles, and because the bead can be adjusted to sit at the PEG-DEX boundary without creating additional interfacial

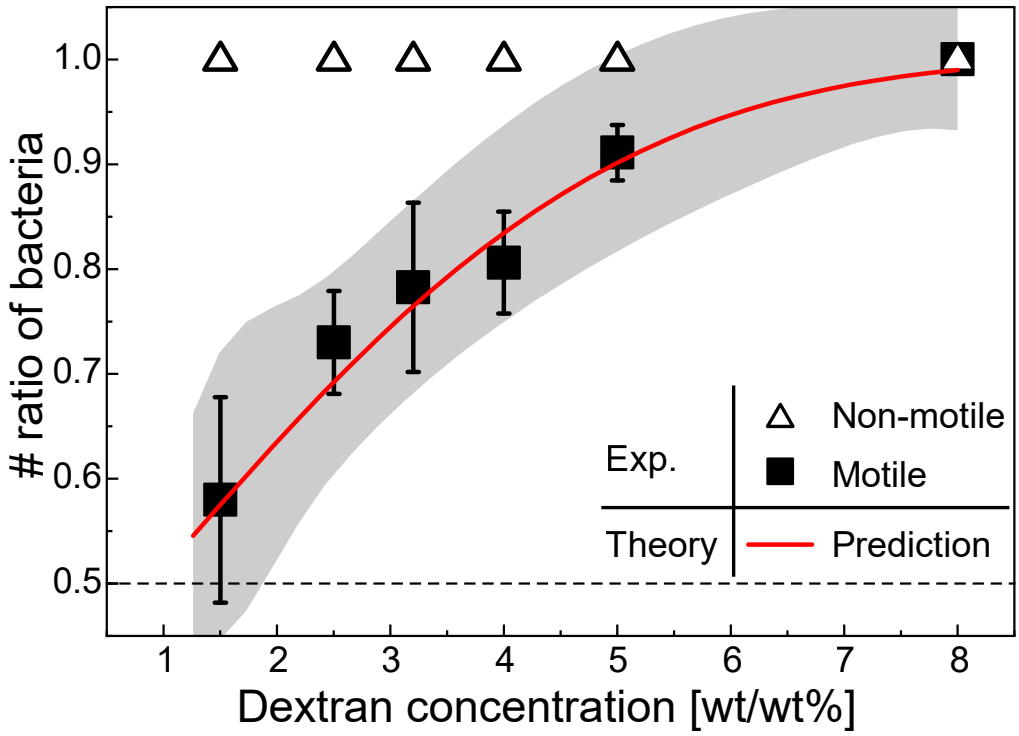

Figure 5.2: Experimental and predicted partitioning ratios of bacteria in DEX-rich phase versus dextran concentration of the overall mixture, where open and filled markers are experimental results of non-motile and motile bacteria, respectively, and the red solid curve is the predicted partitioning ratio based on our theory, Eqs. 5.1 and 5.2. The shaded region represents the 95% confidence band of our model. The horizontal dash line at 0.5 represents a theoretical partitioning ratio when the two-phase boundary vanishes at the critical composition.

deformations. We translated the trap location from the DEX-rich phase into the PEG-rich phase at sufficiently small speeds (0.5 or 2 μm/s) to ignore the viscous drag force on the bead. We measured the displacement of the bead center from the trap center to measure the force generated by the two-phase boundary on the bacterium, F_{int}, as shown in Fig. 5.3B and Supplementary Fig. 5.8.

First, consistent with our initial observations of interface deformation upon bacteria two-phase crossing, we observed that the interface always applies a force on *B. subtilis* towards the DEX-rich phase. As the bacterium body crossed the interface from DEX-

rich to PEG-rich phases, the interface deformed and pulled the bacterium back towards the DEX-rich phase, causing the magnitude of the net force to increase as a function of distance. When the magnitude of F_{int} reached the maximum force, F_{max}, the interface slipped along the bacterium surface as the bacterium penetrated completely across the interface and the interface snapped back to a planar geometry on the trailing edge of the bacterium. At this point, the force suddenly released to zero and the bacterium was now submerged completely inside the PEG-rich phase.

We conducted the measurement across several different dextran compositions in the ATPS mixture. As shown in Fig. 5.3C, F_{max} has magnitudes $\sim \mathcal{O}(\text{pN})$ and increases linearly with dextran concentration. Our measurements corroborate the hypothesis that thermal forces alone are not sufficient to allow non-motile bacteria to cross the two-phase boundary ($1k_{\text{B}}T/1\mu\text{m} \approx 10^{-3}\text{pN} \ll \mathcal{O}(\text{pN})$). Therefore, in the absence of a propulsion force, all non-motile bacteria partitioned into the DEX-rich phase across all conditions tested in Fig. 5.2. In contrast, for motile bacteria, a propulsion force of magnitude $F_{\text{prop}} \sim \mathcal{O}(\text{pN})$ is sufficiently large to overcome the forces generated by the interface, F_{max}. As the dextran concentration increases, the force needed to cross into the PEG-rich phase grows quasi-linearly (see Fig. 5.3). At large dextran concentrations, 8wt/wt%, the interfacial forces F_{int} are too strong for the laser trap to drag the bacteria completely inside the PEG-rich phase. We lose the handle bead prior to crossing the interface and we are unable to measure F_{max}. Consistent with this observation, the motile *B. subtilis* partitioned completely inside the DEX-rich phase at 8wt/wt% dextran concentration, likely because the propulsion forces were always smaller than the interface barrier, $F_{\text{prop}} < F_{\text{max}}$.

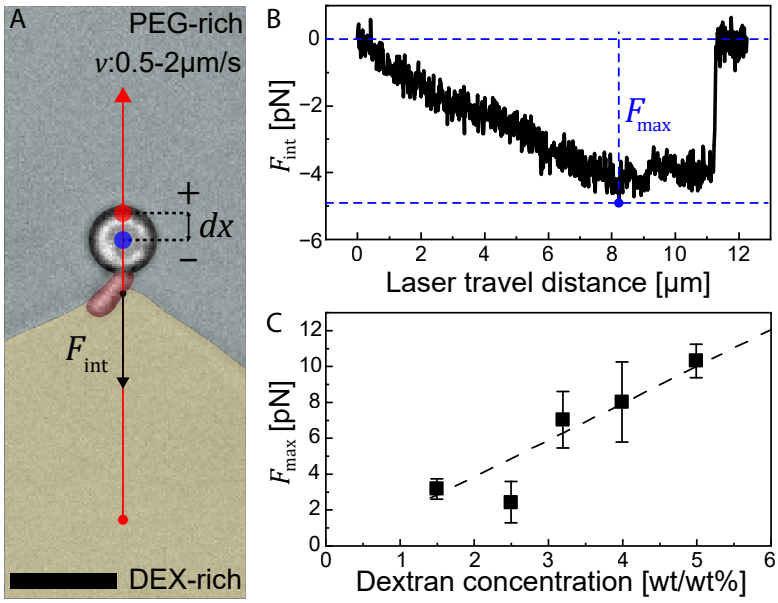

Figure 5.3: Optical laser tweezers were used to drag a single bacterium across the two-phase boundary and measure the forces on the bacterium. A) Representative snapshot of a bacterium attached to a tracer bead crossing the interface. The red solid arrow is the moving path of the optical trap. The force generated by the interface, F_{int}, is calculated by measuring the displacement, dx, between the laser focus (red dot) and the tracer bead center (blue dot). Negative sign means the force is directed against the moving path. The scale bar is 5 μm. B) Representative force profile of F_{int} as the bacterium crosses the two-phase boundary. The laser travel distance is set to zero when the bacterium-bead assembly feels zero interface force. C) Maximum forces (F_{max}) at various dextran concentrations of the ATPS mixture. Dashed lines represent a linear regression for parameter estimation in our theory, Eq. 5.1.

5.3 Model of Bacteria Partitioning

To corroborate our experimental measurements, we model the affinity of the bacteria to the DEX-rich phase as an external field which drives the bacteria to regions of high dextran concentration. We then develop an active Brownian particle model that predicts the partitioning of self-propelled particles subject to that potential driving force.

The Smoluchowski equation describing the evolution of probability for a dilute system

of swimming rod-like particles in a 1-D potential field is given by [22, 23]

$$\frac{\partial P}{\partial t} + \frac{\partial}{\partial x}\left[\frac{P}{\zeta}\left(F_{\text{prop}}\cos\theta - k_{\text{B}}T\frac{\partial \ln P}{\partial x} - \frac{\partial V}{\partial x}\right)\right] + \frac{\partial}{\partial \theta}\left[P\left(-\frac{1}{\tau_R}\frac{\partial \ln P}{\partial \theta} - \frac{1}{\zeta_R}\frac{\partial V}{\partial \theta}\right)\right] = 0, \quad (5.1)$$

where x and θ are the position and orientation of the active particle, ζ and ζ_R are translational and rotational drag coefficients, F_{prop} is the propulsive force, τ_R is the reorientation time, and $V(x, \theta)$ encodes the energetic cost for the bacterium to move from the DEX-rich phase to the PEG-rich phase (see Supplementary Information for the functional form). Approximating the bacterium as a thin rod, we can relate their rotational and translational drag coefficients using the length of the bacterium $\zeta/\zeta_R = 6/\ell_{\text{bact}}$. For simplicity we ignore the orientation dependence on the translational drag coefficient, and we treat the PEG-rich and DEX-rich phases as a 1-D lamellar system with equal domain width $L/2$ and periodicity L. This model can be described with 5 dimensionless parameters: the ratio of the maximum restoring force to the propulsive force $F_{\text{max}}/F_{\text{prop}}$, the propulsive force relative to the thermal energy $(F_{\text{prop}}L)/k_{\text{B}}T$, the thermal diffusivity relative to the reorientation time $(L^2\zeta)/(\tau_R k_{\text{B}}T)$, the scaled bacteria length ℓ_{bact}/L and the scaled interface width δ/L. δ is the length-scale over which the phase transitions from pure PEG-rich to pure DEX-rich. We allow the reorientation time τ_R to be determined independently from the drag to account for non-thermal reorientation mechanisms.

Based on this theoretical model, we solved the steady-state Smoluchowski equation using the methods described in Chapter 4. The partitioning ratio is determined by the fraction of bacteria in the DEX-rich phase:

$$\frac{n_{\text{DEX}}}{n_{\text{DEX}} + n_{\text{PEG}}} = \int_0^{2\pi}\int_{-L/4}^{L/4} P(x,\theta)\; dx\; d\theta \quad (5.2)$$

We integrate between $\pm L/4$ because that is the energetically favorable DEX-rich phase,

and the rest of the domain is the PEG-rich phase. Based on the average measured propulsion force of $F_{\text{prop}} \approx 10\text{pN}$ (See Supplementary Fig. 5.9), we use a linear regression to relate the dextran concentration to the maximum restoring force (see Fig. 5.3C) to determine the force ratio, $F_{\text{max}}/F_{\text{prop}}$. Due to the large parameter space, we use the experimentally determined propulsion force and bacteria length to set $(F_{\text{prop}}L)/k_{\text{B}}T = 5 * 10^5$ and $\ell_{\text{bact}}/L = 0.025$. We find the remaining parameters (δ/L and $(L^2\zeta)/(\tau_R k_{\text{B}}T)$) using a nonlinear-least-squares regression, while bounding them to be within a realistic range based on the experimental system. Due to the order of magnitude difference in parameter values, the regression was performed on their logarithms and converged to $\log_{10}[(L^2\zeta)/(\tau_R k_{\text{B}}T)] = 8.0 \pm 2.0$ and $\log_{10}[\delta/L] = -2.6 \pm 1.8$.

As shown in Fig. 5.2 our model is able to predict the increased partitioning as the maximum restoring force grows (dextran concentration is obtained from F_{max} by the regression in Fig. 5.3C). Like the experimental trend of motile bacteria, the prediction line also monotonically increases with dextran concentration from 0.57 ± 0.14 at 1.5 wt/wt% to 0.99 ± 0.07 at 8 wt/wt%, corresponding to experimental ratios of 0.58 ± 0.10 and 1 respectively. As the energy barrier (and F_{max}) grows, it becomes difficult for bacteria to escape across the interface using their swim force alone. When this occurs, bacteria become trapped in the low energy region until they make a statistically unlikely Brownian move into the PEG-rich region. By the same logic, when the energy barrier is weak the motile bacteria can easily penetrate the interface and evenly distribute over the two phases.

5.4 Discussion and Conclusions

The solution to the Smoluchowski equation is the steady-state probability density of dilute active rods as a function of position and orientation. When we integrate the

distribution to get the partitioning ratio, we lose much of the fined grained detail; as such, there are multiple sets of parameters that give identical partitioning. In our case the parameters $(L^2\zeta)/(\tau_R k_{\mathrm{B}}T)$ and δ/L are strongly anticorrelated, with correlation coefficients nearing -0.99. We expect this is the primary cause for the large uncertainty in the parameter estimation. Deconvoluting the two parameters would require additional measurements capturing the distribution of bacteria throughout space and orientation.

A clear source of potential error in our model is the assumption that the two phases form a lamellar pattern with a fixed and flat interface. As seen in Fig. 5.1, the DEX-rich continuous phase and PEG-rich dispersed phase have a highly curved interface due to the ultra-low interfacial tension between the two phases. The interface is easily deformed by the *B. subtilis*, which can drag the DEX-rich phase behind it when a bacterium passes through the interface. The deformation of the interface creates additional nonconservative interfacial tension-derived forces that are present in the measured $F_{\max}$. This makes it challenging to define a free energy functional that describes the affinity of the bacteria to each phase. The *B. subtilis* have a large dispersity in body length, propulsion force, and tumbling rate. This heterogeneity means that some bacteria will be more likely to cross the interface than others, potentially enabling the ATPS to partition and sort the cells according to the properties. These factors will all increase the uncertainty of the theoretical model and parameter estimation. Finally, as we discussed previously, while we do not expect MIPS from a viscosity difference to be enough to explain the preferential partitioning present in our system, it may slightly enhance the partitioning effect as well. The bacteria propulsion force and the PEG-rich domain size heterogeneities are shown in Supplementary Fig. 5.9.

In conclusion, we studied the competition between motility and two-phase boundaries on the biased partitioning of active *B. subtilis* using experiment and theory. The motility of *B. subtilis* helps to mix the bacteria across both DEX-rich and PEG-rich phases by

providing a large propulsion force, $F_{\text{prop}} \approx 10\text{pN}$, to overcome the maximum interfacial force. We found that the chemical affinity of the *B. subtilis* cell wall with the DEX-rich phase generates interfacial forces on the bacterium with magnitudes $F_{\text{max}} = 2\text{pN}$ to 10pN depending on dextran composition.

5.5 Supplementary Information

5.5.1 Experimental Methods

Bacterial cell culture

For the partitioning-ratio measurements, mid-exponentially growing *Bacillus subtilis* strain ATCC 6051 was used. For this, bacterial colonies were first cultured overnight on a lysogeny broth (Duchefa Biochemie, USA) agar plate at 37°C. A single colony was transferred into sterile terrific broth (TB; MBcell, Republic of Korea) and cultured in a shaking chamber (250 rpm) at 37°C. After overnight growth, an aliquot of the bacterial culture was transferred to fresh TB (O.D. = 0.03) and cultured under the same condition for 2.5 hours (O.D. $\sim$ 0.5). At this point, the bacteria were pelleted and resuspended in a sterile M9 minimal medium (MBcell, Republic of Korea) to prevent further division.

For the optical tweezers experiments, a single colony of *Bacillus subtilis* strain ATCC 6051, grown as described above, was inoculated into 2 ml of TB, and cultured in a shaking incubator (100 rpm) at 37°C. After overnight growth, an aliquot of the bacterial culture was transferred to fresh TB (1:10 dilution) and cultured under the same condition for $\sim$4 hours. Then 2 ml of bacterial suspension were then pelleted (6k RCF for 1 min) and washed in deionized water. This was repeated five times before the cells were resuspended in 400μL of deionized water.

Sample preparation

We utilized two different polymers: PEG (Polyethylene Glycol) with a molecular weight of 35,000 Da from Sigma-Aldrich (USA), and dextran with a molecular weight of 500,000 Da from Spectrum (USA), to create an Aqueous Two-Phase System (ATPS). Both polymers were dissolved in M9 (for partitioning ratio measurement) or deionized water (for optical tweezers experiment) to measure the partitioning ratio and force, respectively. The dextran concentrations were systematically adjusted to achieve final concentrations (including bacteria) of 1.5, 2.5, 3.2, 4, 5, and 8 wt/wt%, while the PEG concentration was maintained at 2.5 wt/wt%. The final bacterial densities were adjusted to an optical density (O.D. at 600 nm) of 1 (partitioning ratio measurement) or 0.05 (force measurement) by pelleting the bacteria at 8k RCF for 1 min and resuspending them in an appropriate volume of either M9 or deionized water.

The quasi-2D cell gap was controlled by the volume of the bacterial ATPS solution. For example, to measure the partitioning ratio of bacteria, a $\sim 1.3\mu$L volume of the bacterial ATPS solution is sandwiched between a polymeric, air-permeable coverslip (purchased from SPL Life Science, Republic of Korea). Based on the area of the coverslip (254 mm^2, 9 mm diameter), the cell gap was estimated to be $\ll 5\mu$m with the two phases to be horizontally separated by an interface. In the optical tweezers experiment, we used a 25×25 mm^2 coverslip where the cell gap was $\ll 5\mu$m.

A confocal image, taken with a Leica SP8 Resonant Scanning Confocal microscope using a solution containing dissolved Alexa Fluor 647-labeled dextran (40,000 Da) dextran in a 3.2 wt/wt% dextran and 2.5 wt/wt% PEG ATPS solution, confirmed that a wall-like interface formed between and separated these two phases completely.

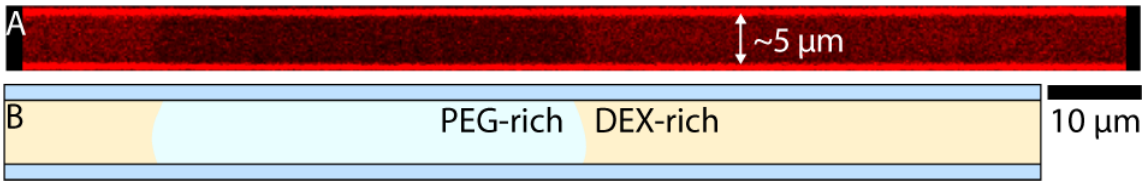

Figure 5.4: Configuration of the observation cell. A) Confocal image of the sandwich cell with labeled dextran and B) schematic image of the cell. The dark region of Panel A is the PEG-rich phase, and the red region represents the Alexa Fluor 647-labeled DEX-rich phase. The cell thickness is $\sim$ 5μm, and the 10-μm scale bar only applies to the lateral direction.

Motility suppression of *B. subtilis*

For the non-motile controls, the *B. subtilis* suspensions were incubated at the 65°C for 10 minutes.

5.5.2 Measuring the Partitioning Ratio

Observation

The samples were observed using an inverted phase-contrast microscope (BX53-P; Olympus) at room temperature (23°C). Image stacks, spanning more than 20 hours, were captured at the rate of 1 frame per second using a 20× dry objective and a CCD camera (INFINITY5-3M; Lumenera). Illumination was provided by an LED lamp (U-LEDPS; Olympus, the illumination light was adjusted to be 550nm by a filter, 43IF550-W45; Olympus).

Methods and Result

We chose a domain of the PEG-rich phase enclosed by the DEX-rich phase within the image stacks and adjusted this PEG-rich island to be located at the center of the image, making the area of each phase the same as shown in Fig. 5.5. Then we counted the number of bacteria inside and outside of the PEG-rich domain as shown in Fig. 5.6A

until the partitioning ratio reached a steady-state as shown in Fig. 5.6B.

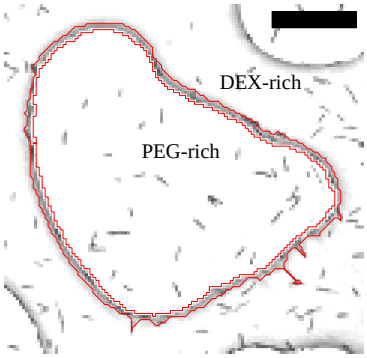

Figure 5.5: Experimental image of the sampled area. The PEG-rich island was adjusted to be at the center. The red lines highlights the interface. The number of bacteria inside and outside of the PEG-rich island was then counted. Scale bar = 50μm

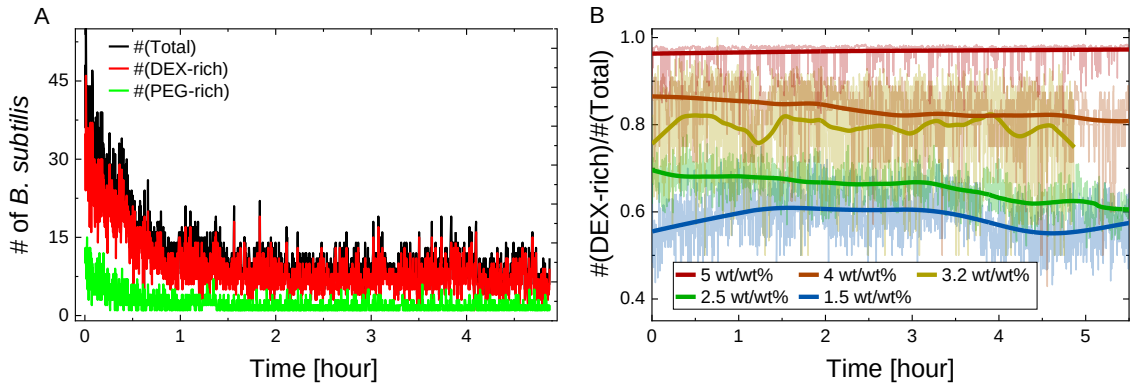

Figure 5.6: Change in the number and partitioning ratio of bacteria in sampled areas over time. (A) The number of bacteria inside(green) and outside(red) of the sampled PEG-domain and the total(black) are plotted. (B) Steady-state partitioning ratio, with each color indicating the concentration of dextran employed in each test. The thick solid lines after smoothing illustrate the partitioning trend over time. The raw data plotted here were used to calculate the values in Fig. 5.2

5.5.3 Attaching a Colloidal Bead to the Bacteria

We attached a spherical silica bead as a handle on the bacterium's surface to calibrate the force in the optical tweezers experiment. Grabbing the handle on the bacterium

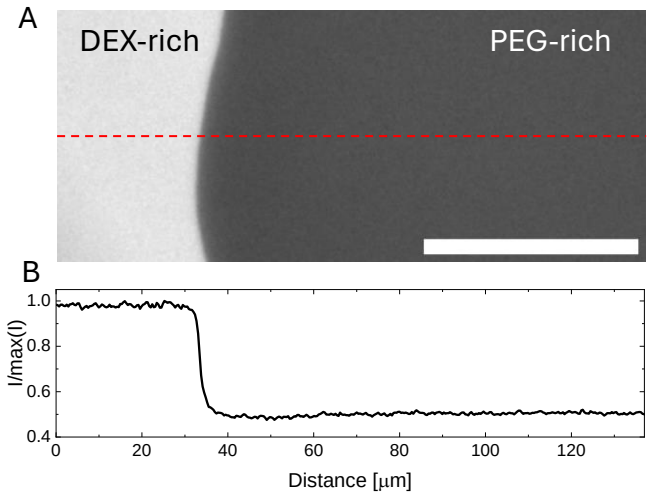

Figure 5.7: Fluorescence microscope image of ATPS and its intensity profile. (A) The phase-separated system and its fluorescence signal images were obtained from the solution containing 3.2 wt/wt% of DEX, 2.5 wt/wt%of PEG, and 0.0004 wt/wt% of DEX-FITC) The intensity profile of the red line, which corresponds with the dextran composition, is plotted in (B). Scale bar = 50 μm

rather than the bacterial body with the optical tweezers simplifies the force calculation by reducing any complexity arising from an anisotropic morphology of the bacterium, as well as changes in the refractive index while crossing the PEG-dextran interface.

Attaching a handle to the bacteria was achieved in two steps. Partially oxidizing the bacterial surface is the first. The second is a biotinylation process involving hydrazide Biotin (Thermo Fisher Scientific). During the first step, the surfaces of the bacteria are partially oxidized and treated by adding 20 μL of aqueous 100 mM $NaIO_4$ (Sigma-Aldrich) solution into 100 μL of washed bacteria solution. After 30 min at room temperature, 22°C, the bacteria were pelleted (6k RCF for 1min) and washed 5 times with deionized water. Then the sedimented pellet is dispersed into 50 μL of deionized water for the biotinylation step. To chemically bind biotin to the bacterial surface, aqueous solutions of 10 μL of 100 mM aniline(Sigma-Aldrich) and 10 μL of 100 mM hydrazide biotin were added to the partially oxidized bacteria solution (50 μL) to make a final concentration of 14.3 mM of aniline and 14.3 mM of a binding material. This was incubated at 36℃

for 2 hours after which the oxidation reaction was quenched by adding 1 mL of deionized water. The biotinylated bacterial cells were collected into 50 μL of deionized water after five rounds of pelleting (6k RCF for 1 min) and washing with deionized water.

Streptavidin-functionalized silica beads (SA-bead, 3-3.9 μm, Spherotech) were added to the biotinylated bacteria suspension. For this, 5 μL of biotinylated bacterial cells and 5 μL of 0.5 wt/wt% SA-bead solution in deionized water were mixed with 200 μL of the ATPS solution. The biotin present on the bacterial surface binds to the streptavidin on the particle.

5.5.4 Optical tweezers measurement

Observation and method

An inverted microscope(TI-2 Eclipse, Nikon) with 100x objective lens (CFI Plan Apo lambda) was used. The optical trapping was controlled by Tweez300 software (Aresis). In this study, the laser beam was focused on the spherical handle attached to the bacterial surface and dragged the bacterium across the interface. The dragging velocity was maintained at a value of 0.5-2 μm/s, which is slow enough to neglect the viscous drag ($6\pi\eta r v$: $0.10 \sim 0.41$pN where $r = 1\mu$m, $\eta = 11\text{mPa}\cdot\text{s}$ and $v = 0.5 \sim 2\mu$m/s) when compared to the force applied by the interface ($\gg$ 1pN). Namely, as the laser beam moved, the sphere remained at the laser beam's focus, and any displacement observed should result from external forces, specifically those from the interface. As the bacterium moved, we tracked the spherical handle and compared its position against the position of the laser focus, which moved at a constant speed. The difference between two positions is defined as $\mathrm{d}x$ where the force applied on the particle (F) is defined as $F = \kappa_\mathrm{t} \cdot \mathrm{d}x$, with trap stiffness, κ_t, is listed in Table. 5.1.

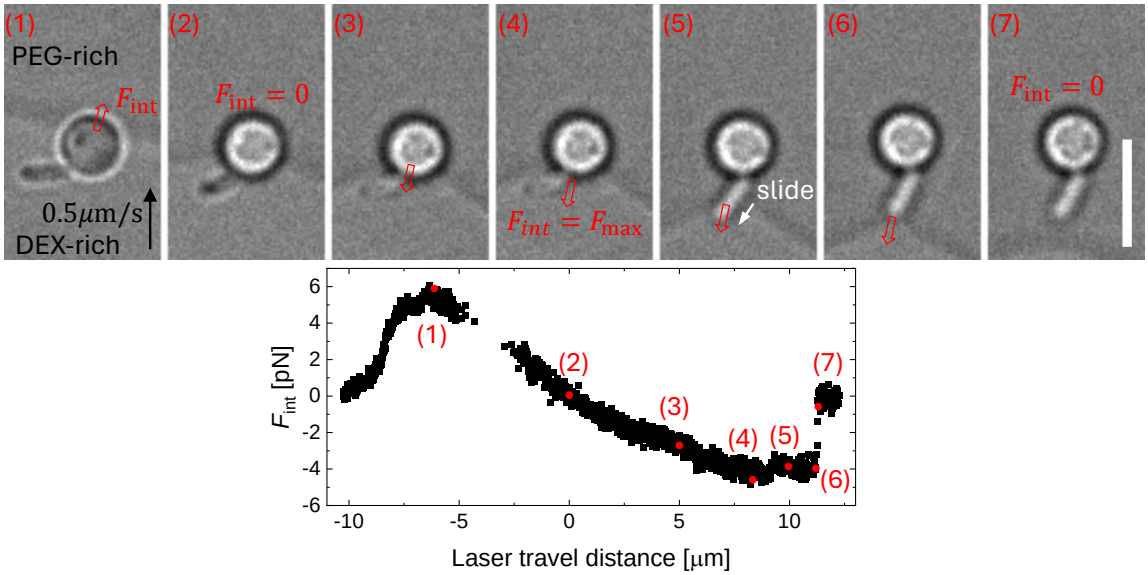

Figure 5.8: Optical tweezers experiment snapshots and calibrated force curve. The images are snapshots of the bacteria assembly crossing the PEG-dextran interface from the DEX-rich phase. The force applied on the assembly as measured by the optical tweezers is shown at the bottom. (1) Because of the interaction between the silica bead and the interface, the assembly is pulled forward along a laser traveling direction (0.5 μm/s, black arrow, same for all snapshots). The force applied by the interface on the assembly, F_{int}, is represented as a red arrow. (2) At the point where $F_{\text{int}} = 0$, the interaction between the bacterial body and the interface begins. (3) F_{int} increases, but its direction is opposite to the traveling direction. (4) F_{int} reaches its maximum magnitude, F_{max}. (5) The interface begins sliding (white arrow) over the bacterial body. (6) Finally, the interface releases the assembly. (7) F_{int} rapidly approaches 0, as the assembly enters the PEG-rich phase completely. Scale bar = 5 μm

5.5.5 Determining Trap Stiffness

The trap stiffness (κ_{t}) for the force measurement was determined from the analysis of a Brownian particle trapped with different laser powers. Because of the parabolic shape of the potential in the vicinity of the trapping focus, the particle's displacement from the laser focus follows a Gaussian probability distribution, represented as $P(dr) = \frac{1}{\sigma\sqrt{2\pi}} e^{-\frac{1}{2}\left(\frac{dr}{\sigma}\right)^2}$, where dr represents the displacement from the focus and σ is the standard deviation. The exponent in this expression corresponds to the dimensionless trapping energy, given by $\frac{E_{\text{trap}}}{k_{\text{B}}T} = -\frac{1}{2}\frac{\kappa_t dr^2}{k_{\text{B}}T}$, where k_{B} is the Boltzmann constant, and T is the

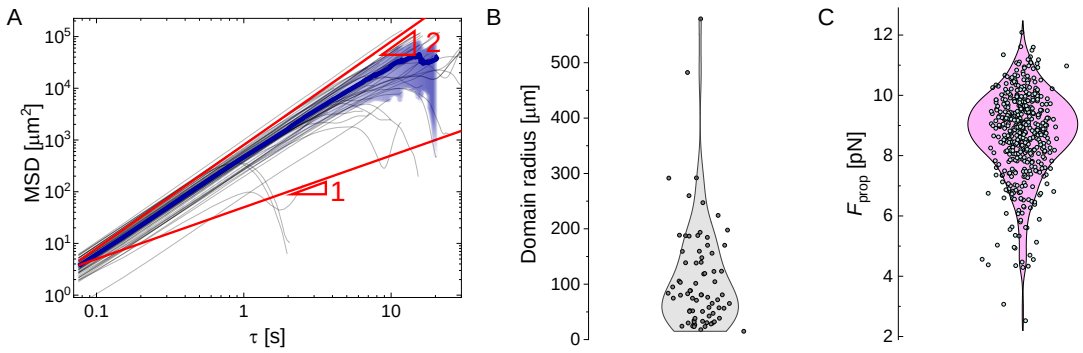

Figure 5.9: Experimental data of *B. subtilis* and the sample area. (A) The mean square displacement of *B.subtilis* in ATPS (where dextran concentration is 3.2wt/wt%). The navy line indicates the averaged MSD with the standard deviation plotted as a shadow. Two red lines are references slopes of 1 and 2. The background lines are the raw data obtained with individual *B. subtilis* cells. (B) Radius of the sampled PEG-rich domain. The area of the domain was estimated and, assumed to be circular, used to calculate the average radius. (C) Propulsion force of *B. subtilis* obtained by multiplying its speed with the drag coefficient of a prolate ellipsoid (the body length and the diameter of the bacterium's body were considered as the major and minor axes, respectively) in the DEX-rich phase (from ATPS prepared with 3.2 wt/wt% dextran).

temperature of the system. Thus, experimental measurement of σ^2 can determine $\kappa_t = \frac{k_B T}{\sigma^2}$.

Trap stiffnesses were measured with more than five different laser powers in the range 2 - 15% of the maximum laser power. Then, a linear regression line depending on laser powers can estimate the trap stiffness at an experimental power range of 10-80% of the maximum laser power using extrapolation.

Dextran concentration [wt/wt%]	1.5	2.5	3.2	4	5	8
Slope [pN/μm/% of P_{max}]	8.78	9.82	9.57	8.86	6.91	8.08

Table 5.1: Slope from the linear regression relating the trap stiffness to the percentage of the maximum laser power.

5.5.6 Model Development

The probability distribution of an active Brownian rod confined in 2-dimensions follows the Smoluchowski equation:

$$\frac{\partial P}{\partial t} + \nabla \cdot \left[\frac{P}{\zeta} \left(\mathbf{F}_{\text{prop}} + \mathbf{F}_{\text{B}} + \mathbf{F}_{\text{ext}} \right) \right] + \frac{\partial}{\partial \theta} \left[\frac{P}{\zeta_R} \left(L_{\text{B}} + L_{\text{ext}} \right) \right] = 0 \tag{5.3}$$

where $P(\mathbf{r}, \theta, t)$ is the normalized probability density in the periodic unit cell, ζ is the translational drag coefficient (which is approximated as a constant independent of particle orientation) and ζ_R is the rotational drag coefficient. $\mathbf{F}_{\text{prop}} = F_{\text{prop}}[\cos(\theta), \sin(\theta)]^T$, $\mathbf{F_B} = -k_{\text{B}}T\nabla \ln P$, and $\mathbf{F}_{\text{ext}}$ are respectively the active, Brownian, and external forces acting upon the body, and $L_B = -k_{\text{B}}T\frac{\partial \ln P}{\partial \theta}$ and L_{ext} are the Brownian and external torques.

Ignoring gradients in the y direction, the Smoluchowski equation simplifies to:

$$\frac{\partial P}{\partial t} + \frac{\partial}{\partial x} \left[\frac{P}{\zeta} \left(F_{\text{prop}} \cos(\theta) - k_{\text{B}}T \frac{\partial \ln(P)}{\partial x} - \frac{\partial V}{\partial x} \right) \right] + \frac{\partial}{\partial \theta} \left[P \left(-\frac{1}{\tau_R} \frac{\partial \ln(P)}{\partial \theta} - \frac{1}{\zeta_R} \frac{\partial V}{\partial \theta} \right) \right] = 0, \tag{5.4}$$

where τ_R is the reorientation time.

To study the partitioning between two phases, we model a repeating lamellar phase using a 1-D periodic potential of strength A and wavelength L: $\phi(x) = -A \tanh\left[\frac{L}{2\pi\delta} \cos\left(\frac{2\pi x}{L}\right)\right]$ with $\delta \ll L$ to approximate a square wave. For a finite-sized body described by density $\rho(\mathbf{s})$, the potential energy V of the body is given by the convolution $V(\mathbf{r}, \theta) = \int \phi(\mathbf{r} - \mathbf{s})\rho(\mathbf{s}) d\mathbf{s}$. We compute the convolution as a product in Fourier space

$$\hat{V}_n(\theta) = \hat{\phi}_n \hat{\rho}_n(\theta). \tag{5.5}$$

The n-th Fourier coefficient of the line density $\hat{\rho}_n$ can be derived analytically [22], allowing us to determine an expression for the center of mass potential directly.

$$V(x, \theta) = \sum_n \hat{\phi}_n e^{i2\pi k_n x} \text{sinc}\left(\pi \ell_{\text{bact}} k_n \cos(\theta)\right). \tag{5.6}$$

The wavevector is defined as $k_n = \frac{n}{L_x}$, and the bacteria length is ℓ_{bact}. This method converges rapidly for periodic potentials with a low-wavenumber power spectrum. The $\text{sinc}(\pi \ell_{\text{bact}} k_n \cos(\theta))$ term comes from the Fourier transform of the segment density for a rod and couples the orientation of the bacterium to the potential energy. We solve Eq. 5.4 at steady state using spectral methods implemented in the spectral PDE solver Dedalus [24].

Bibliography

[1] J. Cheon, K. H. Choi, K. J. Modica, R. J. Mitchell, S. C. Takatori, and J. Jeong, *Motility modulates the partitioning of bacteria in aqueous two-phase systems*, arXiv:2405.0899.

[2] T. Yoshizawa, R.-S. Nozawa, T. Z. Jia, T. Saio, and E. Mori, *Biological phase separation: cell biology meets biophysics*, *Biophysical reviews* **12** (2020), no. 2 519–539.

[3] M. Iqbal, Y. Tao, S. Xie, Y. Zhu, D. Chen, X. Wang, L. Huang, D. Peng, A. Sattar, M. A. B. Shabbir, *et. al.*, *Aqueous two-phase system (atps): an overview and advances in its applications*, *Biological procedures online* **18** (2016) 1–18.

[4] M. Dwidar, B. M. Leung, T. Yaguchi, S. Takayama, and R. J. Mitchell, *Patterning bacterial communities on epithelial cells*, *PLoS One* **8** (2013), no. 6 e67165.

[5] P. Åke Albertsson, *Partition of cell particles and macromolecules in polymer two-phase systems*, *Advances in Protein Chemistry* **24** (1970) 309–341.

[6] G. D. Baird, P. Åke Albertsson, and B. v. Hofsten, *Separation of bacteria by counter-current distribution*, *Nature* **192** (1961), no. 1 236–239.

[7] B. Hofsten, *Partition of escherichia coli in an aqueous polymer two-phase system*, *Experimental Cell Research* **41** (1966), no. 1 117–123.

[8] Q. Ma, Y. Song, W. Sun, J. Cao, H. Yuan, X. Wang, Y. Sun, and H. C. Shum, *Cell-inspired all-aqueous microfluidics: from intracellular liquid–liquid phase separation toward advanced biomaterials*, *Advanced Science* **7** (2020), no. 7 1903359.

[9] A. J. Huang, A. N. Clarke, N. Jafari, and B. M. Leung, *Characterization of patterned microbial growth dynamics in aqueous two-phase polymer scaffolds*, *ACS Biomaterials Science & Engineering* **7** (2021), no. 12 5506–5514.

[10] H. Sakuta, T. Fujimoto, Y. Yamana, Y. Hoda, K. Tsumoto, and K. Yoshikawa, *Aqueous/aqueous micro phase separation: construction of an artificial model of cellular assembly*, *Frontiers in Chemistry* **7** (2019) 44.

[11] C. Shibata, K. Iwashita, and K. Shiraki, *Salt-containing aqueous two-phase system shows predictable partition of proteins with surface amino acids residues*, *International journal of biological macromolecules* **133** (2019) 1182–1186.

[12] J. Kim, H. Shin, J. Kim, J. Kim, and J. Park, *Isolation of high-purity extracellular vesicles by extracting proteins using aqueous two-phase system*, *PloS one* **10** (2015), no. 6 e0129760.

[13] W. Cui, C. Xia, S. Xu, X. Ye, Y. Wu, S. Cheng, R. Zhang, C. Zhang, and Z. Miao, *Water-in-water emulsions stabilized by self-assembled chitosan colloidal particles*, *Carbohydrate Polymers* **303** (2023) 120466.

[14] C. K. Byun, M. Kim, and D. Kim, *Modulating the partitioning of microparticles in a polyethylene glycol (peg)-dextran (dex) aqueous biphasic system by surface modification*, *Coatings* **8** (2018), no. 3 85.

[15] S. Singh and H. Tavana, *Collagen partition in polymeric aqueous two-phase systems for tissue engineering*, *Frontiers in Chemistry* **6** (2018) 379.

[16] M. Mastiani, N. Firoozi, N. Petrozzi, S. Seo, and M. Kim, *Polymer-salt aqueous two-phase system (atps) micro-droplets for cell encapsulation*, *Scientific Reports* **9** (2019), no. 1 15561.

[17] M. E. Cates and J. Tailleur, *Motility-induced phase separation*, *Annual Review of Condensed Matter Physics* **6** (2015), no. 1 219–244.

[18] M. N. Van Der Linden, L. C. Alexander, D. G. Aarts, and O. Dauchot, *Interrupted motility induced phase separation in aligning active colloids*, *Physical review letters* **123** (2019), no. 9 098001.

[19] C. B. Caporusso, P. Digregorio, D. Levis, L. F. Cugliandolo, and G. Gonnella, *Motility-induced microphase and macrophase separation in a two-dimensional active brownian particle system*, *Physical Review Letters* **125** (2020), no. 17 178004.

[20] L. F. Garrity and G. W. Ordal, *Chemotaxis in bacillus subtilis: How bacteria monitor environmental signals*, *Pharmacology & Therapeutics* **68** (1995), no. 1 87–104.

[21] M. J. Tindall, P. K. Maini, S. L. Porter, and J. P. Armitage, *Overview of mathematical approaches used to model bacterial chemotaxis ii: bacterial populations*, *Bulletin of mathematical biology* **70** (2008) 1570–1607.

[22] K. J. Modica and S. C. Takatori, *Soft confinement of self-propelled rods: simulation and theory*, *Soft Matter* **20** (2024) 2331–2337.

[23] A. Baskaran and M. C. Marchetti, *Hydrodynamics of self-propelled hard rods*, *Phys. Rev. E* **77** (1, 2008) 011920.

[24] K. J. Burns, G. M. Vasil, J. S. Oishi, D. Lecoanet, and B. P. Brown, *Dedalus: A flexible framework for numerical simulations with spectral methods*, *Physical Review Research* **2** (4, 2020) 023068, [arXiv:1905.1038].

Chapter 6

Surface Topography Controls Nematic Swarms of Active Filaments

Surface-bound molecular motors can drive the collective motion of cytoskeletal filaments in the form of nematic bands and polar flocks in reconstituted gliding assays. Although these "swarming transitions" are an emergent property of active filament collisions, they can be controlled and guided by tuning the surface chemistry or topography of the substrate. To date, the impact of surface topography on collective motion in active nematics is only partially understood, with most experimental studies focusing on the escape of a single filament from etched channels. Since the late 1990s, significant progress has been made to utilize the nonequilibrium properties of active filaments and create a range of functional nanodevices relevant to biosensing and parallel computation; however, the complexity of these swarming transitions presents a challenge when attempting to increase filament surface concentrations. In this chapter, we etch shallow, linear trenches into glass substrates to induce the formation of swarming nematic bands and investigate the mechanisms by which surface topography regulates the two-dimensional (2D) collective motion of driven filamentous actin (F-actin). We demonstrate that nematic swarms only appear at intermediate trench spacings, and vanish if the trenches are made too narrow, wide, or tortuous. To rationalize these results, we simulate the F-actin as self-propelled, semi-flexible chains subject to a soft, spatially modulated potential that encodes the energetic cost of bending a filament along the edge of a trench. We hypothesize that an individual filament will feel a penalty when its projected end-to-end distance is smaller than the trench spacing ("bending and turning"). However, chains that span the channel width glide above the trenches in a force- and torque-free manner ("crowd-surfing"). Our simulations demonstrate that collections of filaments form nematic bands only at intermediate trench spacings, consistent with our experimental findings.

This chapter includes content from our previously published article:

[1] J.M. Barakat (equal contribution), K.J. Modica (equal contribution), L. Lu, S. Anujarerat, K.H. Choi, and S.C. Takatori, *Surface topography induces and orients ne-*

matic swarms of active filaments: Considerations for lab-on-a-chip devices, *ACS Applied Nano Materials* **7** (5, 2024), no. 10 12142-12152. JMB, KJM, and SCT conceived of the study; all authors designed research; JMB, LL, SA, KHC, and SCT performed experiments; KJM performed simulations; JMB, KJM, and SCT supervised the study and wrote the paper.

6.1 Introduction

Filamentous active matter, including filamentous actin (F-actin) and microtubules, are essential components of the cytoskeleton [2, 3]. The seminal work by Kron and Spudich established the F-actin gliding assay for visualizing single filaments driven by surface-bound myosin motors [4]. Active filaments exhibit collective dynamics that hold promise for the development of miniaturized, multifunctional lab-on-a-chip (LOC) devices. These devices could potentially utilize orchestrated groups of filaments for tasks such as analyte sensing, parallel computation, and targeted cargo delivery [5, 6]. While significant research efforts have focused on exploiting individual filaments in nanodevices, a growing area of interest lies in harnessing the emergent properties that arise from collective filament behavior. Researchers have already utilized the gliding assay to demonstrate the emergence of polar flocks and nematic swarms in collections of F-actin at moderate surface densities [7–11]. Theory and agent-based simulation have demonstrated that the emergence of these "swarming transitions" are determined by the symmetry of the interaction between colliding filaments [7, 9, 12]. If the pairwise collision of two filaments has nematic symmetry, the system will form nematic bands at high density; however, if the pairwise collision preferentially aligns the filaments to point the same direction, the system can form polar flocks. While experiments have shown the presence of both

nematic swarms and polar flocks, excluded-volume interactions alone only exhibit nematic symmetry upon the inelastic collision of two filaments. While the mechanics of the isotropic to polar or nematic transition is well understood for individual filaments, controlling the onset and evolution of filamentous swarms and flocks remains challenging, as these structures are inherently nonequilibrium and localized in space and time [13, 14]. Furthermore, the collective patterns observed in dry active systems, like gliding F-actin, showed a density-dependent polar transition, whereas other active nematics in wet systems exhibited dynamics driven by fluid-mediated hydrodynamic interactions [15, 16].

Researchers have proposed different methods to control the collective behavior of two-dimensional (2D) active matter [17]. Strategies include light-activated force generation [18–20], thermotropic liquid crystals [21–23], boundary confinement [24–26], surface chemistry patterning [27–31], and surface topography [32–42]. The latter has been shown to direct the motion of individual filaments in dilute systems of kinesin-driven microtubules [32–35] and myosin-driven F-actin [37–42]. By comparison, relatively few experimental studies have examined the effect of surface topography on collections of filaments at high surface densities [16, 43, 44].

Theory and simulation have demonstrated various methods to control swarming transitions in 2D active nematics, including boundary effects [13, 45–50]. In the presence of hydrodynamic interactions, active nematics confined between two parallel walls undergoes a transition between active turbulence, an ordered vortex lattice with dynamically structured disclinations, and coherent flow when the channel spacing and active stress decrease relative to the system's effective Frank elastic constant [51]. Similar results have been found for active nematics in a disk and annulus, with the boundary curvature allowing circulating and corotating states [52, 53]. The behavior of these wet systems are characterized by the presence and motion of topological defects in the director field.

In dry systems, it remains unclear how confinement and surface topography influence the order-disorder transitions between isotropic motion, polar flocks, and nematic swarms in *collections* of filaments, precluding the possibility of precise control.

In this chapter, we study the effect of surface topography on collections of dry active nematics. We manipulate surface topography by introducing periodic, shallow trenches in myosin-coated glass substrates to trigger the formation of nematic swarms within F-actin systems. These trenches are shallow enough that the F-actin is able to bend out of plane and escape the trenches to glide along the surrounding hills or to reenter the trenches after gliding on the hills.

In low-density systems, we find that individual F-actin exhibit enrichment along the trench boundaries, consistent with previous studies [37–42]. At higher F-actin densities, we observe the development of swarming nematic bands characterized by spatially-modulated density and nematic order along the channels. Notably, the swarming nematic bands form only at intermediate trench spacing, and the nematic order is non-monotonic with channel spacing. Narrow trenches suppress the formation of swarms altogether, whereas wide trenches result in uncorrelated collective motion. Similar suppression is observed for tortuous trenches compared to linear ones. Interestingly, for intermediate channel spacing, swarms consistently manifest and align along the channels. These experimental findings suggest the existence of an optimal length scale for surface topography to effectively guide the collective motion of filaments.

To rationalize our experimental findings, we develop a computational model of 2D self-propelled filaments subject to bending forces and torques along periodic intervals in one direction. Filaments spanning more than one periodic cell are assumed to glide freely without bending, whereas collapsed filaments are forced to bend and turn. This model is then implemented in 2D Brownian dynamics simulations of a collection of self-propelled, mutually interacting filaments, which demonstrate significant nematic ordering

and swarming when the filament length is comparable to the periodic repeat distance. Our model and simulations are consistent with the experimental observation that the "optimal" trench spacing is comparable to the run length and persistence length of F-actin. Taken together, our experiments and simulations suggest that the relationship between surface topography and self-propulsion is strongly coupled, and that precise tuning of topographical surfaces is necessary to promote and direct swarming behavior in filamentous active matter.

6.2 Materials and Methods

6.2.1 Experimental Details of F-actin Gliding Assay on Microfabricated Etched Topographies

We microfabricated etched features on a 24 mm by 40 mm, 170 µm thickness borosilicate coverslip (Azer Scientific). We used the Heidelberg Maskless Aligner, a high-speed direct-write photolithography equipment that is available at the UCSB Nanofabrication Facility for rapid prototyping and high-throughput of etched patterns. We developed a photolithographic mask on the substrate with a specified pattern, followed by anisotropic plasma dry etching with CF_4/CHF_3 gases [54]. Using this technique, we created topographic patterns on the coverslip because the photoresist will mask select regions from dry etching [54]. Once the topographical substrates were created, we followed the existing methods for actin-gliding assays [7, 55]. We purified heavy meromyosin (HMM) motor proteins and globular actin monomers (G-actin) from rabbit skeletal muscle [56–58].

We coated the etched coverslip with a thin layer of trichloromethylsilane, and created an observation chamber on the coated substrate using a 5mm thick polydimethylsiloxane (PDMS, Sylgard 184, Dow) block with a 6mm hole. We deposited F-buffer containing

HMM into the observation chamber to allow the HMM to stick on the substrate. The F-buffer composition is 50mM Tris pH 7.5, 2mM $MgCl_2$, 0.2mM $CaCl_2$, 25mM KCl, 0.5mM adenosine 5'-triphosphate (ATP), and 1mM dithiothreitol (DTT). Separately, 10 µM G-actin and 1 µM phalloidin-647 (Alexa Fluor Plus 647 Phalloidin, Invitrogen) were added to F-buffer and incubated for 45 min. The F-actin suspension was pipetted into the observation cell at a desired density. We allowed the F-actin to sediment for 30 min and added ATP at a specified density, following previous actin-gliding assays [4, 7]. Activity persisted for at least 30 minutes after ATP addition. An ATP regeneration system was not necessary for our system.

All imaging was carried out on an inverted Nikon Ti2-Eclipse microscope (Nikon Instruments) using an oil-immersion objective (Plan Apochromat VC 100x, numerical aperture 1.4). Lumencor SpectraX Multi-Line LED Light Source was used for excitation (Lumencor, Inc). Fluorescent light was spectrally filtered with an emission filter (680/42; Semrock, IDEX Health and Science) and imaged on a Photometrics Prime 95 CMOS Camera (Teledyne Photometrics).

6.2.2 Brownian Dynamics Simulations of Active Filaments

An active filament is represented as a chain of 21 spherical particles of diameter σ connected by harmonic spring forces between adjacent pairs and bond-angle forces between connected triplets. The position $\boldsymbol{r}_{i,j}(t)$ of the jth particle on the ith chain is advanced via the Langevin equation,

$$\frac{d\boldsymbol{r}_{i,j}(t)}{dt} = \sqrt{\frac{2k_{\mathrm{B}}T}{\zeta}}\boldsymbol{\eta}_{i,j}(t) + \frac{1}{\zeta}\left(\boldsymbol{F}_{i,j}^{\mathrm{bond}} + \boldsymbol{F}_{i,j}^{\mathrm{angle}} + \boldsymbol{F}_{i,j}^{\mathrm{excl}} + \boldsymbol{F}_{i,j}^{\mathrm{ext}} + \boldsymbol{F}_{i,j}^{\mathrm{act}}\right), \tag{6.1}$$

where ζ is the particle drag coefficient and $\boldsymbol{\eta}_{i,j}$ is a white-noise source. In this model, each particle experiences forces due to bond pairs, angular triplets, excluded-volume interactions, external fields, and active propulsion, each of which is discussed further below.

The bond and angle forces, $\boldsymbol{F}_{i,j}^{\text{bond}}$ and $\boldsymbol{F}_{i,j}^{\text{angle}}$, between particles on the *same* chain are defined as follows. For two bonded particles separated by a distance r, a harmonic spring potential pulls them to an equilibrium separation equal to their diameter,

$$V_{\text{bond}}(r) = \tfrac{1}{2}k_{\text{bond}}(r-\sigma)^2. \tag{6.2}$$

Similarly for a group of three linearly bonded particles forming an angle θ, an angle potential pulls them into parallel alignment,

$$V_{\text{ang}}(\theta) = \tfrac{1}{2}k_{\text{ang}}(\theta-\pi)^2. \tag{6.3}$$

Here, k_{bond} and k_{ang} denote the Hookean spring stiffnesses for these potentials. To simulate semiflexible filaments, we choose a large bond stiffness, $k_{\text{bond}} = 50k_BT$, and an angle stiffness that gives a persistence length, L, equal to the contour length, $L_{\text{c}} = 21\sigma$, $k_{\text{ang}} = 21k_BT$. The bond and angle forces are then obtained from a virtual work argument,

$$\boldsymbol{F}_{i,j}^{\text{bond}} = -\nabla_{i,j}V_{\text{bond}}(\boldsymbol{r}_{i,j}), \qquad \boldsymbol{F}_{i,j}^{\text{ang}} = -\nabla_{i,j}V_{\text{ang}}(\boldsymbol{r}_{i,j}), \tag{6.4}$$

where $\nabla_{i,j}$ denotes the gradient with respect to the position of the jth particle on the ith chain.

Any two particles not directly bonded to each other interact with each other via the following soft excluded-volume interaction:

$$V_{\text{excl}}(r) = \begin{cases} \varepsilon\left[1+\cos\left(\dfrac{\pi r}{r_c}\right)\right], & \text{if } r \le r_c, \\ 0, & \text{if } r > r_c, \end{cases} \tag{6.5}$$

where $\varepsilon = 10k_BT$ is the energy-well depth and $r_c = 1.1\sigma$ is the interaction radius. The excluded-volume force is then computed via the gradient,

$$\boldsymbol{F}_{i,j}^{\text{excl}} = -\nabla_{i,j} V_{\text{excl}}(\boldsymbol{r}_{i,j}). \tag{6.6}$$

To simulate an externally imposed, soft confinement with periodic repeat distance $2H$, we use a continuous approximation of the square-wave potential,

$$V_{\text{ext}}(\boldsymbol{r}_{i,j}) = \begin{cases} 0, & \text{if the } j\text{th filament crosses} \\ & \text{two or more "edges,"} \\ -A \tanh\left[\dfrac{H}{\pi\sigma}\cos\left(\dfrac{\pi \boldsymbol{r}_{i,j}\cdot\boldsymbol{e}_x}{H}\right)\right], & \text{otherwise,} \end{cases} \tag{6.7}$$

where A is the potential amplitude. Here, an "edge" denotes an inflection point in the potential landscape where a "hill" meets a "valley." This external field is defined such that a filament crossing multiple edges feels no force or torque. The number of edges crossed, $N_{i,\text{cross}}$ by the ith chain with its tail at $x_{i,1}$ and head at $x_{i,N}$ is found via the following algorithm:

$$N_{i,\text{cross}} = \left|\text{floor}\left(\frac{x_{i,N}}{H} + \frac{1}{2}\right) - \text{floor}\left(\frac{x_{i,1}}{H} + \frac{1}{2}\right)\right| \tag{6.8}$$

The amplitude, A, of the external field is calibrated such that the work required for a filament to escape a trench is $2AL_{\text{c}}/\sigma = 42k_{\text{B}}T$. The associated force on the jth particle on the ith chain is

$$\boldsymbol{F}_{i,j}^{\text{ext}} = -\nabla_{i,j} V_{\text{ext}}(\boldsymbol{r}_{i,j}). \tag{6.9}$$

Finally, active propulsion is modeled by imposing a constant force, F_{act}, on each particle along the tangent of the filament contour [59],

$$\boldsymbol{F}_{i,j}^{\text{act}} = \begin{cases} F^{\text{act}} \dfrac{\boldsymbol{r}_{i,j+1} - \boldsymbol{r}_{i,j}}{\|\boldsymbol{r}_{i,j+1} - \boldsymbol{r}_{i,j}\|}, & j = 1, 2, \ldots, N-1, \\ F^{\text{act}} \dfrac{\boldsymbol{r}_{i,N} - \boldsymbol{r}_{i,N-1}}{\|\boldsymbol{r}_{i,N} - \boldsymbol{r}_{i,N-1}\|}, & j = N, \end{cases} \tag{6.10}$$

where $N = 21$ is the number of particles per chain. The strength of the active propulsion force is set to be one-half the value of the maximum external-potential force. Hence, a single particle on the chain will not easily overcome the energy barrier, but multiple particles directed together can push the chain out of a local potential well.

A system of filaments with number density ρ was initialized in a periodic box of width L_x and length L_y. The box width was determined from an integer multiple of the periodic repeat spacing of the external potential, $L_x = 2pH$. The periodicity, p, and number of filaments were adjusted such that the box width $L_x > 20L_c$ and the box length $L_y > 50L_c$, to avoid finite-size effects from the periodic boundary conditions.

After calibrating our parameters, we ran simulations to determine the impact of inter-filament interactions on ordering and alignment. All simulations were performed at number density $\rho = 3/L_c^2$. We calculated the density-weighted nematic order tensor, $\boldsymbol{Q}$, by finding the unit orientation vector $\boldsymbol{q}$ for all filaments at all timesteps (resulting in N_{samp} number of samples), forming a symmetric and traceless dyad, and then taking the ensemble average. The ensemble-averaged nematic order tensor was found for three independent simulations and the standard deviation of the average values were computed to find the error of the mean.

6.3 Results and Discussion

6.3.1 Surface Topography Directs the Motion of Individual Filaments and Dense Swarms

Figure 6.1A-B depicts our etched coverslips coated with molecular motors to direct the motion of F-actin in a gliding assay (for details, see Methods). The etched trenches have a fixed depth ≈ 200 nm, as verified by scanning electron microscopy (Fig. 6.1C), and

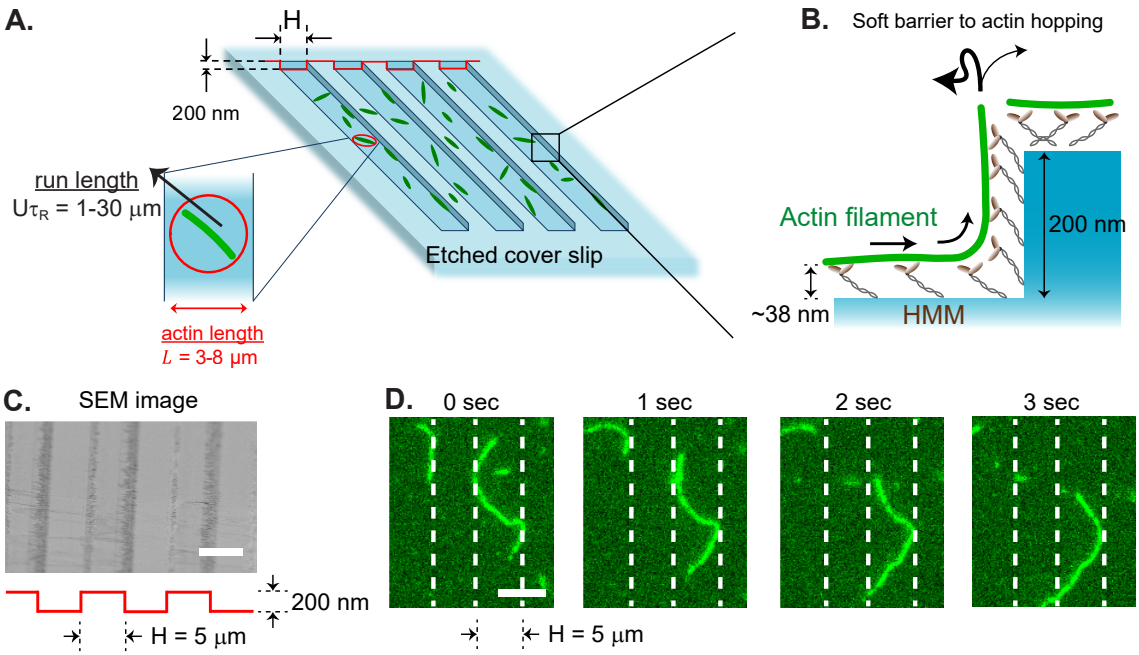

Figure 6.1: Etched surface topographies are used to control the motion and swarming transitions of filamentous actin (F-actin) propelled by surface-bound heavy meromyosin (HMM) motors. (A) Schematic of parallel trenches with shallow valleys and variable spacing, H. (B) Etched substrates of depth $\approx$ 200 nm impose a soft confinement for F-actin inside the trenches. (C) Scanning electron microscopy image of the etched substrates with parallel trenches (5 µm channels shown here). (D) Individual actin filaments bounce off the walls due to a soft confinement potential imposed by the trench edges. All scale bars are 5 µm.

a periodic repeat spacing, H, that can be controlled. Figure 6.1D depicts measurements for single filaments with trench spacing $H = 5$ µm. Upon activating the system via addition of ATP, we observed individual F-actin collide into the trench boundaries and reorient their motion within the confines of the trenches. Since F-actin glides at an average height of $\approx$ 38 nm above the substrate [60], we hypothesized that the filaments experience a soft barrier to bending at the sharp edge of the trench (Fig. 6.1B) similar to the confinement observed for kinesin-propelled microtubules in microfluidic channels with deep trenches [33–35]. The flexural modulus of phalloidin-stabilized F-actin [17] is $EI \approx 20\ k_{\mathrm{B}}T \cdot$µm and so the work to bend a filament segment into a quarter-arc of radius

≈ 200 nm is of order 50 $k_{\mathrm{B}}T$ [61]. Therefore, while thermal Brownian forces are unlikely to drive the filaments out of the trenches, active forces generated by the myosin motors can overcome the bending penalty posed by the trench edge.

At larger F-actin surface densities, we observed the spontaneous formation of swarming nematic bands along the trenches that repeated every periodic spacing (Fig. 6.2A; see Supplementary Movie 1 of [1]). These robust nematic bands spanned hundreds of micrometers and persisted over tens of minutes until ATP depletion. Filaments continuously enter and leave the bands while maintaining an enriched density within the trenches (line scan in Fig. 6.2B shows approximately four-fold enrichment). The nematic bands were similar in structure to those observed in F-actin gliding assays on planar substrates [7]; here, we demonstrated our ability to control the alignment of nematic filaments using surface topography.

To confirm the development of spatially modulated order within the system, we computed the intensity-weighted nematic order tensor [62],

$$\boldsymbol{Q}_I(\boldsymbol{r}) = I(\boldsymbol{r})[2\boldsymbol{n}(\boldsymbol{r})\boldsymbol{n}(\boldsymbol{r}) - \boldsymbol{I}], \tag{6.11}$$

as a function of position $\boldsymbol{r} = x\hat{\boldsymbol{e}}_x + y\hat{\boldsymbol{e}}_y$, where $I(\boldsymbol{r})$ is the normalized scalar intensity and $\boldsymbol{n}(\boldsymbol{r})$ is the unit director (Fig. 6.2B-C). The concentration of filaments is not uniform in space; we use the intensity as a proxy for actin density when sampling the F-actin nematic order. Contour plots of the yy tensor component (parallel to the trenches) confirm the formation of ordered, nematic bands within the trenches (Fig. 6.2D). The average degree of order for a particular experiment is quantified by the areal average of the order tensor,

$$\langle \boldsymbol{Q}_I \rangle = \frac{1}{A}\int_A \boldsymbol{Q}_I(\boldsymbol{r})\, d\boldsymbol{r}, \tag{6.12}$$

where $d\boldsymbol{r} = dx\, dy$ and A denotes the two-dimensional area in the field of view. Equation 6.12 is used to compare the degree of ordering across different experiments.

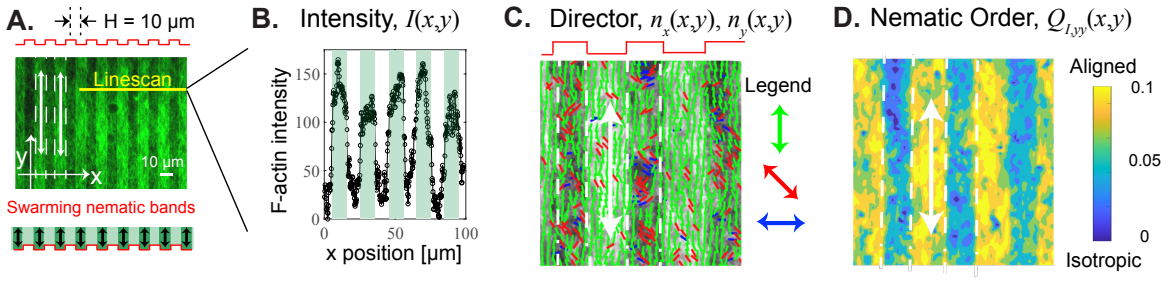

Figure 6.2: Parallel trenches induce and guide nematic bands of F-actin. (A) Image of gliding assay showing swarming nematic bands of F-actin moving up and down along the periodic parallel channels (outlined in white dashed lines). (B) Line scan of local intensity, $I(\boldsymbol{r})$ shows periodic, fourfold enrichment of F-actin. (C) The unit director field, $\boldsymbol{n}(\boldsymbol{r})$ is strongly aligned with the direction of the trenches. (D) Contours of the yy component of the nematic order tensor, $\boldsymbol{Q}_I(\boldsymbol{r})$, as defined by Eq. 6.11.

6.3.2 Two-dimensional (2D) model of topography-directed active filaments

In order to develop a mechanistic understanding of topography-driven spatial enrichment and nematic ordering of active filaments, we model the topographical surface as a spatially-modulated potential in the x-y plane. This 2D representation offers favorable computational efficiency when applied to a large number of filaments. Our potential model, illustrated in Fig. 6.3, derives from the argument that filaments experience local bending forces and torques near the edge of a trench. Under the action of a square-wave potential with periodicity in the x-direction, a single filament is forced towards the potential minima and torqued to align along the y-direction (Fig. 6.3A). Groups of mutually exclusive filaments under such forces and torques will coordinate their motion to run transverse to the potential gradients. We call this type of behavior "bending and turning."

However, when an active filament is longer than the periodic spacing, a single filament has to sharply bend at multiple locations, which is energetically unfavorable. In this

scenario, we expect the filament to detach from the motors coating the depressed regions of the topographical surface rather than bend at multiple points. Active propulsion is then solely generated by motors on the elevated surfaces. This latter type of behavior is called "crowd-surfing," since the filament glides above the trenches without bending. In order to model this behavior, we switch off the potential whenever the end-to-end distance of a filament spans multiple periodic cells (Fig. 6.3A). This phenomenological rule is inspired by experimental observations of F-actin that predominantly glide in a straight path on the tops of the trenches for the small-wavelength trenches, unaffected by the undulations of the substrate.

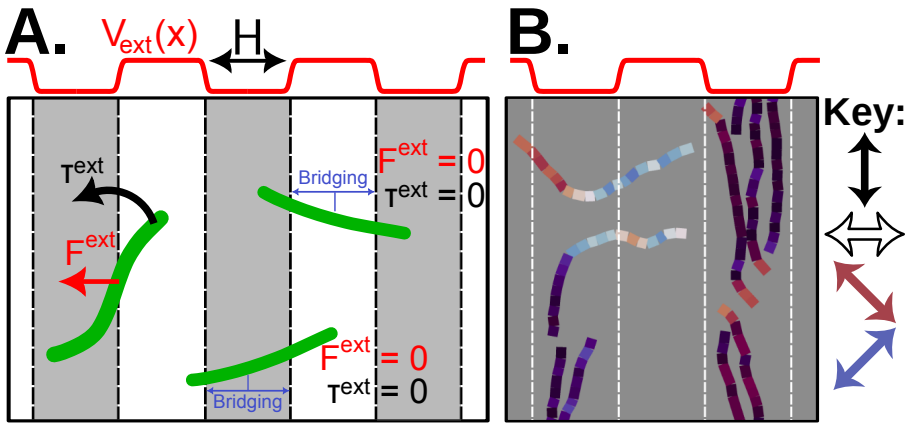

Figure 6.3: Actin gliding captured in simulations using a 2D potential model. (A) Schematic demonstrating our model of topographical confinement using an external field. Active filaments are confined and turned by the external field only if the actin is not bridging the channel. If a filament bridges between two hills or valleys (represented as potential energy minima and maxima), the filament ignores the energy field and glides across channels under zero force and torque, $\boldsymbol{F}^{\text{ext}} = \mathbf{0}$ and $\mathsf{T}^{\text{ext}} = 0$. (B) Simulation snapshot of active filaments moving under the influence of the potential field. Filaments are colored by their local nematic order along the contour.

We implemented this potential model in 2D Brownian Dynamics (BD) simulations of semi-flexible filaments of persistence length $L = 10$ µm and contour length $L_c = 10$ µm subject to thermal, active, and potential-driven forces as well as pairwise excluded-body forces. Details of our simulation methodology can be found in the Methods section; a

sample simulation is shown in Fig. 6.3B. Simulation parameters were first calibrated for a dilute system, for which the excluded-body forces are disabled, before increasing the surface concentration to determine the impact of inter-filament interactions on ordering and alignment. To compare against our experimental results on a qualitative basis, we calculated the ensemble-averaged, density-weighted nematic order tensor,

$$\langle \boldsymbol{Q} \rangle = \frac{1}{N_{\text{samp}}} \sum_{i=1}^{N_{\text{samp}}} [2\boldsymbol{q}(i)\boldsymbol{q}(i) - \boldsymbol{I}] \tag{6.13}$$

where $\boldsymbol{q}(i)$ is unit orientation vector (directed along the propulsion axis) for the ith sampled filament at a particular timestep, N_{samp} is the total number of samples (filaments and timesteps), and $\langle \cdots \rangle$ denotes an ensemble average over all simulated trajectories. The latter should not be confused with the areal average in Eq. 6.12, which is intended for the limited sampling window observed in our experiments.

6.3.3 Swarm Suppression by Varying the Periodic Repeat Spacing

In our experiments, we varied the trench spacing across $H = 5$ - 40 µm while keeping the F-actin surface density and ATP concentration fixed (Fig. 6.4). Interestingly, we found that the large ($H = 40$ µm) and small ($H = 5$ µm) trench spacings do not produce nematic bands (see Supplementary Movies 2 and 3 of [1] for videoes of $H = 5$ µm and $H = 40$ µm, respectively). For small spacing, $H = 5$ µm, we never observed nematic bands in any of our experiments (more than 30 replicates). For large spacing, $H = 40$ µm, we occasionally observed nematic bands that are similar to the bulk swarms in unconfined systems [7, 13], but these bulk swarms were not correlated with the periodic trenches. In contrast, nematic bands formed consistently in the direction of the channels over intermediate trench spacings of $H = 10$ - 20 µm (Fig. 6.4C and D). These intermediate

spacings are similar to the characteristic length scale associated with the actin swarms observed previously on planar surfaces [7]. Taken together, our data suggest that the nematic bands appear in our periodic channels when the spacing, H, is comparable to the orientation screening length of the swarms.

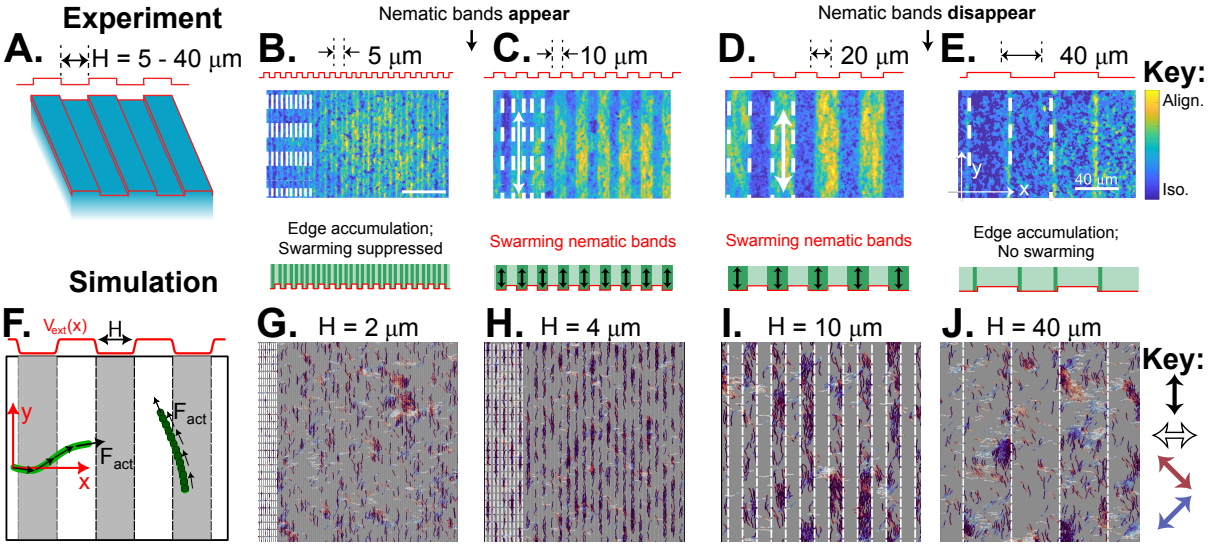

Figure 6.4: Nematic bands appear at intermediate spacing, H, but not at large and small spacing. (A) Schematic of our experiments on etched coverslips. (B - D) Contours of the yy component of the nematic order tensor, $\boldsymbol{Q}_I(\boldsymbol{r})$. All experiments were conducted at the same ATP concentration, 0.1 mM. (B) At small spacing, $H = 5$ μm, we do not observe swarming nematic bands. (C, D) At intermediate spacing, $H = 10 - 20$ μm, nematic bands form along the channels with significant actin enrichment. (E) At large spacing, $H = 40$ μm, we see an isotropic distribution of actin filaments, with a small accumulation at the periodic edges. (F) Schematic of the simulation box with a periodically modulated potential. (G-J) BD simulations varying the potential width corroborate our experimental observations.

Using our 2D model, we also performed BD simulations of active filaments in a potential field of varying periodic repeat spacing H (Fig. 6.4F-J and Supplmentary Movies 4-6). Similar to our experiments, our simulations indicated that swarms preferentially align along the potential wells at an intermediate spacing, $H = 3$ - 12 μm. The physical mechanism behind this preferential alignment at intermediate spacing is linked to a energetic competition between filament bending and adhesion to the substrate, as discussed

previously.

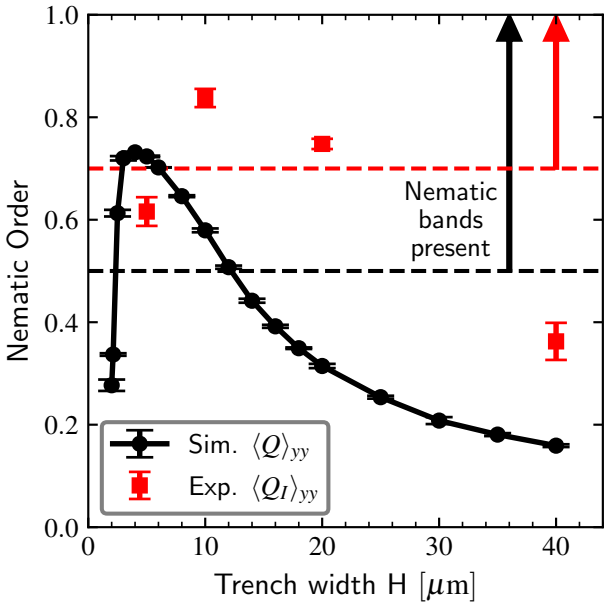

Figure 6.5: Experiments and simulations indicate filament alignment is maximized at intermediate trench spacing. Simulated filaments have contour length $L_c = 10$ µm to roughly match the mean experimental actin length. (A) The degree of alignment of filaments with the channel director is plotted as a function of trench width. Black circles are the density-weighted nematic order measured from simulations, $\langle \boldsymbol{Q} \rangle_{yy}$. Red squares are the intensity-weighted average nematic order from the experiments, $\langle \boldsymbol{Q}_I \rangle_{yy}$. These metrics quantify the appearance of swarming nematic bands over an intermediate trench spacing, H^*. The simulations underpredict ($H^*_{\text{sim}} \approx 4$ µm) the value of H^* observed in the experiments ($H^*_{\text{exp}} \approx 10$ µm). Dashed lines in both figures are markers of visual observations of the appearance of nematic bands in simulation (black) and experiment (red).

To quantify the onset of swarming, we computed the average nematic order tensors $\langle \boldsymbol{Q}_I \rangle$ and $\langle \boldsymbol{Q} \rangle$ from the experiments and simulations, respectively [cf. Eqs. 6.12 and 6.13]. Since these tensors are weighted differently (by intensity in the experiments, by density in the simulations), the comparison between the two is intended to be qualitative rather than quantitative. The yy components of each are co-plotted in Fig. 6.5 as a function of the periodic repeat spacing (or trench width), H. Both the experiments and simulations indicate that order is maximized at an intermediate trench spacing, H^*. At small trench

spacings ($H < H^*$), filaments align along boundaries but do not form collective nematic bands, resulting in low nematic order. As the spacing is increased ($H \approx H^*$), ordered nematic bands appear in both simulation and experiment. Actin propels along a director parallel to the trenches in bundles made from a large number of individual filaments. At large trench spacing ($H > H^*$), the boundaries are far enough apart that orientational correlations decay by the time the filament reaches the center of the trenches, resulting in loss of global order.

The simulations predict a value $H^* \approx 4$ µm that is smaller than the experimental observation, ≈ 10 µm, which we believe could be caused by polydispersity in the experimental actin contour lengths. Nevertheless, the qualitative agreement between the experiments and simulations indicate that the microscopic rule proposed in our simple model can explain the non-monotonic dependence of nematic order with trench spacing. To recapitulate, the basic idea of this rule is that filaments will only bend and turn to align with the edge of a trench only if their length does not span the entire trench width. A filament crossing one edge will start to turn until it reaches the second edge; this implies that most filaments will cross the second edge at an angle relative to the x-axis, provided their run length is sufficiently small. This explains why the optimal trench width for alignment as predicted in the simulation (≈ 4 µm) is smaller than the filament length (≈ 10 µm). More accurate predictions would likely require a (much more computationally intensive) 3D simulation of filament motion, explicitly resolving the spatial variation in depth (i.e., in the z-direction).

As discussed previously, we estimate the bending penalty for actin to be $\approx 50 k_{\mathrm{B}}T$ at each of the trench corners. A filament that spans multiple channels can avoid this bending penalty by detaching from N_{bound} bound HMM motors. The precise dissociation energy between actin and myosin depends upon the experimental conditions (ionic strength, pH, presence of ATP, etc.), but we estimate from previously reported values

for the dissociation constant that $\Delta G_{\text{dissoc}} < 10 k_{\text{B}} T$ per motor [63]. Since HMM is a non-processive motor, actin is rapidly binding and unbinding with the surface-bound motor and stochastically sampling the competing bending and binding energies within the trenches. We model the cross over of the filament into the "crowd-surfing" state when the filament crosses two or more trench boundaries.

In experiments on planar gliding assays, collisions between F-actin have been shown to have a slight polar symmetry, leading to large density fluctuations and nematic bands or polar flocks depending on experimental conditions [9]. In our model, interactions between filaments are purely steric with nematic symmetry. Generally, agent-based simulations and theories prescribe an additional alignment interaction to capture experimentally observed polar flocks, but here we focus on the isotropic to nematic transition. Therefore, this model will not capture the formation of bulk polar flocks seen in some experiments.

An important distinction between the experiments and the simulations is the complete suppression of collective swarms at small trench spacings. In the simulations, by contrast, collective swarms are observed even when the periodic repeat spacing is small, but the directional motion of these swarms do not correlate with the applied potential field. Rather, the simulated swarms "surf" across the peaks and valleys of the potential landscape. We attribute the absence of swarming in the experiments at small trench spacings to additional physics not accounted for in the simulations. For instance, scission events at the trench boundaries produce successively smaller filaments and reduce their ability to orient with one another. Such events occur more frequently when the trench spacing is narrow, which could possibly explain the absence of swarms in the experiments. By contrast, in the simulations the contour length of each filament is fixed and collisions between filaments can give rise to spontaneous collective motion. Bending of the filaments into the third dimension is another feature that is present in the experiments but not in the simulations.

6.3.4 Impact of Propulsion Speed and Trench Tortuosity on Swarm Formation

In a separate set of experiments, we varied the ATP concentration to study the role of propulsion speed on nematic band formation (Fig. 6.6). At ATP concentrations between 0.025 - 0.3 mM, we observed robust nematic bands along the trenches for intermediate spacings, $H = 10$ - 20 µm (Fig. 6.6A). However, at large ATP concentrations, ≥ 0.3 mM, we observed polar flocks and nematic swarms that were uncorrelated with the etched features (Fig. 6.6B; see also Supplementary Movie 7 of [1]), with similar structure and dynamics as previous studies on planar substrates [7].

Increasing the ATP concentration increases the rate of myosin attachment and detachment, as well as increases the number of myosin involved in pushing a single filament [64]. We suspect that the additional tension imparted onto the filament makes it easier to escape the channels and facilitates "crowd-surfing" due to increased ATP-driven detachment. Similar flocking behavior is observed in the simulations when the active force on the filament is large (see Supporting Information document of [1]).

Additionally, we studied the effect of in-plane tortuosity on nematic band formation by creating etched patterns that zigzag along the substrate. We hypothesized that the competition between the tortuosity path length and the swarm persistence length governs the onset of nematic band formation. To test this hypothesis, we studied two zigzag patterns, with periodic triangle- and square-wave features, at a fixed spacing $H = 20$ µm (Fig. 6.7). In both tortuous patterns, we observed accumulation of actin filaments along the boundaries but no swarming nematic bands. Tortuosity changes the preferred orientation at the channel edges causing destructive interference between nematic boundary layers at various points along the surface. The nematic bands disappear when the tortuosity path length is comparable to the swarm persistence length. Although the biased

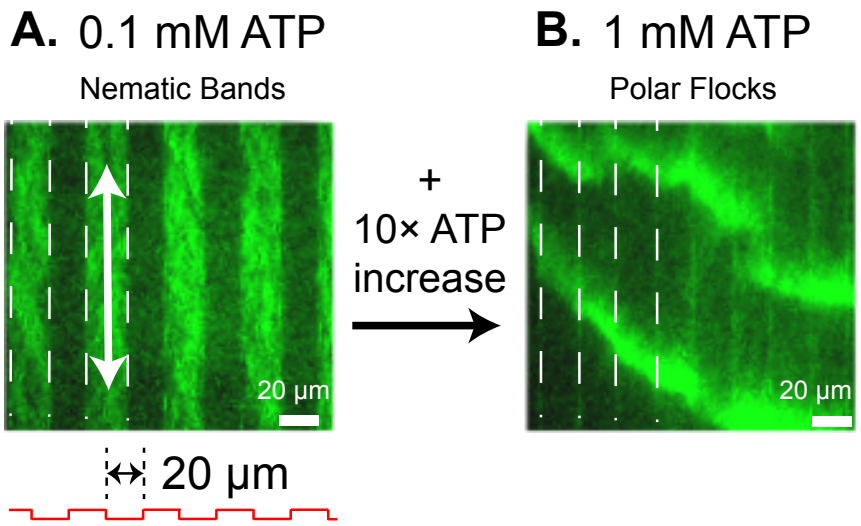

Figure 6.6: Topography-induced nematic bands only appear at intermediate propulsion speeds. (A) Nematic bands appear at intermediate ATP concentration, 0.1 mM. (B) Nematic bands vanish along the periodic trenches upon increasing ATP concentration to 1 mM. Polar flocks appear after 15 min, indicating that actin motion is unaffected by topography at high ATP concentration. These experiments were conducted with the same channel spacing, $H = 20$ μm.

orientation of an individual filament from one boundary can interact with other filaments on the opposing boundary, the tortuous path causes a destructive interference with no collective enhancement of nematic ordering. This effect is similar to a spherical active particle moving through a porous media with a tortuous path, which is known to create density and polar boundary layers that can overlap destructively [65, 66].

The fact that directed swarms emerge when the topographic and filament length scales are commensurate suggests a type of coherence between collections of filaments in a corrugated landscape. In dense 2D systems, passive filaments with infinite persistence length (hard rods) are known to undergo a Berezinskii-Kosterlitz-Thouless (BKT) phase transition [67, 68]. In an unbounded system, the local orientation correlation decays algebraically over a length scale λ that depends upon the Frank elastic constant of a continuum nematic fluid [69]. In our case, the soft walls bias the orientation of the

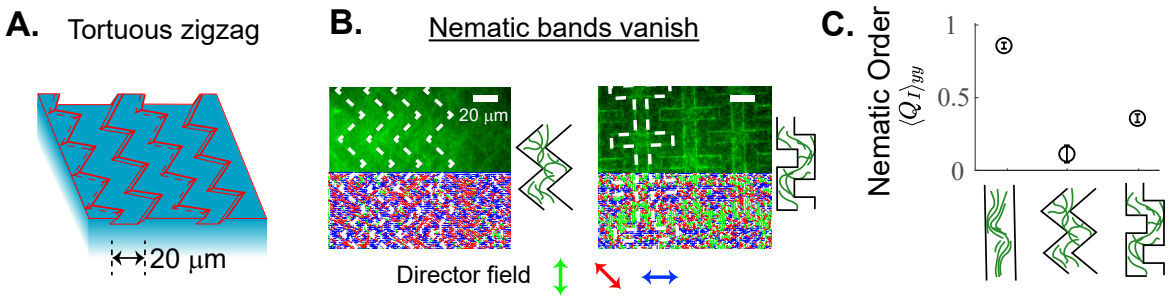

Figure 6.7: Etched substrates with tortuous topographies disrupt swarming nematic bands. (A) We designed etched substrates with tortuous zigzag patterns with $H = 20$ μm spacing. (B) Swarming nematic bands vanish on substrates with triangle- and square-wave patterns. Scale bars are 20 μm. (C) Comparing the yy component of the intensity-weighted nematic order tensor confirms the reduction of ordering along the y-direction on tortuous trenches compared to parallel trenches. All experiments are conducted at 0.05 mM ATP concentration.

filaments at the boundaries and this propagates into the center of the channel over the distance λ, which is a function of the effective Frank elastic constant and the activity. The effective elastic constant depends on the physical properties of the filament (i.e. filament persistence length and contour length) [70, 71]. We also vary the persistence length of the simulated filaments and show that the magnitude of nematic order increases and the location of the optimal spacing H^* decreases as the persistence length grows (see the Supporting Information document of [1]). Scission events due to collisions create a large polydispersity in the actin contour length. This precludes us from meaningfully increasing the F-actin length to explore different ratios of contour length and persistence length in experiments.

Consequently, nearby filaments align with the boundaries due to proximity with their neighbors. The finite concentration of filaments provides a mechanism of transmitting the nematic bias across multiple filaments up to a distance λ away from boundaries, beyond which orientational correlations between filaments rapidly fall off. If the corrugations are spaced less than λ, nematic order persists throughout the entire channel.

To help explain this idea of nematic coherence induced by an aligning bias, Fig. 6.8A-

C depicts simulation snapshots of a system of filaments with three different periodic repeat spacings, $H = 2$, 4, and 40 µm. In Fig. 6.8D-F, we have plotted histograms of the yy component of the *local* nematic order tensor, $\boldsymbol{Q}(x)$, corresponding to these snapshots. The local nematic order tensor is defined by "binning" filaments into a primitive section of the periodic potential landscape, spanning a distance $-H \leq x \leq H$:

$$\boldsymbol{Q}(x) = \frac{2H}{N_{\text{samp}}} \sum_{i=1}^{N_{\text{samp}}} [2\boldsymbol{q}(i)\boldsymbol{q}(i) - 1]\, \delta[x - x_H(i)], \tag{6.14}$$

where $x_H(i) = H + \text{mod}[x(i) + H, 2H]$ is the global displacement of the ith filament from the primitive periodic cell. In numerically evaluating Eq. 6.14, the Dirac delta function is approximated by a finite impulse function whose width and reciprocal height is equal to the bin size. Averaging Eq. 6.14 over the periodic interval, $-H \leq x \leq H$, recovers the *average* nematic order tensor defined by Eq. 6.13

$$\langle \boldsymbol{Q} \rangle = \frac{1}{2H} \int_{-H}^{H} \boldsymbol{Q}(x)\, dx; \tag{6.15}$$

therefore, the components of $\boldsymbol{Q}(x)$ are normalized such that their average over space $\langle \boldsymbol{Q} \rangle$ has components bounded between ± 1.

The snapshots and histograms presented in Fig. 6.8 can be understood as follows. For the narrow spacing shown ($H = 2$ µm, Fig. 6.8A,D), filaments are only partially biased by the potential gradient to align along the y direction. This weak bias results from the fact that the filaments are much longer than the repeat spacing ($L_c \gg H$, where $L_c = 10$ µm) and so frequently bridge multiple periodic cells under zero force and torque. Importantly, the peak nematic order is centered within the potential well. As H is increased to 4 µm (Fig. 6.8B,E), the peak nematic order increases in scale and widens in extent to span nearly the entire well. This case corresponds to the "optimal" spacing, H^*, discussed in Fig. 6.5. At much larger spacing ($H = 40$ µm, Fig. 6.8C,F), the peak nematic order localizes near the edges of the potential well, where the gradient

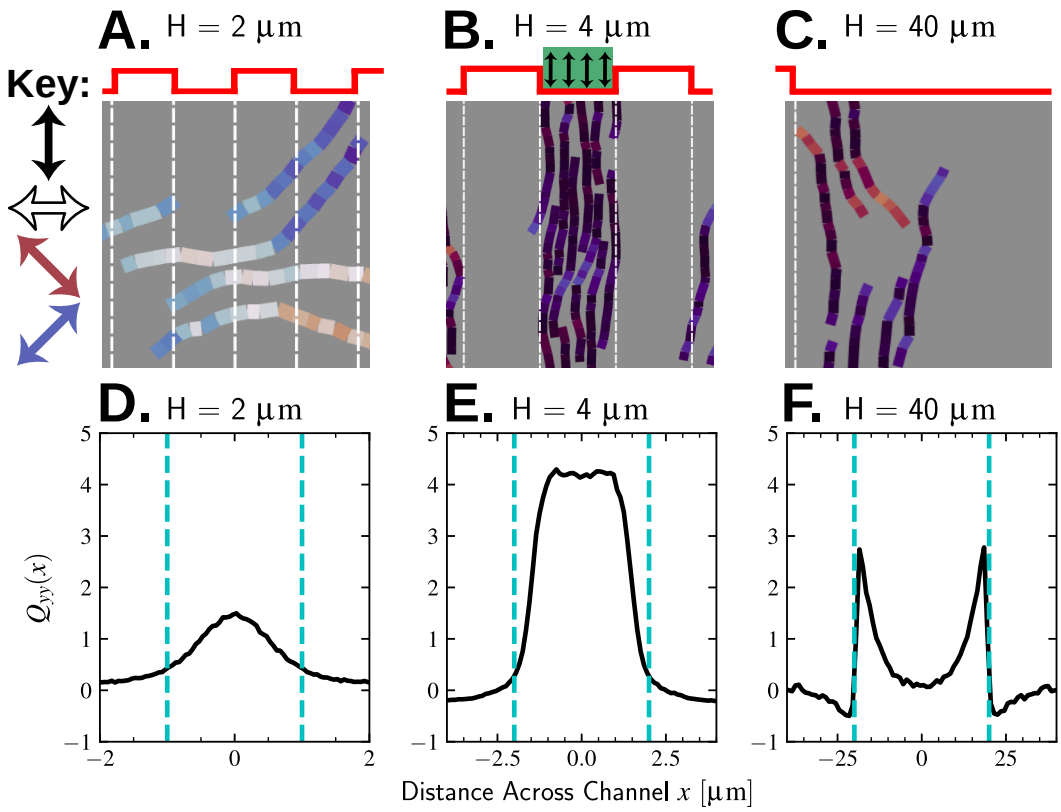

Figure 6.8: Nematic bands form when edge-induced nematic order is coherent through the entire channel. Top row (A)-(C): cropped simulation snapshots of filaments in a confining potential with different periodic repeat spacing. Filament segments are colored according to their director. White dashed lines indicate the edges of the potential wells where the gradient is strongest. Bottom row (D)-(F): local nematic order across a primitive periodic cell, obtained from Eq. 6.14. The origin of the x-axis is centered inside the potential well.

is strongest, and decays toward the center. The decay length (or coherence length), λ, is of order 10 μm and comparable to the filament contour length, L_c. In this case, the size of the well is larger than the scale over which nematic order can be transmitted via interactions with other filaments, resulting in loss of nematic order across a "boundary layer" adjacent to the edges of the well. Comparing this case to the intermediate spacing ($H = 4$ μm) indicates that the highest order is achieved when the two boundary layers on either side of the well overlap.

6.4 Conclusions

Our experimental results demonstrate that surface topography can be employed to induce and control the ordering and swarming transitions of self-propelled filaments at finite surface density. We successfully modeled this coupling between topography and collective motion using a 2D soft confinement potential, which reflects the local effect of bending filaments across the trench boundaries. The 2D system serves as a compelling model for understanding active force generation on curved surfaces of practical interest, including 2D active materials and biological cell membranes. Whether this concept extends to 3D active fluids remains to be demonstrated, but is worthy of further investigation.

Our findings highlight the intricate interplay between active propulsion, many-body interactions, and soft confinement, which orchestrate the emergence of ordered, regular patterns in active filaments under specific surface topographies. This observation suggests that the optimal confinement length scale, corresponding to the coherence length in active nematic systems, offers a valuable design principle for manipulating two-dimensional (2D) active fluids in confined geometries.

Future work in this project can focus on the utilization of collections of active filaments to enhance the capabilities of existing lab-on-a-chip devices. Specific topographical patterning can be used to locally enhance or repress swarming of filaments, allowing for precise control of the location and direction of nematic bands and polar flocks. Additionally, incorporating tortuous channels offers a promising approach for sorting or separating incoming groups of filaments, facilitating tasks like analyte detection while enabling greater filament surface density.

Bibliography

[1] J. M. Barakat, K. J. Modica, L. Lu, S. Anujarerat, K. H. Choi, and S. C. Takatori, *Surface topography induces and orients nematic swarms of active filaments: Considerations for lab-on-a-chip devices*, *ACS Applied Nano Materials* (5, 2024).

[2] A. P. Liu, D. L. Richmond, L. Maibaum, S. Pronk, P. L. Geissler, and D. A. Fletcher, *Membrane-induced bundling of actin filaments*, *Nature Physics* **4** (10, 2008) 789–793.

[3] I. M. Schwartz, M. Ehrenberg, M. Bindschadler, and J. L. McGrath, *The role of substrate curvature in actin-based pushing forces*, *Current Biology* **14** (6, 2004) 1094–1098.

[4] S. J. Kron and J. A. Spudich, *Fluorescent actin filaments move on myosin fixed to a glass surface.*, *Proceedings of the National Academy of Sciences* **83** (9, 1986) 6272–6276.

[5] G. Saper and H. Hess, *Synthetic systems powered by biological molecular motors*, *Chemical Reviews* **120** (9, 2019) 288–309.

[6] A. Månsson, *The potential of myosin and actin in nanobiotechnology*, *Journal of Cell Science* **136** (3, 2023) jcs261025.

[7] V. Schaller, C. Weber, C. Semmrich, E. Frey, and A. R. Bausch, *Polar patterns of driven filaments*, *Nature* **467** (9, 2010) 73–77.

[8] V. Schaller and A. R. Bausch, *Topological defects and density fluctuations in collectively moving systems*, *Proceedings of the National Academy of Sciences* **110** (3, 2013) 4488–4493.

[9] L. Huber, R. Suzuki, T. Krüger, E. Frey, and A. R. Bausch, *Emergence of coexisting ordered states in active matter systems*, *Science* **361** (7, 2018) 255–258.

[10] A. Sciortino and A. R. Bausch, *Pattern formation and polarity sorting of driven actin filaments on lipid membranes*, *Proceedings of the National Academy of Sciences* **118** (2, 2021) e2017047118.

[11] R. Suzuki and A. R. Bausch, *The emergence and transient behaviour of collective motion in active filament systems*, *Nature Communications* **8** (6, 2017) 41.

[12] H. Chaté, *Dry aligning dilute active matter*, *Annual Review of Condensed Matter Physics* **11** (3, 2020) 189–212.

[13] J. Denk and E. Frey, *Pattern-induced local symmetry breaking in active-matter systems*, *Proceedings of the National Academy of Sciences* **117** (12, 2020) 31623–31630.

[14] S. R. McCandlish, A. Baskaran, and M. F. Hagan, *Spontaneous segregation of self-propelled particles with different motilities*, *Soft Matter* **8** (2012), no. 8 2527.

[15] S. J. DeCamp, G. S. Redner, A. Baskaran, M. F. Hagan, and Z. Dogic, *Orientational order of motile defects in active nematics*, *Nature Materials* **14** (8, 2015) 1110–1115.

[16] K. Thijssen, D. A. Khaladj, S. A. Aghvami, M. A. Gharbi, S. Fraden, J. M. Yeomans, L. S. Hirst, and T. N. Shendruk, *Submersed micropatterned structures control active nematic flow, topology, and concentration*, *Proceedings of the National Academy of Sciences* **118** (9, 2021) e2106038118.

[17] C. Reuther, R. Catalano, A. Salhotra, V. Vemula, T. Korten, S. Diez, and

A. Månsson, *Comparison of actin- and microtubule-based motility systems for application in functional nanodevices*, *New Journal of Physics* **23** (7, 2021) 075007.

[18] M. Schuppler, F. C. Keber, M. Kröger, and A. R. Bausch, *Boundaries steer the contraction of active gels*, *Nature Communications* **7** (10, 2016) 13120.

[19] T. D. Ross, H. J. Lee, Z. Qu, R. A. Banks, R. Phillips, and M. Thomson, *Controlling organization and forces in active matter through optically defined boundaries*, *Nature* **572** (8, 2019) 224–229.

[20] R. Zhang, S. A. Redford, P. V. Ruijgrok, N. Kumar, A. Mozaffari, S. Zemsky, A. R. Dinner, V. Vitelli, Z. Bryant, M. L. Gardel, and J. J. de Pablo, *Spatiotemporal control of liquid crystal structure and dynamics through activity patterning*, *Nature Materials* **20** (6, 2021) 875–882.

[21] R. Zhang, A. Mozaffari, and J. J. de Pablo, *Autonomous materials systems from active liquid crystals*, *Nature Reviews Materials* **6** (2, 2021) 437–453.

[22] N. Kumar, R. Zhang, J. J. de Pablo, and M. L. Gardel, *Tunable structure and dynamics of active liquid crystals*, *Science Advances* **4** (10, 2018) eaat7779.

[23] P. Guillamat, J. Ignés-Mullol, and F. Sagués, *Control of active liquid crystals with a magnetic field*, *Proceedings of the National Academy of Sciences* **113** (5, 2016) 5498–5502.

[24] K.-T. Wu, J. B. Hishamunda, D. T. N. Chen, S. J. DeCamp, Y.-W. Chang, A. Fernández-Nieves, S. Fraden, and Z. Dogic, *Transition from turbulent to coherent flows in confined three-dimensional active fluids*, *Science* **355** (3, 2017) eaal1979.

[25] J. Hardoüin, C. Doré, J. Laurent, T. Lopez-Leon, J. Ignés-Mullol, and F. Sagués, *Active boundary layers in confined active nematics*, *Nature Communications* **13** (11, 2022) 6675.

[26] J. Hardoüin, R. Hughes, A. Doostmohammadi, J. Laurent, T. Lopez-Leon, J. M. Yeomans, J. Ignés-Mullol, and F. Sagués, *Reconfigurable flows and defect landscape of confined active nematics*, *Communications Physics* **2** (10, 2019) 1–9.

[27] H. S. H. Suzuki, K. O. K. Oiwa, A. Y. A. Yamada, H. S. H. Sakakibara, H. N. H. Nakayama, and S. M. S. Mashiko, *Linear arrangement of motor protein on a mechanically deposited fluoropolymer thin film*, *Japanese Journal of Applied Physics* **34** (7, 1995) 3937.

[28] D. V. Nicolau, H. Suzuki, S. Mashiko, T. Taguchi, and S. Yoshikawa, *Actin motion on microlithographically functionalized myosin surfaces and tracks*, *Biophysical Journal* **77** (8, 1999) 1126–1134.

[29] J. A. Jaber, P. B. Chase, and J. B. Schlenoff, *Actomyosin-driven motility on patterned polyelectrolyte mono- and multilayers*, *Nano Letters* **3** (11, 2003) 1505–1509.

[30] K. L. Hanson, F. Fulga, S. Dobroiu, G. Solana, O. Kaspar, V. Tokarova, and D. V. Nicolau, *Polymer surface properties control the function of heavy meromyosin in dynamic nanodevices*, *Biosensors and Bioelectronics* **93** (7, 2017) 305–314.

[31] M. Sundberg, M. Balaz, R. Bunk, J. P. Rosengren-Holmberg, L. Montelius, I. A. Nicholls, P. Omling, S. Tågerud, and A. Månsson, *Selective spatial localization of actomyosin motor function by chemical surface patterning*, *Langmuir* **22** (8, 2006) 7302–7312.

[32] Y. Hiratsuka, T. Tada, K. Oiwa, T. Kanayama, and T. Q. Uyeda, *Controlling the direction of kinesin-driven microtubule movements along microlithographic tracks*, *Biophysical Journal* **81** (9, 2001) 1555–1561.

[33] J. Clemmens, H. Hess, R. Lipscomb, Y. Hanein, K. F. Böhringer, C. M. Matzke, G. D. Bachand, B. C. Bunker, and V. Vogel, *Mechanisms of microtubule guiding on microfabricated kinesin-coated surfaces: Chemical and topographic surface patterns*, *Langmuir* **19** (12, 2003) 10967–10974.

[34] J. Clemmens, H. Hess, J. Howard, and V. Vogel, *Analysis of microtubule guidance in open microfabricated channels coated with the motor protein kinesin*, *Langmuir* **19** (3, 2003) 1738–1744.

[35] J. Clemmens, H. Hess, R. Doot, C. M. Matzke, G. D. Bachand, and V. Vogel, *Motor-protein "roundabouts": Microtubules moving on kinesin-coated tracks through engineered networks*, *Lab Chip* **4** (2004) 83–86.

[36] D. V. J. Nicolau, M. Lard, T. Korten, F. C. M. J. M. van Delft, M. Persson, E. Bengtsson, A. Månsson, S. Diez, H. Linke, and D. V. Nicolau, *Parallel computation with molecular-motor-propelled agents in nanofabricated networks*, *Proceedings of the National Academy of Sciences* **113** (3, 2016) 2591–2596.

[37] R. Bunk, J. Klinth, L. Montelius, I. A. Nicholls, P. Omling, S. Tågerud, and A. Månsson, *Actomyosin motility on nanostructured surfaces*, *Biochemical and Biophysical Research Communications* **301** (2, 2003) 783–788.

[38] R. Bunk, M. Sundberg, A. Månsson, I. A. Nicholls, P. Omling, S. Tågerud, and L. Montelius, *Guiding motor-propelled molecules with nanoscale precision through silanized bi-channel structures*, *Nanotechnology* **16** (6, 2005) 710–717.

[39] F. W. Lindberg, M. Norrby, M. A. Rahman, A. Salhotra, H. Takatsuki, S. Jeppesen, H. Linke, and A. Månsson, *Controlled surface silanization for actin-myosin based nanodevices and biocompatibility of new polymer resists*, *Langmuir* **34** (7, 2018) 8777–8784.

[40] M. Lard, L. ten Siethoff, S. Kumar, M. Persson, G. te Kronnie, H. Linke, and A. Månsson, *Ultrafast molecular motor driven nanoseparation and biosensing*, *Biosensors and Bioelectronics* **48** (10, 2013) 145–152.

[41] M. Sundberg, R. Bunk, N. Albet-Torres, A. Kvennefors, F. Persson, L. Montelius, I. A. Nicholls, S. Ghatnekar-Nilsson, P. Omling, S. Tågerud, and A. Månsson, *Actin filament guidance on a chip: Toward high-throughput assays and lab-on-a-chip applications*, *Langmuir* **22** (8, 2006) 7286–7295.

[42] L. Cheng, M. Kao, E. Meyhöfer, and L. J. Guo, *Highly efficient guiding of microtubule transport with imprinted cytop nanotracks*, *Small* **1** (4, 2005) 409–414.

[43] D. Inoue, G. Gutmann, T. Nitta, A. M. R. Kabir, A. Konagaya, K. Tokuraku, K. Sada, H. Hess, and A. Kakugo, *Adaptation of patterns of motile filaments under dynamic boundary conditions*, *ACS Nano* **13** (11, 2019) 12452–12460.

[44] D. A. Khaladj and L. S. Hirst, *Using curved fluid boundaries to confine active nematic flows*, *Frontiers in Physics* **10** (4, 2022) 880941.

[45] M. Striebel, I. R. Graf, and E. Frey, *A mechanistic view of collective filament motion in active nematic networks*, *Biophysical Journal* **118** (1, 2020) 313–324.

[46] S. Ramaswamy and M. Rao, *Active-filament hydrodynamics: instabilities, boundary conditions and rheology*, *New Journal of Physics* **9** (11, 2007) 423–423.

[47] A. Doostmohammadi, J. Ignés-Mullol, J. M. Yeomans, and F. Sagués, *Active nematics*, *Nature Communications* **9** (8, 2018) 3246.

[48] A. Baskaran and M. C. Marchetti, *Hydrodynamics of self-propelled hard rods*, *Physical Review E* **77** (1, 2008) 011920.

[49] A. Baskaran and M. C. Marchetti, *Enhanced diffusion and ordering of self-propelled rods*, *Physical Review Letters* **101** (12, 2008) 268101.

[50] A. Baskaran and M. C. Marchetti, *Self-regulation in self-propelled nematic fluids*, *The European Physical Journal E* **35** (9, 2012) 95.

[51] T. N. Shendruk, A. Doostmohammadi, K. Thijssen, and J. M. Yeomans, *Dancing disclinations in confined active nematics*, *Soft Matter* **13** (2017), no. 21 3853–3862.

[52] M. M. Norton, A. Baskaran, A. Opathalage, B. Langeslay, S. Fraden, A. Baskaran, and M. F. Hagan, *Insensitivity of active nematic liquid crystal dynamics to topological constraints*, *Phys. Rev. E* **97** (1, 2018) 012702.

[53] C. Joshi, Z. Zarei, M. M. Norton, S. Fraden, A. Baskaran, and M. F. Hagan, *From disks to channels: dynamics of active nematics confined to an annulus*, *Soft Matter* **19** (2023) 5630–5640.

[54] R. Parthasarathy, C. han Yu, and J. T. Groves, *Curvature-modulated phase separation in lipid bilayer membranes*, *Langmuir* **22** (5, 2006) 5095–5099.

[55] A. Månsson, M. Balaz, N. Albet-Torres, and K. J. Rosengren, *In vitro assays of molecular motors – impact of motor-surface interactions*, *FBL* **13** (2008) 5732–5754.

[56] J. D. Pardee and J. A. Spudich, *Purification of muscle actin*, vol. 85, pp. 164–181. Academic Press, 1982.

[57] S. S. Margossian and S. Lowey, *Preparation of myosin and its subfragments from rabbit skeletal muscle*, vol. 85, pp. 55–71. Academic Press, 1982.

[58] T. D. Pollard, *Myosin Purification and Characterization*, vol. 24, pp. 333–371. Academic Press, 1982.

[59] R. E. Isele-Holder, J. Elgeti, and G. Gompper, *Self-propelled worm-like filaments: spontaneous spiral formation, structure, and dynamics*, *Soft Matter* **11** (2015) 7181–7190.

[60] M. Persson, N. Albet-Torres, L. Ionov, M. Sundberg, F. Höök, S. Diez, A. Månsson, and M. Balaz, *Heavy meromyosin molecules extending more than 50 nm above adsorbing electronegative surfaces*, *Langmuir* **26** (6, 2010) 9927–9936.

[61] L. D. Landau and E. M. Lifshitz, *Theory of elasticity*, vol. 7. Pergamon Press, 1959.

[62] R. Adkins, I. Kolvin, Z. You, S. Witthaus, M. C. Marchetti, and Z. Dogic, *Dynamics of active liquid interfaces*, *Science* **377** (8, 2022) 768–772.

[63] J. R. Sellers, E. Eisenberg, and R. S. Adelstein, *The binding of smooth muscle heavy meromyosin to actin in the presence of atp. effect of phosphorylation.*, *The Journal of biological chemistry* **257** (12, 1982) 13880–3.

[64] K. Rastogi, M. S. Puliyakodan, V. Pandey, S. Nath, and R. Elangovan, *Maximum limit to the number of myosin ii motors participating in processive sliding of actin*, *Scientific Reports* **6** (8, 2016) 32043.

[65] K. J. Modica, Y. Xi, and S. C. Takatori, *Porous media microstructure determines the diffusion of active matter: Experiments and simulations*, *Frontiers in Physics* **10** (4, 2022) 869175.

[66] K. J. Modica, A. K. Omar, and S. C. Takatori, *Boundary design regulates the diffusion of active matter in heterogeneous environments*, *Soft Matter* **19** (2023) 1890–1899.

[67] J. M. Kosterlitz and D. J. Thouless, *Ordering, metastability and phase transitions in two-dimensional systems*, *Journal of Physics C: Solid State Physics* **6** (4, 1973) 1181–1203.

[68] V. L. Berezinsky, *Destruction of long range order in one-dimensional and two-dimensional systems having a continuous symmetry group. i. classical systems*, *Sov. Phys. JETP* **32** (1971) 493–500.

[69] M. A. Bates and D. Frenkel, *Phase behavior of two-dimensional hard rod fluids*, *The Journal of Chemical Physics* **112** (6, 2000) 10034–10041.

[70] S. P. Thampi, R. Golestanian, and J. M. Yeomans, *Velocity correlations in an active nematic*, *Phys. Rev. Lett.* **111** (9, 2013) 118101.

[71] E. J. Hemingway, P. Mishra, M. C. Marchetti, and S. M. Fielding, *Correlation lengths in hydrodynamic models of active nematics*, *Soft Matter* **12** (2016), no. 38 7943–7952.

Chapter 7

Conclusions and Outlook

In this dissertation, I have developed models to analyze the structure and dispersion of confined active swimmers in two dimensions. I have found that the nonequilibrium self-propulsion couples the particle dynamics to the surrounding surface microstructure, controlling both the transport and the steady-state distribution of the swimmers.

In Chapter 2, we introduced several techniques that are commonly used to predict the effective diffusivity of *passive* colloidal systems, and tested their applicability to nonequilibrium swimmers via the "effective temperature" approach. While the effective temperature approach provides a good first approximation to estimate active diffusivity, it fails to capture the impact of boundary shape when the run length is commensurate to the surface radius of curvature. In Chapter 3, we tested the impact of surface concavity using simulations and experimental measurements of active Brownian particle (ABP) transport in random arrays of immovable obstacles. As the porosity decreases, collections of obstacles aggregate into impassible walls and concave traps. The increased accumulation of active Brownian particles at regions of high concavity inhibits active transport when compared to convex systems at identical porosity.

In Chapter 4, we extended our Smoluchowski-based models to study the mobility of anisotropic swimmers under confining external fields. For rods in channel confinement, the torque imposed on the rod nematically orients the particles along the channel axis. As rod nematic order increases, there is an subsequent magnification of diffusivity in the direction parallel to the channels. This occurs because the nematic alignment inhibits reorientation of the rods, creating extended ballistic runs. In Chapters 5 and 6, we use the methods we have developed to study systems of practical interest. We are able to predict the partitioning of bacteria in an aqueous two-phase system (ATPS) of dextran and polyethylene glycol. We verified that the motility allows the bacteria to overcome the chemical affinity between the bacteria surface and the dextran polymer, partitioning the bacteria between the two phases. Additionally, we used simulations to offer mechanistic

insight into the alignment of cytoskeletal filaments within topographically patterned surfaces. In a gliding assay containing shallow channels, we find that filaments escape due to their flexibility and exhibit a unique "crowd-surfing" behavior at intermediate channel width. In summary, we find that one can control active transport by careful design of the boundary microstructure. Through extensive collaboration with experimentalists, we have shown the utility of these models in providing mechanistic insight and have provided design principles for engineers seeking to create devices utilizing active agents.

A clear future direction of this work would be to extend these models into three-dimensional systems. Percolation of obstacles in 2D prevents all transport; however, in 3D the swimmer has additional directions it can move to avoid barriers, even when the obstacles are closely packed. Incorporating the additional degrees of freedom necessary to model three-dimensional active motion is both computationally and analytically challenging, but it is a critical next step toward accurately predicting active transport through many biologically and industrially relevant materials. The continued development of GPU-accelerated Brownian dynamics will be essential for studying these phenomena in three dimensions.

This work examines the confinement of active swimmers using stationary obstacles or fixed external fields. However, many porous materials are soft, elastic, and dynamic. For example, fluctuations can play an important role in particle transport through mucus, hydrogels, and other polymeric networks due to the flexibility of the mesh. Cytoskeletal filaments control cell shape and induce large deformations on lipid membranes, changing the boundary curvature and active transport drastically. In suspended media, obstacles will dynamically rearrange due to thermal fluctuations, fluid flow, or from the pressure of the active bath. These rearrangements allow swimmers to enter previously inaccessible regions of the phase space, and warrants future study.

With the exception of Chapter 6, we focused on the transport of *dilute* active swim-

mers and ignore interactions between particles. Extending this work to concentrated suspensions is possible using a modification to the Smoluchowski equation that incorporates density correlations via a mean-field, or by using a phenomenological hydrodynamic model of dense active nematics. These techniques would be particularly useful when modeling the behavior of bacteria in biofilms, which may help researchers design new treatments for these traditionally recalcitrant multicellular aggregates.